Constraining the Hubble constant from structural and dynamical analysis of the Leo I group

Master's Thesis

Niels Bohr Institute

University of Copenhagen

Written by

Kevin Kumar

Supervised by

Jens Hjorth

FACULTY:	SCIENCE	
INSTITUTE:	Niels Bohr Institute	
AUTHOR:	Kevin Kumar	KU-ID: VGJ803
SUPERVISOR:	Jens Hjorth	jens@nbi.ku.dk
HANDED IN:	20th of May 2021	
DEFENDED:	3rd of June 2021	

Abstract

Two different approaches are traditionally used to determine the Hubble constant. The discrepancy of the value obtained from each approach has rendered astronomers perplexed over the past few years. Recent observations of the Leo I group reveal conflicting conclusions about its dynamics and structure. Using high-precision TRGB-based measurements of the Leo I group, it is possible to re-analyse its structure and provide a distance ratio between the group and the Coma cluster through a revised Fundamental Plane. The estimated distance to the Coma cluster is $D_{\mathrm{Coma}} = (99 \pm 2\,(\mathrm{stat}) \pm 3\,(\mathrm{sys}))$ Mpc. The peculiar velocity of Coma is obtained through low-redshift Universe reconstruction. This provides a corrected observed velocity of Coma in the CMB rest-frame of $v_{\mathrm{Coma}} = (7190 \pm 160)$ kms^{-1}. The resulting value of the Hubble constant is $H_0 = (74 \pm 2\,(\mathrm{stat}) \pm 3\,(\mathrm{sys}))$ kms^{-1}Mpc^{-1}, which is in good agreement with recent type Ia SNe and Cepheid-based estimates.

Contents

1 Introduction

The Hubble constant, H_0, is one of the most important numbers in cosmology as it describes the current expansion rate of the Universe, which can be translated into its age and history. In 1929, Edwin Hubble provided the first estimate of H_0 and although almost a century has passed, astronomers still disagree on the exact value. The value of H_0 has been determined from two different precise methods, and yet the discrepancy between the results ranges up to 5σ. This phenomenon is referred to as the *Hubble tension*. Determining H_0 from observations of type Ia supernovae and Cepheids yields a value of $H_0 = (73.2 \pm 1.3)$ kms^{-1}Mpc^{-1} (Riess et al., 2021) and observations of the cosmic microwave background (CMB) yields (67.36 ± 0.54) kms^{-1}Mpc^{-1} (Planck Collaboration et al., 2020).

The value determined from the CMB is model-based and relies on the fundamental physics believed to have driven the evolution of the Universe. The tension between the two values of $\sim 4\sigma$, therefore, implies that either our measurements are subject to unknown systematic errors and effects or that our understanding of the underlying cosmological model is inadequate or flawed. One way of clarifying this problem is to provide independent measurements of H_0. This is where the Leo I group comes in.

The Leo I galaxy group is amongst the closest groups other than the local group, such that it is ideal as a distance indicator. In order to determine H_0, one must know the distance to a given object and its recessional velocity. There are many known techniques for determining distances to celestial objects, whose underlying physical processes are well-understood by astronomers.

However, in practice, one must overcome a number of obstacles related to the calibration of the method, making it difficult to obtain high-precision measurements at large distances. Measuring the radial velocity of an object is more straightforward, but also comes with its complications as peculiar velocities dominate at smaller distances and are difficult to determine. Given more recent high-precision distance measurements to the members of Leo I, we may circumvent this by establishing a distance to Leo I and stepping out to

larger distances where we gain higher precision in the velocity estimates.

1.1 The Leo I group

Figure 1 shows the galaxies in the Leo constellation as illustrated by *An Atlas of The Universe* (Powell, 2003). The illustration is a wide field view of the lower centre of the constellation.

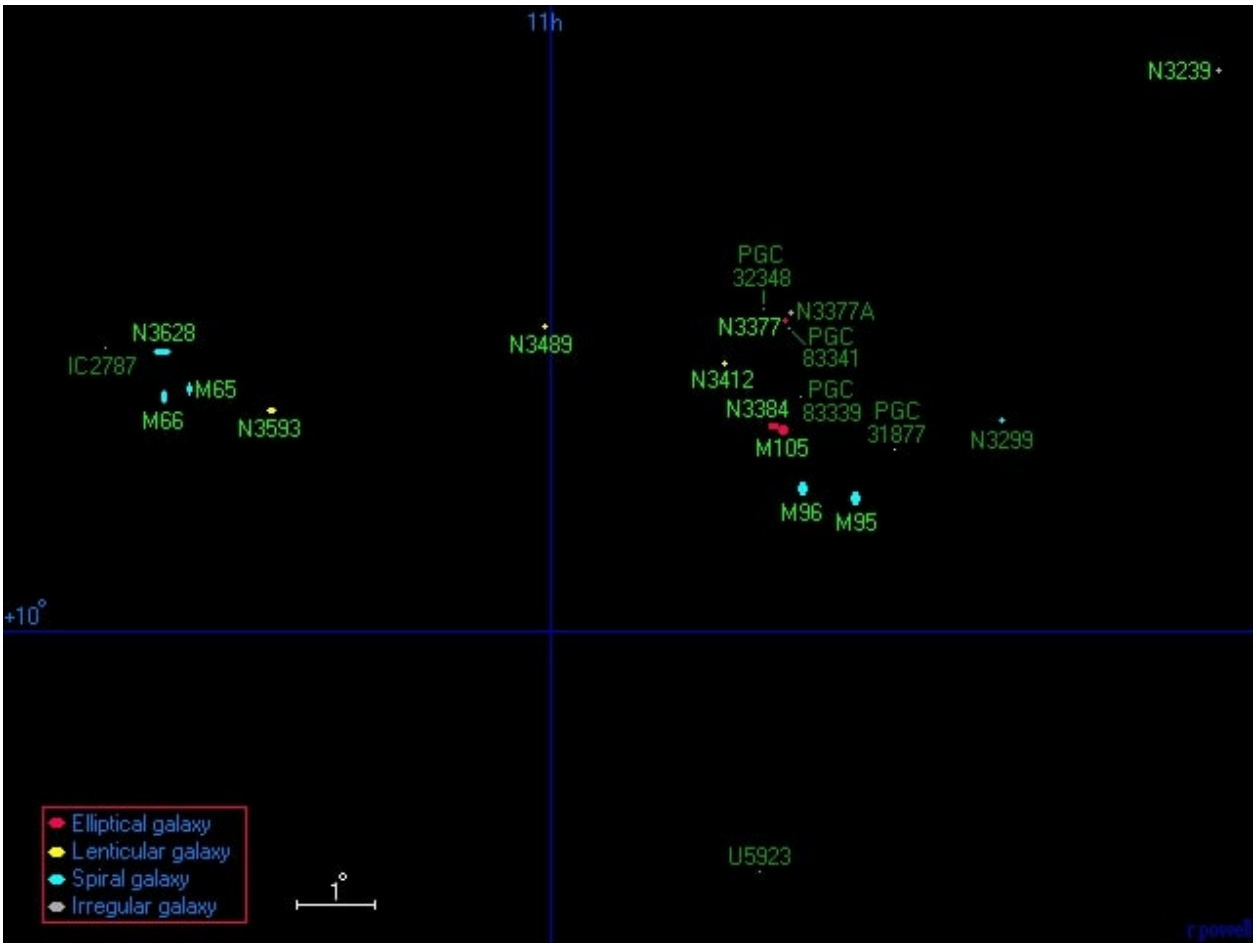

Figure 1: Illustration of galaxies in the Leo constellation (Powell, 2003). The colours indicate the type of galaxy as shown in the legend.

Membership studies traditionally divide the galaxies in the constellation into two subgroups. The first is called the *M66 Group* and includes three bright spirals located in the eastern part of the constellation. In this thesis, we focus on the second subgroup known as the *M96 Group* or the *Leo I Group* as we shall refer to it in this work, and is located in the western part of the constellation. Although the membership assignment of the group is

still actively debated, seven galaxies are established as known members. These are listed in Table 1 along with their morphology as classified by de Vaucouleurs et al. (1991).

Table 1: Members of the Leo I group and their morphology. Abbreviations for the galaxy types are described in Table 21 in Appendix K.

Name	NGC 3351 (M95)	NGC 3368 (M96)	NGC 3379 (M105)	NGC 3377	NGC 3384	NGC 3412	NGC 3489
Type	SB(r)b	SAB(rs)ab	E1	E5-6	SB(s)0	SB(s)0	SAB(rs)0

The group consists of mostly early-type galaxies: the two elliptical NGC 3379 and NGC 3377, and the three lenticular galaxies NGC 3384, NGC 3412 and NGC 3489. The exception to this are the two spirals NGC 3351 and NGC 3368. As shown in Figure 1, NGC 3379, NGC 3368 and NGC 3384 are in close proximity to each other and are traditionally considered the centre of the group. This is widely accepted in literature based on a proposed link between these three members put forth by Schneider (1985). The link is derived from a giant HI structure, typically called *the Leo ring*, that appears to be interacting with NGC 3368 whilst orbiting NGC 3379 and NGC 3384 along an elliptical path.

However, studies on the origin of the HI structure reveal that it might be a transient phenomenon rather than a primordial one, thus casting doubt on its Keplerian nature (Oosterloo et al., 2010) and, consequently, also on the established structure of the group (Kumar, 2020). In order to provide a precise estimate of H_0, it is crucial to understand the structure and properties of the Leo I group. This information dictates how we determine the distance to the group and subsequently how we step out to larger distances.

Given the doubt on the link between the three members, we find it necessary to probe the structure of the group. This is done by using high-precision distance measurements across different techniques from which we are able to compare the relative distances to the members. We test the hypothesis that NGC 3368, NGC 3379 and NGC 3384 are located at the same distance within statistical fluctuations.

Determining the distance at larger scales requires well-studied objects which we are able to accurately relate to the Leo I group. We shall make use of the Fundamental Plane fitted to early-type galaxies in the Coma cluster presented by Jorgensen et al. (1996). This

was previously done in Hjorth & Tanvir (1997) by assuming the same distance to the members of Leo I and fitting the Fundamental Plane to the 5 early-types in Leo I. From the derived zero points of the Fundamental Plane in Leo I and Coma, it is possible to obtain a luminosity distance ratio. We revise the method from Hjorth & Tanvir (1997) based on the structural and dynamical analysis of the Leo I group.

This thesis is divided into three parts. In the first part (Section 2), we shall analyse the dynamics of the giant HI structure in Leo I and test the hypothesis that it may be adequately described by a Keplerian model. This is done by solving Kepler's problem and fitting the derived model to 21 cm observations of the HI structure. In the second part (Section 3), we shall further analyse the relationship between the members based on newer high-precision measurements and provide a revised structural image of the group. In the third part (Section 4), we estimate H_0 by determining the distance ratio between members of the Leo I group and the Coma cluster through the Fundamental Plane. In Section 5, we discuss the strengths and weaknesses of such an approach that aims to provide an independent measurement of H_0 from knowledge of the Leo I group. Section 6 summarises the main findings and conclusions of this work.

2 The intergalactic neutral hydrogen in the Leo I group

Extended HI structures around galaxies are of great importance when probing galaxy formation scenarios. One of the distinct features of the Leo I group is the intergalactic neutral hydrogen which, at first glance, seems to be distributed in a ring-like structure. The giant structure in the Leo group is one of the largest HI structures in the nearby Universe. The origin of the structure is still actively debated. It could consist of primordial gas, as suggested by the lack of an optical counterpart and lack of a strong physical connection to nearby galaxies. Another suggestion is that the gas could be expelled from a galaxy in a collision. A false-colour image of the 4 largest members in the Leo I group and the HI structure is shown in Figure 2 (Watkins et al., 2014).

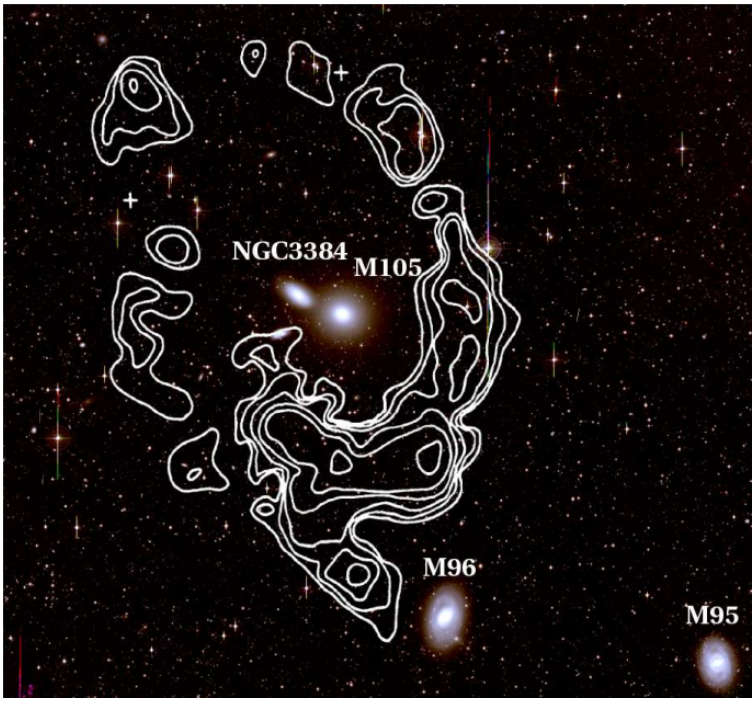

Figure 2: *Figure 1* from Watkins et al. (2014). False-colour image of the Leo I Group. The four largest group members are labelled. HI contours from Schneider (1985) are overlaid in white.

Although not obvious, one possibility could be that the main cloud had undergone tidal interaction with the galaxy M96 (henceforth NGC 3368), explaining the extension towards NGC 3368 and the overall 'S'-type symmetry of the observed HI (Schneider, 1985). Additional models suggest a head-on collision between NGC 3368 and NGC 3384. It was suggested by Schneider (1985) that the velocity structure across the main cloud could be

explained by rotation about M105 (henceforth NGC 3379) and/or NGC 3384. This would provide a unique link between three key galaxies: NGC 3379, NGC 3368 and NGC 3384. If the structure is in fact orbiting NGC 3379 and/or NGC 3384, it would link these members with NGC 3368, where interactions with the HI structure is observed (Watkins et al., 2014). In order to understand the structure of Leo I, this is an important hypothesis to investigate, since it would situate NGC 3379, NGC 3384 and NGC 3368 virtually at the same distance relative to us. We shall return to the importance of the structure in Section 3.

In this section, we will explore and analyse the dynamics of the HI structure and the connection to the aforementioned members in the Leo I group. We test the hypothesis by fitting a Keplerian model to the HI structure and analyse the constraints this would put on the properties of the group. A majority of the early work done in the Leo I group has been carried out by Stephen Schneider in a series of papers from the 80's. We specifically make use of the dynamical analysis from Schneider (1985) (hereafter S85).

2.1 The data

The first discovery of the HI structure was made in 1983 at the Arecibo Observatory (Schneider et al., 1983). The clouds II-IV (see Figure 3) were discovered by accident while unsuccessfully searching for the redshift of UGC 5808. Previous studies at the time had shown that isolated intergalactic gas clouds are rare. Additionally, the observed clouds II through IV were more extreme, showed a larger spatial extent and most importantly, the derived HI mass situated more than 3 Holmberg radii away from individual galaxy centres were much larger in both percentage and absolute amount. The Holmberg radius is a measure of a galaxy's size and is defined to be the projected length of the semi-major axis of an ellipsoid having an isophotal surface brightness if 26.5 B-mag arcsec^{-2} (Carroll & Ostlie, 2007).

The region was mapped using Arecibo 21 cm dual-circular polarisation feed. The observations were carried out in a total band-pass 2.5 MHz wide. For reduction, all second-order baselines were removed from the spectra. The spectra were Hanning smoothed once, resulting in a velocity resolution of 4 kms^{-1} with noise levels around 5 mJy rms.

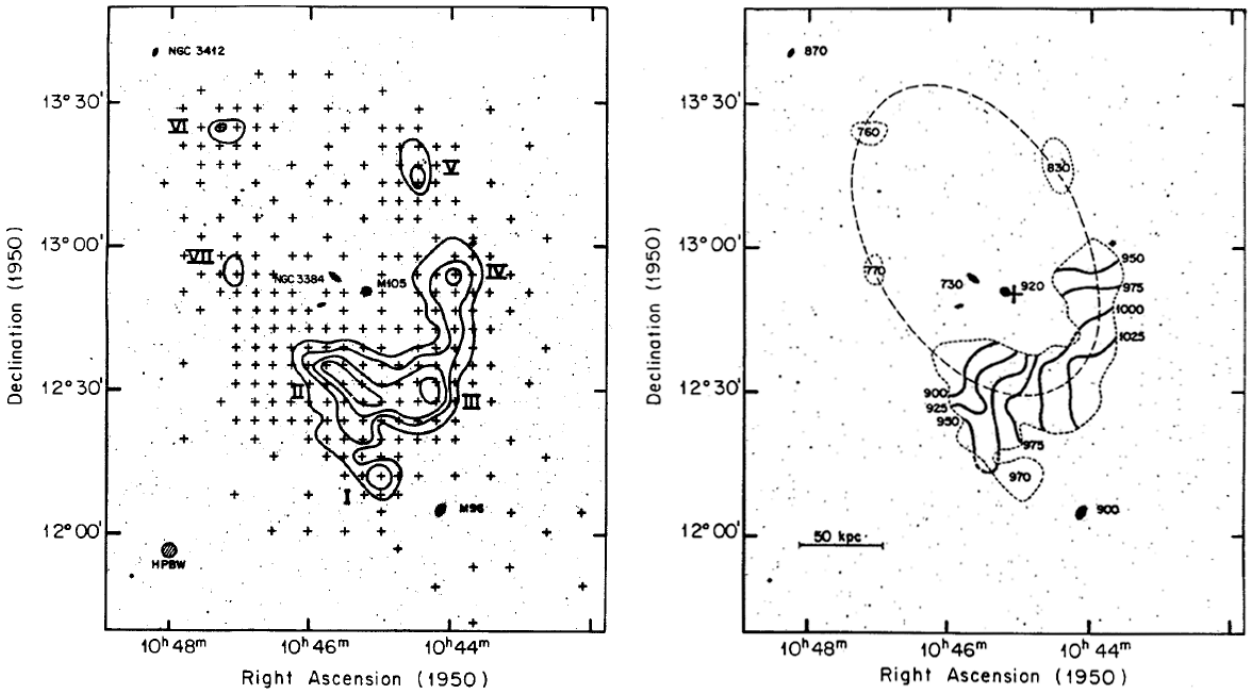

Figure 3: **Left panel:** *Fig 1a* from S85. Distribution of the intergalactic neutral hydrogen. Integrated flux contour levels are at $\int Tdv = 5$, 10, 20, and 40 K kms^{-1}. The points observed are marked with crosses. The local peaks in the HI intensity are labelled as clouds I through VII. The half-power beam width is shown in the bottom left corner. **Right panel:** *Fig 1b* from S85. Heliocentric velocity contours in the main cloud complex, and velocities of the individual clouds and galaxies. An ellipse fit through clouds II-VII is shown and the position of the focus predicted from the radial velocity pattern is marked by a cross. The 50 kpc scale assumes a distance to the group of 10 Mpc.

In Figure 4, the HI map from Schneider et al. (1983) is shown in the left panel and the representative spectra from across the cloud in the right panel. The line fluxes were reduced to brightness temperatures. This was done in Schneider et al. (1983) by assuming a beam efficiency of 0.65, which includes an estimate of the first sidelobe contribution from the spectra and a forward gain of 8 K Jy^{-1}. In the left panel of Figure 4, the contours indicate the integrated brightness temperatures.

The heliocentric redshift varies from about 870 km s^{-1} at the eastern edge to around 1050 km s^{-1} at the western edge. Additionally, the mean velocity of the southern part extending towards NGC 3368 is around 970 km s^{-1}, which is close to the systemic velocity of the whole cloud at 960 km s^{-1} (Schneider et al., 1983).

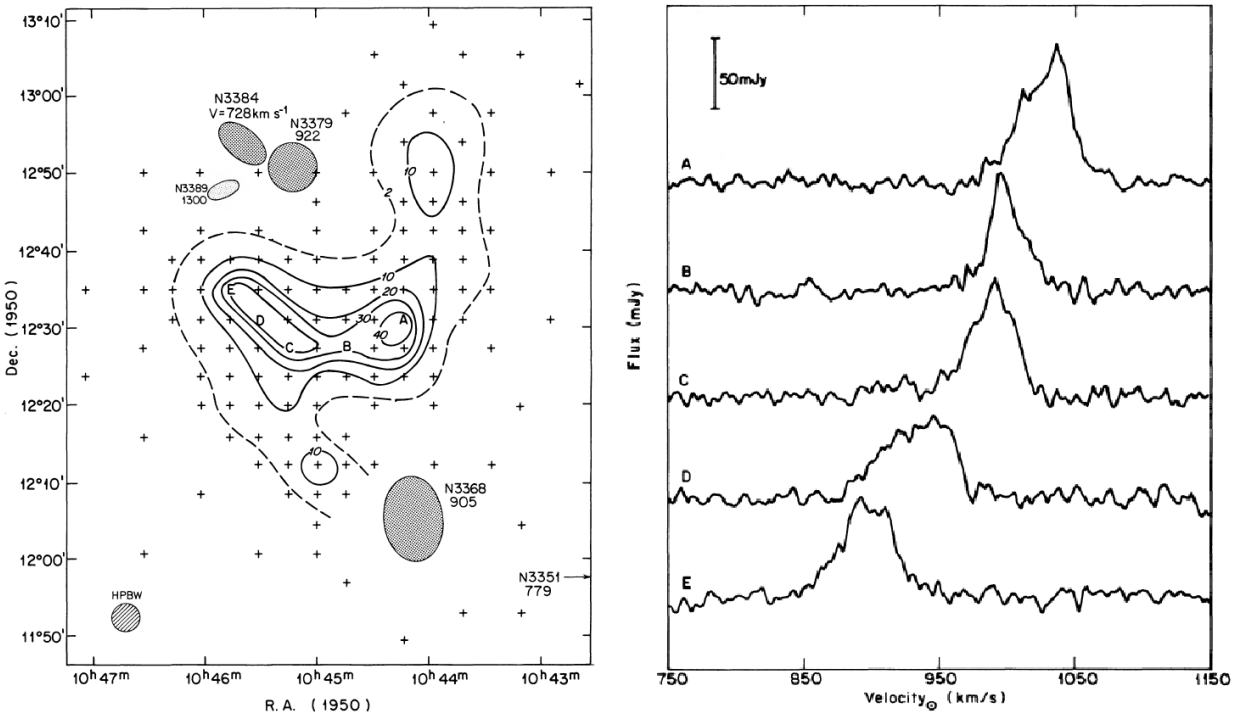

Figure 4: **Left panel**: *Fig 1* from Schneider et al. (1983). Neutral hydrogen map of the intergalactic cloud in the region of NGC 3368. The plus symbols indicate the locations where HI spectra were obtained. Contours are drawn in units of K kms^{-1}. The position and Holmberg dimensions of NGC 3368, NGC 3379, NGC 3384 and NGC 3389 are indicated with their heliocentric velocities. **Right panel**: *Fig 2* from Schneider et al. (1983). Five HI spectra (A to E) across the Leo intergalactic cloud at the corresponding positions indicated in the left panel in units of brightness temperature, 50 mJy $\sim$ 0.6 K.

The search for HI in 1985 (from S85) was also made using Arecibo 21 cm dual-circular polarisation feed. The data collection and reduction procedures were similar to the previous detection published in Schneider et al. (1983). However, the main difference between S85 and Schneider et al. (1983) is that S85 adopts overlapping 5 MHz spectra covering velocities from 200 to 2000 kms^{-1} with a resolution of 8 kms^{-1} and about 2.5 mJy noise level after Hanning smoothing. This new search found an additional 3 clouds (V through VII), providing a larger framework for interpreting the HI dynamics. The distribution of the HI from S85 is shown in the left panel of Figure 3, where the crosses mark the observed points. The contour levels indicate the integrated flux at $\int Tdv = 5$, 10, 20, and 40 K kms^{-1}. Local peaks, which is referred to as clouds, are labelled I through VII.

In S85, a proposed Keplerian model is shown for the clouds' radial velocities which can be seen in the right panel of Figure 3. The figure depicts the heliocentric velocities of the group members as well as the clouds with a fitted ellipse through clouds II-VII and a cross

marking the predicted focus.

The goal is to utilise the velocity profile from S85 as seen in the right panel of Figure 3 to investigate the dynamics of the HI structure.

2.2 Radial velocity

Most of what we know about the night sky comes from the information we receive from light. Of course, many important advances come from studies of meteorites, space probes in the solar system, detection of high-energy particles, gravitational waves and neutrinos, but the majority come from extracting information from photons. This puts many restrictions on observations and what properties of systems we are able to determine more easily than others. An example of this is the position on the sky which can be measured to great precision whilst the distance can only be approximated. For the time derivatives, in this case, it is the opposite since we are able to measure the Doppler shift motions along the line of sight. This allows us to determine motions of objects to great precision (Wright, 2018).

In fact, much of astronomy is concerned with the motion of objects which is a result of their mutual gravity. Hence, the use of radial velocities (line-of-sight velocity) is a cornerstone in astronomy. Its roots are found in the analysis of binary systems, where the radial velocity technique provides a mass estimate of the members. Additionally, it is the second most successful method of detecting exoplanets, where the line-of-sight gravitational acceleration of a star caused by orbiting planets are measured from Doppler shifts in the parent star's spectral features. The exoplanet detection is of course the low-mass limit of this application and one of the drawbacks of the technique is its sensitivity to mass. In exoplanet analysis, it often only provides an estimate of the minimum mass of the planet.

The work in the field of exoplanets is remarkably similar to the problem we are investigating in the Leo I group regardless of the scale difference. With the 3 new clouds (V-VII) discovered in S85, it was possible to test, in the words of Schneider (1985), *a naive orbit model by assuming that the gas lies along a single Keplerian orbit*. Similar to the exoplanets,

we make use of Kepler's laws to model the elliptical path of the gas and gain knowledge about the constraints this put on the mass in the focus. Unlike the star-planet system, the HI structure in Leo I is on much larger scales which makes it impossible to observe one full period/revolution for each cloud, thus emphasising the importance of the detection of clouds V-VII. Instead, the spatial distribution of the cloud can be considered as the same object at different orbital phases.

2.2.1 Deriving the line-of-sight velocity

In this section, we derive an expression for the line-of-sight velocity of objects moving along an elliptical orbit. Unfortunately, the use of the term radial velocity is often confused with the velocity component of the objects' total velocity vector extending in the radial direction from the orbital plane. To avoid confusion, we shall hereafter refer to the velocity in the observer's direction as the *line-of-sight velocity* and the radial component of the objects' velocity as *radial velocity*.

In order to derive the line-of-sight velocity, we must consider a traditional star-planet system of mass m_1 and m_2, respectively. The motion of the planet around its host star can be understood by solving a two-body problem. The solution to the problem was first presented by Sir Isaac Newton who showed that the elliptical path of a planet and the empirical laws of Kepler were a consequence of an inverse square law of force acting between the two bodies:

$$F = G\frac{m_1 m_2}{r^2}, \tag{1}$$

where $G = 6.6726 \cdot 10^{-11}\mathrm{Nm^2kg^{-2}}$ is the universal gravitational constant. A more complex task is to find the the position and velocity of an object in this problem. This is known as *Kepler's problem*. Using the basic equations of the two-body problem, we show how the elliptical motion arises and use them to solve Kepler's problem as outlined in Murray & Correia (2011).

Basic equations

We consider the star and planet system as illustrated in Figure 5 with position vectors $\boldsymbol{r}_1$ and $\boldsymbol{r}_2$ with respect to the origin O fixed in inertial space. The motion of the planet (m_2) is given by $\boldsymbol{r} = \boldsymbol{r}_2 - \boldsymbol{r}_1$. The gravitational forces acting on the two bodies are:

$$\boldsymbol{F}_1 = m_1\ddot{\boldsymbol{r}}_1 = +G\frac{m_1 m_2}{r^3}\boldsymbol{r} \tag{2}$$

$$\boldsymbol{F}_2 = m_2\ddot{\boldsymbol{r}}_2 = -G\frac{m_1 m_2}{r^3}\boldsymbol{r}, \tag{3}$$

respectively.

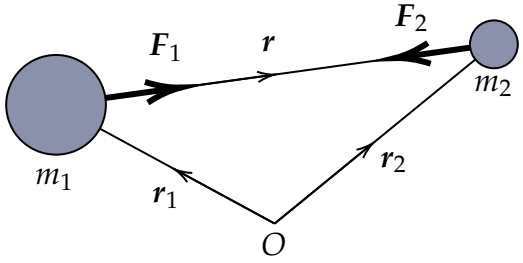

Figure 5: The forces acting on the two bodies of mass m_1 and m_2 with position vectors $\boldsymbol{r}_1$ and $\boldsymbol{r}_2$ (Murray & Correia, 2011).

We now consider the motion of the planet (m_2) with respect to the star (m_1). The equation $\ddot{\boldsymbol{r}} = \ddot{\boldsymbol{r}}_2 - \ddot{\boldsymbol{r}}_1$ combined with eq. (1) yields:

$$\ddot{\boldsymbol{r}} + G(m_1 + m_2)\frac{\boldsymbol{r}}{r^3} = 0. \tag{4}$$

The vector product of $\boldsymbol{r}$ with eq. (4) is $\boldsymbol{r} \times \ddot{\boldsymbol{r}} = 0$, which integrated gives:

$$\boldsymbol{r} \times \dot{\boldsymbol{r}} = \boldsymbol{h}. \tag{5}$$

$\boldsymbol{h}$ is a constant vector which is perpendicular to both $\boldsymbol{r}$ and $\dot{\boldsymbol{r}}$. This tells us that the motion about the star will always lie in the *orbital plane*. Additionally, this implies that the position and velocity vector will always lie in the same plane. Eq. (5) is also known as the *angular momentum integral* and $\boldsymbol{h}$ is one of the constants in the two-body problem (Murray & Correia, 2011).

In order to solve eq. (4), it is useful to transform to polar coordinates (r, f) with an origin centred at the star and a reference line corresponding to $f = 0$ as seen in Figure 6.

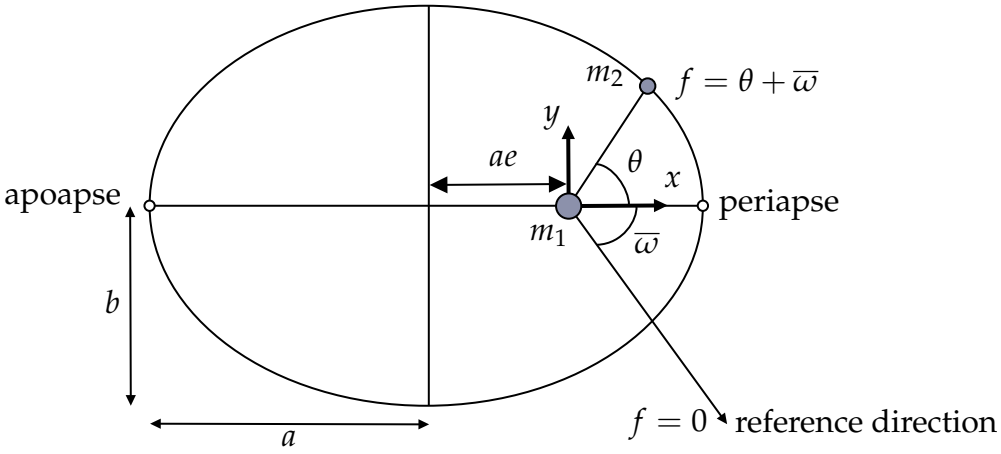

Figure 6: Geometry of the ellipse with semi-major axis a, semi-minor axis b, eccentricity e and longitude of periapse $\bar{\omega}$ (Murray & Correia, 2011).

In polar coordinates, we can express the position, velocity and acceleration as:

$$\boldsymbol{r} = r\hat{\boldsymbol{r}} \tag{6}$$

$$\dot{\boldsymbol{r}} = \dot{r}\hat{\boldsymbol{r}} + r\dot{f}\hat{f} \tag{7}$$

$$\ddot{\boldsymbol{r}} = (\ddot{r} - r\dot{f}^2)\hat{\boldsymbol{r}} + \left[\frac{1}{r}\frac{d}{dt}\left(r^2\dot{f}\right)\right]\hat{f}, \tag{8}$$

where $\hat{r}$ and $\hat{f}$ are the unit vectors along and perpendicular to the radius vector, respectively. If we substitute eq. (7) into eq. (5), we find $\boldsymbol{h} = r^2\dot{f}\hat{z}$, where $\hat{z}$ is the unit vector perpendicular to the orbital plane. The magnitude of this vector is:

$$h = r^2\dot{f}. \tag{9}$$

This leads to an interesting observation. The quantity $r^2\dot{f}$ is constant while both r and f vary as the body moves around its orbit. Consider the area element $\mathrm{d}A$ swept out by radius vector in time interval $\mathrm{d}t$. In polar coordinates its described as:

$$\mathrm{d}A = \int_0^r r\mathrm{d}r\mathrm{d}f = \frac{1}{2}r^2\mathrm{d}f. \tag{10}$$

Thus, we obtain

$$\dot{A} = \frac{1}{2} r^2 \dot{f} = \frac{1}{2} h = \text{constant}. \tag{11}$$

This is **Kepler's second law of planetary motion**, which states that the radius vector between the star and planet sweeps out equal areas in equal times.

If we now compare the radial component $\hat{r}$ of the radius vector in eqs. (4) and (8) using eq. (6), we find the differential equation:

$$\ddot{r} - r\dot{f}^2 = -\frac{G(m_1 + m_2)}{r^2}. \tag{12}$$

Using the substitution $u = 1/r$ and eq. (9), we can eliminate time in the differential equation. By expressing

$$\ddot{r} = -h \frac{\mathrm{d}^2 u}{\mathrm{d}f^2} \dot{f} = -h^2 u^2 \frac{\mathrm{d}^2 u}{\mathrm{d}f^2}, \tag{13}$$

we can rewrite eq. (12) as:

$$\frac{\mathrm{d}^2 u}{\mathrm{d}f^2} + u = \frac{G(m_1 + m_2)}{h^2}. \tag{14}$$

This second order differential equation has the general solution:

$$u = \frac{G(m_1 + m_2)}{h^2} \left[1 + e \cos(f - \bar{\omega})\right], \tag{15}$$

and is referred to as *Binet's equation* (Murray & Correia, 2011). The eccentricity, e, and the phase, $\bar{\omega}$, are two constants from integration. Substituting r back yields

$$r = \frac{p}{1 + e \cos(f - \bar{\omega})}, \tag{16}$$

where $p = h^2 / G(m_1 + m_2)$. We have then solved the differential equation to obtain r as a function of f. However, this is a general solution and the constant p is dependent on the initial conditions of the system. In the case of elliptical motion, it is given by:

$$p = a(1 - e^2) \tag{17}$$

where a is the semi-major axis of the ellipse. The semi-minor axis b can be expressed in terms of a and e by:

$$b^2 = a^2(1 - e^2). \tag{18}$$

The semi-major and semi-minor axes are shown in Figure 6. Inserting eq. (17) in eq. (16) gives

$$r = \frac{a(1 - e^2)}{1 + e\cos(f - \bar{\omega})}, \tag{19}$$

which is the equation of the ellipse in polar coordinates. Hence, the planet moves along an elliptical path around the star at one focus. This is **Kepler's first law of planetary motion**. From eq. (19), we find the minimum and maximum values of r at $r_p = a(1 - e)$ (at $f = \bar{\omega}$) and $r_a = a(1 + e)$ (at $f = \bar{\omega} + \pi$), respectively. The points are called *periapse* and *apoapse*, respectively (see Figure 6). The angle f indicates the true longitude of the orbit. $\bar{\omega}$ is the longitude of periapse of the orbit and corresponds to the angular location of the closest approach relative to the reference direction. We can now define the *true anomaly*, $\theta = f - \bar{\omega}$, which is then measured relative to the periapse direction. Eq. (19) then becomes:

$$r = \frac{a(1 - e^2)}{1 + e\cos\theta}. \tag{20}$$

Using the true anomaly, we define the Cartesian coordinate system centred on the star with the x-axis pointing towards the periapse as seen in Figure 6. The position vectors are given by $x = r\cos\theta$ and $y = r\sin\theta$.

Although we rid time from the equation of motion, we can relate the orbital period P to the semi-major axis a. The area of an ellipse is given by $A = \pi ab$, which is swept out in one period P. Given eq. (11), this is equal to $A = hP/2$. This yields

$$P^2 = \frac{4\pi^2}{G(m_1 + m_2)}a^3, \tag{21}$$

which is **Kepler's third law of planetary motion**. The relation show that the orbital period is independent of e and instead only depends on the masses of the two bodies and a.

We can define the mean motion of the orbit body as:

$$n = \frac{2\pi}{P}, \tag{22}$$

such that,

$$G(m_1 + m_2) = n^2 a^3 \tag{23}$$

$$h = na^2\sqrt{1-e^2} = \sqrt{G(m_1+m_2)a(1-e^2)}. \tag{24}$$

Finally, we wish to express the motion of the orbiting body. We write the following scalar equation:

$$\dot{\boldsymbol{r}} \cdot \ddot{\boldsymbol{r}} + G(m_1 + m_2)\frac{\dot{r}}{r^2} = 0, \tag{25}$$

by taking the scalar product of $\dot{\boldsymbol{r}}$ with eq. (4) and using the definitions in eqs. (6) and (7). Integrated, this yields

$$\frac{1}{2}v^2 - \frac{G(m_1+m_2)}{r} = C, \tag{26}$$

where $v^2 = \dot{\boldsymbol{r}} \cdot \dot{\boldsymbol{r}}$ and C is a constant. Eq. (26) shows that the orbital energy per unit mass of the system is conserved. Since $\bar{\omega}$ is a constant, $\dot{f} = \dot{\theta}$ gives

$$v^2 = \dot{\boldsymbol{r}} \cdot \dot{\boldsymbol{r}} = \dot{r}^2 + r^2\dot{\theta}^2. \tag{27}$$

Differentiating eq. (20) results in

$$\dot{r} = \frac{r\dot{\theta}e\sin\theta}{1 + e\cos\theta}, \tag{28}$$

which can be rewritten using eqs. (9) and (16) as:

$$\dot{r} = \frac{na}{\sqrt{1-e^2}}e\sin\theta, \tag{29}$$

and

$$r\dot{\theta} = \frac{na}{\sqrt{1-e^2}}\left(1 + e\cos\theta\right). \tag{30}$$

Inserting these two relations in eq. (27) then yields

$$v^2 = \frac{n^2 a^2}{1-e^2}\left(1 + 2e\cos\theta + e^2\right), \tag{31}$$

which shows the dependence of the velocity v on the true anomaly θ. This can further be manipulated to show the dependence of v on r as follows:

$$v^2 = G(m_1 + m_2)\left(\frac{2}{r} - \frac{1}{a}\right). \tag{32}$$

The velocity vector is also illustrated in Figure 7 and can be expressed as:

$$\boldsymbol{v} = \boldsymbol{v}_r + \boldsymbol{v}_\theta, \tag{33}$$

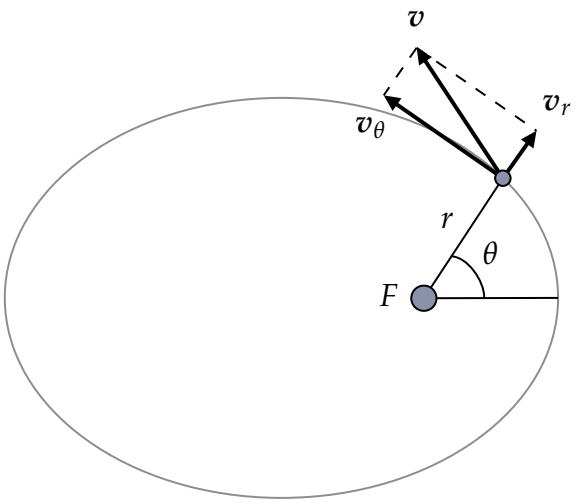

Figure 7: The velocity vector for elliptical motion in polar coordinates (Carroll & Ostlie, 2007). F denotes the focus.

where $\boldsymbol{v}_r$ is the radial component of the velocity and $\boldsymbol{v}_\theta$ is the azimuthal component. Using eqs. (9), (24) and (20), we may obtain an alternative definition of these components as

$$v_r = \dot{r} = \frac{h}{p}e\sin(\theta) = \frac{2A_{\text{orb}}e}{a(1-e^2)}\sin(\theta) \tag{34}$$

$$v_\theta = r\dot{f} = \frac{h}{r} = \frac{h}{p}\left[1 + e\cos(\theta)\right] = \frac{2A_{\text{orb}}}{r}, \tag{35}$$

where $A_{\rm orb} = \frac{1}{2}\sqrt{GMa(1-e^2)}$ is the areal velocity of the orbit. The total orbital energy may be found as well. The velocity at the periapse and apoapse can be written as:

$$v_{\rm p}^2 = \frac{G(m_1+m_2)(1+e)}{r_{\rm p}} = \frac{G(m_1+m_2)}{a}\left(\frac{1+e}{1-e}\right) \tag{36}$$

$$v_{\rm a}^2 = \frac{G(m_1+m_2)(1-e)}{r_{\rm a}} = \frac{G(m_1+m_2)}{a}\left(\frac{1-e}{1+e}\right), \tag{37}$$

$$\tag{38}$$

thus,

$$E_{\rm tot} = \frac{1}{2}\mu_{\rm r} v_p^2 - G\frac{(m_1+m_2)}{r_{\rm p}} \tag{39}$$

$$E_{\rm tot} = -G\frac{(m_1+m_2)\mu_{\rm r}}{2a} = -G\frac{m_1 m_2}{2a}, \tag{40}$$

where $\mu_{\rm r} = m_1 m_2/(m_1+m_2)$ is the reduced mass. The total energy of a binary orbit depends on the semi-major axis and is half the time-averaged potential energy of the system (Carroll & Ostlie, 2007):

$$E_{\rm tot} = \frac{1}{2}\langle U\rangle, \tag{41}$$

with $\langle U\rangle = -GM\mu_{\rm r}/a$ and denotes an average over one orbital period. Conservation of energy gives:

$$-G\frac{(m_1+m_2)\mu_{\rm r}}{2a} = \frac{1}{2}\mu_{\rm r} v^2 - G\frac{(m_1+m_2)\mu_{\rm r}}{r}. \tag{42}$$

This may be simplified to:

$$v^2 = G(m_1+m_2)\left(\frac{2}{r} - \frac{1}{a}\right). \tag{43}$$

Thus, the obtained expression for the total velocity in eq. (32) is also in agreement with that obtained from an energy perspective.

Solving the Kepler Problem

In the previous section, we introduced and solved the equation of motion for the two-body problem in the case of a planet orbiting a star. In the process, we obtained an expression for r as a function of θ. However, we have yet to determine r as a function of time, which is key to solving the Kepler problem (Murray & Correia, 2011). We, therefore, start by deriving an expression for $\dot{r}$ in terms of r. This can be done by using eqs. (20), (30) and (32) to rewrite eq. (27) as follows:

$$\dot{r}^2 = n^2 a^3 \left(\frac{2}{r} - \frac{1}{a}\right) - \frac{n^2 a^4 (1 - e^2)}{r^2}. \tag{44}$$

Simplifying the above equation results in:

$$\dot{r} = \frac{na}{r}\sqrt{a^2 e^2 - (r - a)^2}. \tag{45}$$

Before we can solve this differential equation, we must introduce a new variable, E, known as the eccentric anomaly. Whereas the true anomaly θ is measured with respect to the focus F, the eccentric anomaly measures the angle from the centre of the ellipse C with respect to the major axis. It can be more easily interpreted by drawing the auxiliary circle as shown in Figure 8.

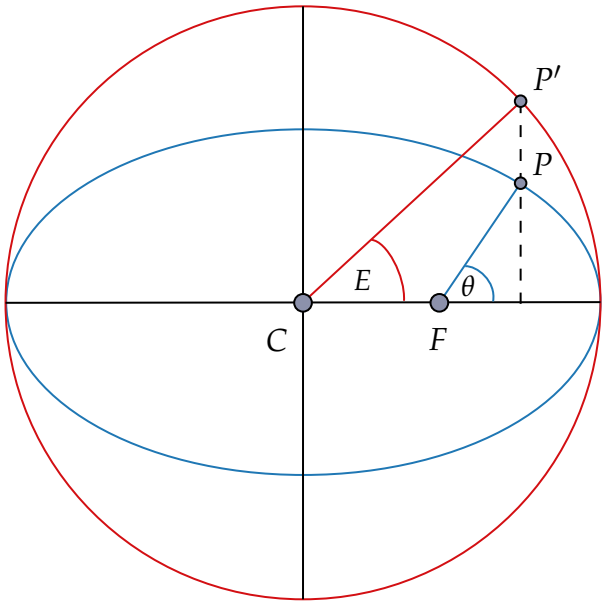

Figure 8: Illustration of the true anomaly θ and the eccentric anomaly E for point P along the elliptical path (in blue) with focus F and centre C. The red circle denotes the auxiliary circle.

The auxiliary circle is the projection of the ellipse when the y-component is divided by $\sqrt{1-e^2}$. The x- and y-coordinates in terms of E are as follows:

$$x = a\cos E \tag{46}$$

$$y = a\sqrt{1-e^2}\sin E. \tag{47}$$

The eccentric anomaly is very useful in the analysis we wish to conduct of the HI structure in the Leo I group as it is the angle we are able to match to the sky.

We can then express r as

$$r = a(1 - e\cos E), \tag{48}$$

which can be used to transform the differential equation

$$\dot{E} = \frac{n}{1 - e\cos E}, \tag{49}$$

with the solution

$$n(t - t_0) = E - e\sin E, \tag{50}$$

where t_0 is the constant of integration and determined from the boundary condition $E = 0$ when $t = t_0$. A third anomaly, M, the mean anomaly is defined as:

$$M = n(t - t_0), \tag{51}$$

where t_0 is the time of the passage of the periapse. M is hard to illustrate geometrically, but it is has the dimensions of an angle and it increases linearly with time. Additionally, $M = \theta = 0$ when $t = t_0$ or $t = t_0 + P$, and $M = \theta = \pi$ when $t = t_0 + P/2$. The eccentric anomaly and the true anomaly are connected via the following relation:

$$\tan\left(\frac{\theta}{2}\right) = \sqrt{\frac{1+e}{1-e}}\tan\left(\frac{E}{2}\right). \tag{52}$$

Likewise, the mean anomaly can be expressed in terms of the eccentric anomaly as:

$$M = E - e \sin E. \tag{53}$$

Eq. (53) is also known as *Kepler's equation* (Murray & Correia, 2011) and its solution is fundamental to the problem of finding the position along the orbital path for any given time. For a time t, we can determine M from eq. (51), find E from eq. (53), find r from eq. (48) and finally θ from eq. (20). This is typically done numerically, although this is not used for this analysis. For further information, we refer the interested reader to Danby (1988), where several numerical methods for its solution are provided.

The orbit in three dimensions

So far, we have defined four different orbital elements. Two of them, a and e, are related to the physical dimensions of the orbit. The other two, $\bar{\omega}$ and θ, are related to the orientation of the orbit relative to the reference direction and the location of the orbiting body. There are several alternatives to θ as mentioned previously, e.g. f and M. We now wish to extend the problem to three dimensions as illustrated in Figure 9.

The orbital motion is confined to the xy-plane as shown in Figure 6. The position vector is then:

$$\boldsymbol{r} = (x, y, 0) = x\hat{\boldsymbol{x}} + y\hat{\boldsymbol{y}} + 0\hat{\boldsymbol{z}}. \tag{54}$$

We then consider the plane of sky, with X- and Y-axes in the plane and Z-axis perpendicular corresponding to the direction of the observer (see Figure 9). The angle, i, denotes the inclination between the plane of orbit and plane of sky. The inclination is always in the range $0 \leq i \leq 180°$. The line that connects the intersection between the orbital path and the plane of sky is called the *line of nodes*. The *ascending node* is the point at which the orbit crosses the plane of sky, moving from below to above the plane. Vice versa, the *descending node* is the point at which the orbit crosses the plane, moving from above to below the plane. We define the **X**-axis to be the reference direction. The angle, Ω, is then the *longitude of the ascending node* between the reference line and the radius vector to

the ascending node. The angle between the radius vector to the ascending node and the periapse is called the *argument of periapse*, ω. We can then write:

$$\bar{\omega} = \Omega + \omega. \tag{55}$$

The orientation angles Ω, ω and i are illustrated in Figure 9.

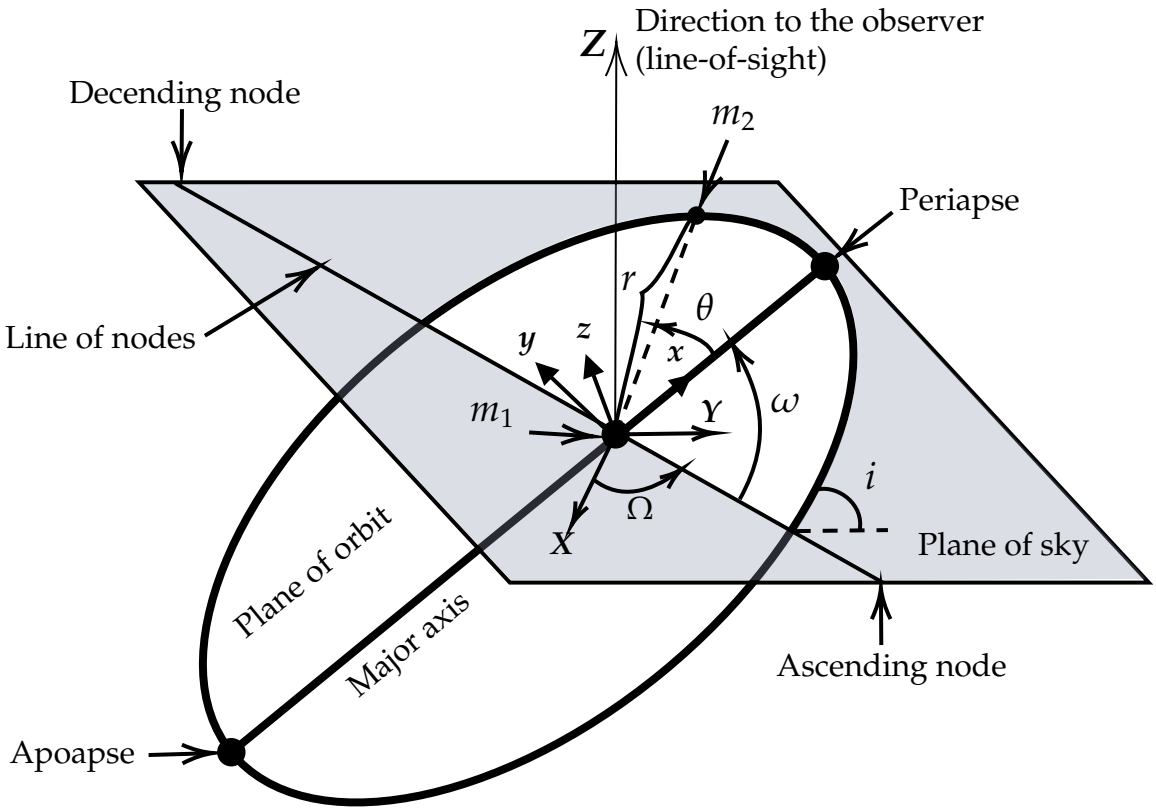

Figure 9: Illustration of mass, m_2, orbiting mass, m_1, in an elliptical with orbital parameters. x-, y- and z-axes are defined with respect to the plane of orbit. X-, Y- and Z-axes are defined with respect to the plane of sky.

We now look at the transformation between the (x, y, z)- and (X, Y, Z)-coordinate system in order to translate the motion in the orbital plane to the observed motion along the line of sight. The transformation is done in a series of rotation. First, a rotation about the z-axis using ω so that the x-axis is aligned with the line of nodes. Secondly, a rotation about the x-axis using i making the two planes coincident. Finally, a rotation about the z-axis through Ω. We can write up the transformations by two rotation matrices; $\mathbf{P}_x(\phi)$

for rotation about the x-axis, and $\mathbf{P}_z(\phi)$ for rotation about the z-axis:

$$\mathbf{P}_x(\phi) = \begin{pmatrix} 1 & 0 & 0 \\ 0 & \cos\phi & -\sin\phi \\ 0 & \sin\phi & \cos\phi \end{pmatrix} \tag{56}$$

and

$$\mathbf{P}_z(\phi) = \begin{pmatrix} \cos\phi & -\sin\phi & 0 \\ \sin\phi & \cos\phi & 0 \\ 0 & 0 & 1 \end{pmatrix}. \tag{57}$$

Thus,

$$\begin{pmatrix} X \\ Y \\ Z \end{pmatrix} = \mathbf{P}_z(\Omega)\mathbf{P}_x(i)\mathbf{P}_z(\omega) \begin{pmatrix} x \\ y \\ z \end{pmatrix}, \tag{58}$$

With $x = r\cos\theta$, $y = r\sin\theta$ and $z = 0$, we obtain:

$$X = r\left[\cos\Omega\cos(\omega+\theta) - \sin\Omega\sin(\omega+\theta)\cos i\right] \tag{59}$$

$$Y = r\left[\sin\Omega\cos(\omega+\theta) + \cos\Omega\sin(\omega+\theta)\cos i\right] \tag{60}$$

$$Z = r\sin(\omega+\theta)\sin i. \tag{61}$$

In order to determine the motion, it is useful to consider the motion in the centre of mass of the system as shown in Figure 10.

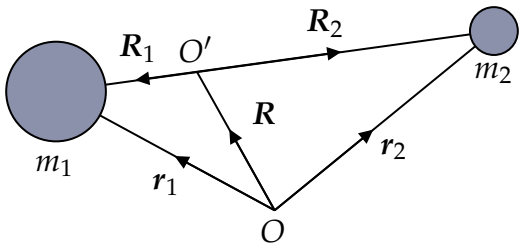

Figure 10: The position vectors of m_1 and m_2 with respect to the centre of mass O' and the origin O (Murray & Correia, 2011).

The position vector of the centre of mass is

$$\boldsymbol{R} = \frac{m_1\boldsymbol{r}_1 + m_2\boldsymbol{r}_2}{m_1 + m_2}. \tag{62}$$

From eqs. (2) and (3), we know that:

$$\ddot{\boldsymbol{R}} = \frac{m_1\ddot{\boldsymbol{r}}_1 + m_2\ddot{\boldsymbol{r}}_2}{m_1 + m_2} = 0. \tag{63}$$

From integration, we find $\dot{\boldsymbol{R}} = \boldsymbol{V} =$ constant. This implies that the centre of mass is stationary ($\boldsymbol{V} = 0$) or moving with constant velocity ($\boldsymbol{V} \neq 0$) in a straight line relative to the origin O. Since $\boldsymbol{R}_1 = \boldsymbol{r}_1 - \boldsymbol{R}$ and $\boldsymbol{R}_2 = \boldsymbol{r}_2 - \boldsymbol{R}$, we find:

$$m_1\mathbf{R}_1 + m_2\mathbf{R}_2 = 0. \tag{64}$$

The position vectors $\boldsymbol{R}_1$ and $\boldsymbol{R}_2$ are, therefore, always in opposite directions and the centre of mass is always positioned along the line between m_1 and m_2, thus:

$$R_1 + R_2 = r. \tag{65}$$

We can now determine the expression for the line-of-sight velocity, v_{los}. As the Z-axis is defined as the direction towards the observer, we may simply find the projection of the velocity vector along the line of sight. If we assume the centre of mass to be situated at m_1, we can write up the expression:

$$v_{\text{los}} = \boldsymbol{r} \cdot \hat{\boldsymbol{Z}} = v_0 + \dot{Z}, \tag{66}$$

where $v_0 = \boldsymbol{V} \cdot \hat{\boldsymbol{Z}}$ is the proper motion of the centre of mass. With the described transformation, we can obtain $\dot{Z}$ directly from eq. (61) as follows:

$$\dot{Z} = \dot{r}\sin(\omega + \theta)\sin i + r\dot{\theta}\cos(\omega + \theta)\sin i, \tag{67}$$

where we can write $\dot{r}$ and $r\dot{\theta}$ out explicitly using eqs. (29) and (30),

$$\dot{Z} = \frac{na\sin i}{\sqrt{1 - e^2}}\left[\cos(\omega + \theta) + e\cos\omega\right]. \tag{68}$$

We then find:

$$v_{\text{los}} = v_0 + K\left[\cos(\omega + \theta) + e\cos\omega\right], \tag{69}$$

where

$$K = \frac{na\sin i}{\sqrt{1-e^2}} = \frac{2\pi a\sin i}{P\sqrt{1-e^2}}. \tag{70}$$

K is also known as the *radial velocity semi-amplitude*. With a centre of mass shifted from m_1, K is reduced with a factor determined from the centre of mass of the two bodies and their individual mass. The derived expression in eq. (69) is consistent with the findings in Clubb (2008) and Ohta et al. (2005).

As mentioned when introducing the anomalies E and M, the eccentric anomaly, E, is the one that we can match to the plane of sky. One final step is, therefore, to apply the geometric conversion between θ and E from eq.(52). We then obtain the expression:

$$v_{\text{los}} = v_0 + K\left\{\cos\left[\omega + 2\arctan\left(\sqrt{\frac{1+e}{1-e}}\tan\left(\frac{E}{2}\right)\right)\right] + e\cos\omega\right\}. \tag{71}$$

Validation of model

In order to validate the expression found in eq. (69), we apply it to a famous example of the radial velocity method. With the exemption of the pulsar, PSR 1257+12, the star, Pegasi 51, was the first star found to have a planet orbiting it (other than the sun) (Carroll & Ostlie, 2007). It was first detected by M. Mayor and D. Queloz (Carroll & Ostlie, 2007) who found an orbital period of $P = 4.231$ days and a semi-major axis of $a = 0.052$ AU (Sylvain G. Korzennik, 1997). We have used observations of Pegasi 51 from AFOE (Advanced Fiber Optic Echelle Spectrometer, Sylvain G. Korzennik, 1997). We overplot the model from eq. (69) with the derived model parameters of Sylvain G. Korzennik (1997) as shown in Figure 11.

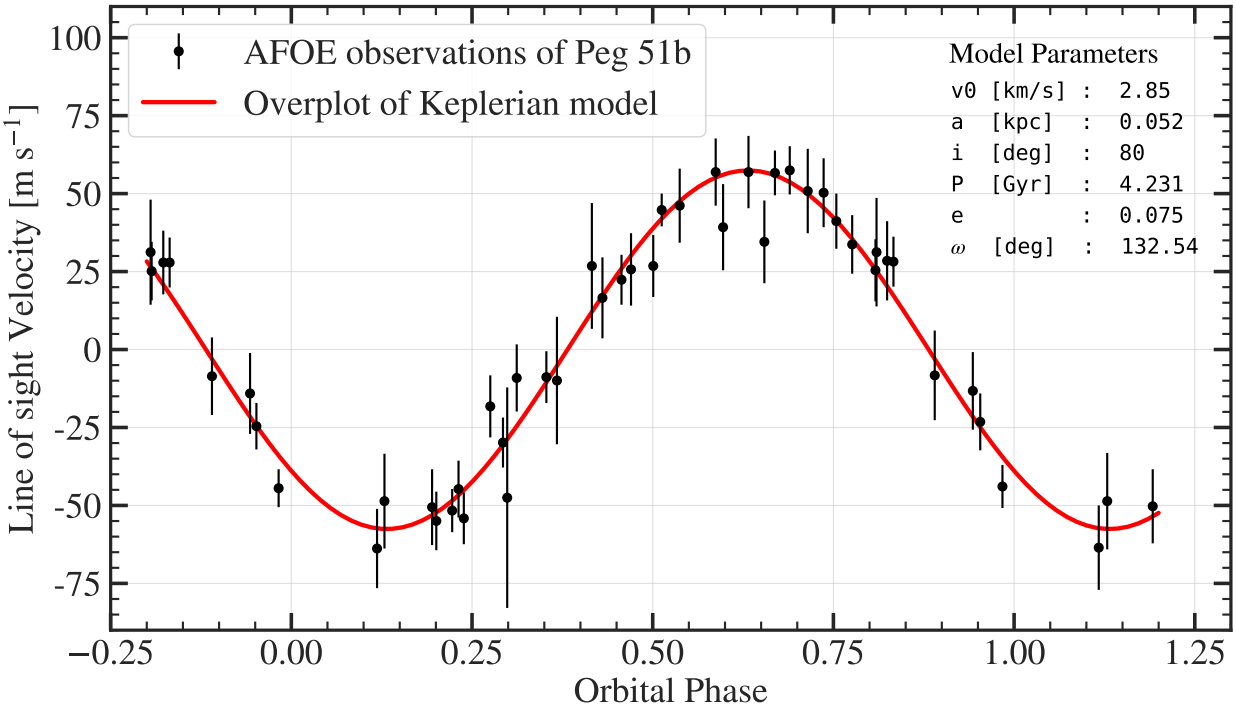

Figure 11: Measured line-of-sight velocities of Pegasi 51b from AFOE (Sylvain G. Korzennik, 1997) as a function of orbital phase (marked with black dots). The red curve shows an overplot of the Keplerian model from eq. (69), with the model parameters derived by AFOE (Sylvain G. Korzennik, 1997).

A comparison between the overplotted model (red curve in Figure 11) and the data shows a high level of agreement. We find a chi-square of $\chi^2 = 26.39$, reduced chi-square of $\chi^2_\nu = 0.61$ and a probability of the chi-square of $P(\chi^2) = 97.8\%$. We, therefore, accept the derived model for line-of-sight velocity.

We refrain from comparing the derived model with the previous solution by S85. This is explained in Appendix A.

2.3 Model fitting using nested sampling

Least-squares is a standard approach for regression analysis and is indeed a very powerful one. Essentially, given known x values and a corresponding set of y values with a given accuracy, one can determine unknown parameters of a function whose form is known. It does so by squaring the differences between the measurements and predicted values. Thus, greater importance is placed on removing the large deviations (Barlow,

1989). The chi square is then computed as follows:

$$\chi^2 = \sum_{i=1}^{N} \left[\frac{y_i - f(x_i; k_1, ..., k_n)}{\sigma_i} \right]^2, \tag{72}$$

where f is the predicted value for x_i with its parameters $k_1, ..., k_n$. The parameters are chosen by minimising the χ^2.

This method is computationally very fast and will work great given proper bounds on the parameters. In a multi-modal problem, the fitting problem becomes more complex as we wish to converge towards the global minimum. Many algorithms, including the method of least-squares, are prone to getting stuck in local minima. Hence, we adopt a more complex fitting procedure.

Using nested sampling, we are able to examine the parameter space at multiple points at once. Nested sampling is a computational approach to Bayesian statistics problems and can be use to generate points from a posterior distribution given a likelihood and prior. This can be used in regression analysis as well. The background for nested sampling is Bayes' Theorem (Buchner, 2021):

$$P(A|B) = \frac{P(B|A)P(A)}{P(B)}, \tag{73}$$

where $P(A|B)$ is the posterior, $P(B|A)$ is the likelihood, $P(A)$ is the prior and $P(B)$ is the marginal likelihood. In nested sampling, the marginal likelihood is also called the evidence, z. The ratio z_1/z_0 for two hypotheses H_1 (alternate hypothesis) and H_0 (null hypothesis) is called the *Bayes factor*, and is a useful tool for model comparison.

Similar to the least-squares approach, we require known uncertainties on the measurements. However, the data from S85 does not have stated uncertainties. From the radial velocity pattern in Figure 3, we find the velocities to be given in steps of 10 km/s with a few exemptions down to 5 km/s. We, therefore, adopt a conservative uncertainty of ± 10 km/s for all the data points. This provides us with the likelihood, where each data point follows a Gaussian distribution. We employ a flat prior for each parameter of interest

by assigning bounds that define the region of the parameter space to be sampled by the algorithm.

We use the package ULTRANEST (Buchner, 2021), which is written in PYTHON. A brief explanation of the algorithm is provided in Appendix B, although we reference Buchner (2021) for the full documentation.

From the posterior samples, we can obtain the best-fitting parameter values that maximise the likelihood. These are not necessarily equal to the ones for the mean or median of the parameters' distributions. For this problem, we have very few data points. This is not ideal as low statistics influence the quality of the fit. The least-squares method is, therefore, also much cheaper computationally compared to the nested sampling approach. However, the exploration of the parameter space in nested sampling gives us a more robust result, along with a better understanding of possible degeneracies.

2.4 Results

In this section, we present the results from applying the described nested sampling technique to the data using the derived model from eq. (69). The flat prior, which sets the bounds on each parameter, is shown in Table 2.

Table 2: Flat priors employed in nested sampling

Parameter	Lower Bound	Upper Bound
v_0 [km/s]	200	2000
a [kpc]	80	120
i [degrees]	0	180
P [Gyr]	2	7
e	0	<1
ω [degrees]	0	360

The choice of prior is crucial for obtaining a proper fit. Some model parameters are bounded by definition; $0° \leq i \leq 180°$, $0° \leq \omega \leq 360°$ and $0 \leq e < 1$. The proper

motion of the centre of mass, v_0, is bounded by the range from observation (200 to 2000 kms^{-1}). In Figure 3, the distance scale of 50 kpc is determined from an assumed distance of 10 Mpc. This provides a rough estimate on the bounds of the semi-major axis, which may vary depending on the inclination.

However, given the distribution of the clouds, the apoapse is ill-defined compared to the periapse. This creates a convergence towards higher values of a if not bounded. If we consider the radial velocity semi-amplitude from eq. (70):

$$K = \frac{2\pi a \sin i}{P\sqrt{1-e^2}},$$

we find a complex relation between the 3 parameters P, a and i as they are degenerate. If we were able to determine one of these parameters independently, it would constrain the others and allow for more straightforward interpretation. However, since the actual distance to each cloud is not actually included, we are left with many possibilities for the size of the semi-major axis. Of these three parameters, a is the one we are able to constrain the most. The lower bound is set to 80 kpc, which is slightly smaller than the semi-major axis projected onto the sky plane. The upper bound is not as straightforward. If we consider Kepler's third law of planetary motion from eq. (21), we can obtain the total mass of the system, M, as follows:

$$P^2 = \frac{4\pi^2}{GM}a^3$$

$$\Leftrightarrow M = \frac{4\pi^2}{G}\frac{a^3}{P^2}. \tag{74}$$

The mass must be bounded as well. The main assumption is that the HI structure orbits NGC 3379. The mass of NGC 3379 is of order $10^{11}M_\odot$, which is our lower bound. From Kepler's third law, we find $M \propto a^3/P^2$. The lower bound on the mass then corresponds to the lower bound on a and the upper bound on P. For the upper bound on the mass, we do not set any conditions from a physical perspective, but restrict it to an order-of-magnitude of $10^{13}M_\odot$, which is larger than the expected virial mass for such a system. This ensures

that we cover all scenarios while optimising the computing time of the fit. Note that the lower bound P is determined from this bound as lower values would converge quickly towards a non-physical scenario.

Given the measurements y and the predicted value f_i, we write the log-likelihood for a Gaussian distribution in eq. (75):

$$\mathcal{L} = -\frac{1}{2}\sum\left(\frac{y_i - f_i}{\sigma_i}\right)^2. \tag{75}$$

We set the number of live points to $N_{\text{live points}} = 12000$[1] and require at least 40 points to be sampled for each detected cluster. Additionally, we run with 10 test samples to catch bugs. The maximum likelihood best-fitting parameters is presented in Table 3.

Table 3: Maximum likelihood best-fitting parameters

Parameter	Value
v_0 [km/s]	834 ± 5
a [kpc]	100 ± 10
i [degrees]	50 ± 40
P [Gyr]	5 ± 1
e	0.58 ± 0.06
ω [degrees]	297 ± 3

In Figure 12, the parameter space is shown with the sampled distribution for each parameter. The best-fitting parameters are marked with the red lines/dots and the median is shown in the title of each histogram with estimated upper and lower uncertainties. The black dashed lines indicate the 1σ interval from the median. The red lines/dots indicate the maximum likelihood best-fitting parameters from Table 3. The contours show the 2D sigma level. Within the 1-sigma level of 1D distributions, the Gaussian contains 39.3% of the volume. As such, the relevant sigma levels for 2D histograms is 39% and not 68%.

[1]Live point is the term adopted by UltraNest for sampled points within an ellipsoid (see Appendix B).

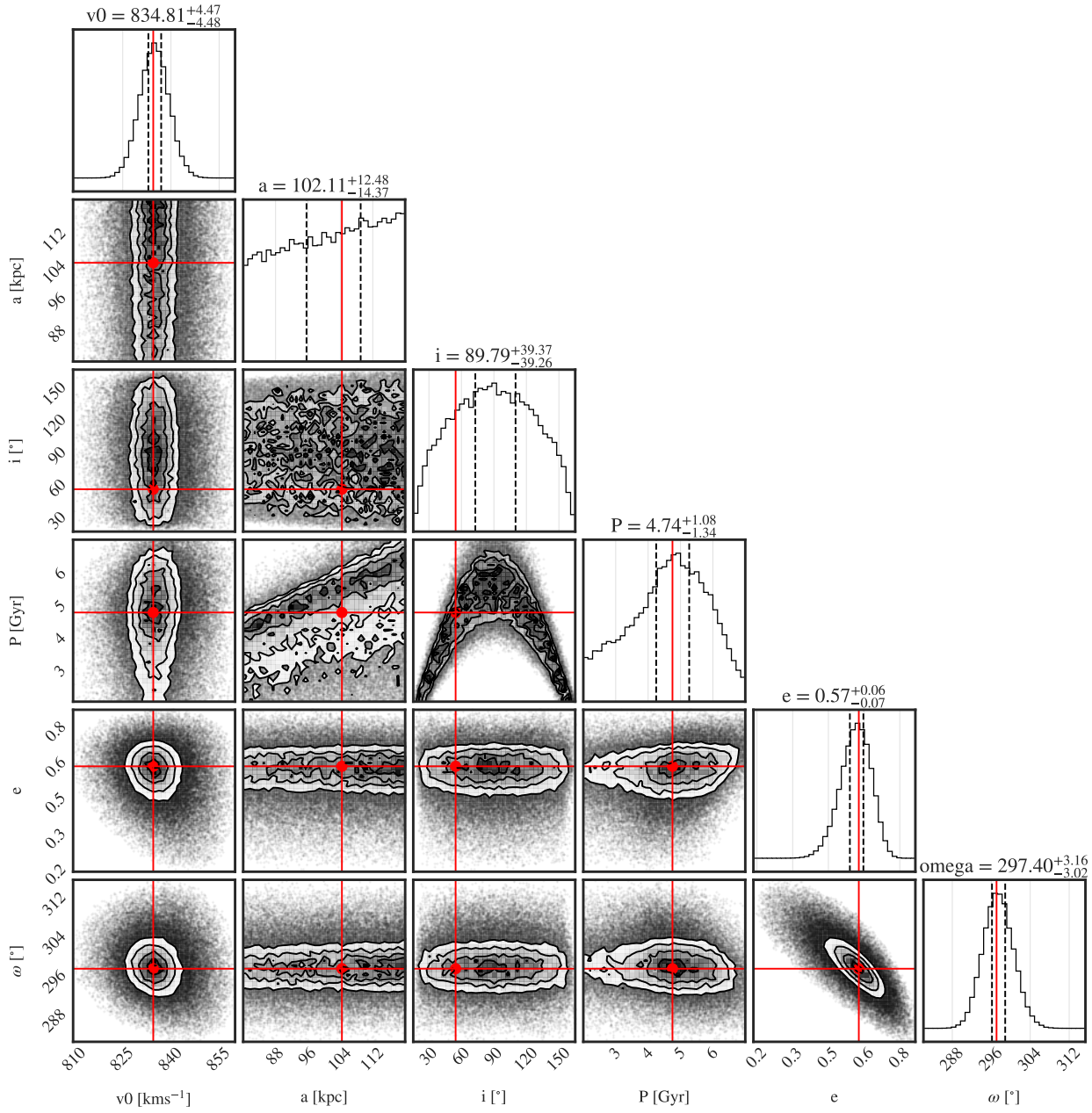

Figure 12: Corner plot of the parameter space explored via nested sampling. Titles of each histogram shows the median value of the distribution with estimated upper and lower uncertainty. Black dashed lines on the distributions show the 1σ interval from the median. Red lines/dots indicate the maximum likelihood best fit parameters from Table 3. 35 bins is used for each histogram. The contours show the 2D sigma level. Within the 1-sigma level of 1D distributions, the Gaussian contains 39.3% of the volume.

If we consider v_0, e and ω, we see that their distributions are quite narrow. Furthermore, the sampled regions of the joint probability distributions of (v_0, e), (v_0, ω) and (e, ω), all show a clear Gaussian shape with a well-determined peak. The estimated uncertainties on these parameters are, therefore, relatively low.

The landscapes for a, i and P are more complex as expected from the considerations about the prior. If we consider the landscape of the orbital period, it would seem as if we have probed the most populated part of the landscape compared to the well-determined parameters (v_0, e and ω). The uncertainty, however, is quite large on this parameter. This is also seen on its wide and skewed distribution. The left tail in its distribution is caused by the convergence toward higher mass solutions.

Similarly, we find the inclination to be poorly determined. This is expected as the viewing angle is hard to determine.

The semi-major axis is particularly complex. The sampled regions of (a, P), (a, i) and (P, i) all show ill-defined distributions. Note that the inclination is symmetric about 90°, thereby providing two solutions to the same model, e.g. a value of $(120 \pm 40)^\circ$ can also be interpreted as $(60 \pm 40)^\circ$.

The complex parameter space gives a clear indication as to what we can expect for the goodness of the fit. The maximum likelihood parameters of P, i and a may vary from run to run, even though we employed nested sampling. Re-running the algorithm with the same initial conditions results in the same values for v_0, e and ω. This is shown in Figures 36 and 37 (see Appendix C).

Additionally, to emphasise the effects of the prior, we have run looser bounds on the semi-major axis with (50 kpc $\leq a \leq$ 180 kpc) and (0.8 Gyr $\leq P \leq$ 10 Gyr), thus not accounting for the boundary on the mass. As seen in Figures 38 and 39, this drastically increases the uncertainties on a and P.

In Figure 13, the resulting maximum likelihood fit is indicated by the solid black line. The red, blue and green bands indicate the 1, 2, and 3σ prediction bands, respectively. A χ^2-test yields a value 44.92 and a reduced chi-square $\chi^2_\nu = 6.42$. The resulting probability of the chi-square is $P(\chi^2, \mathrm{N_{dof}} = 7) = 0$. Recall that we assumed a conservative uncertainty of $\pm$10 km/s. Since the true uncertainty might be lower, it is unlikely that we are able to improve upon the fit.

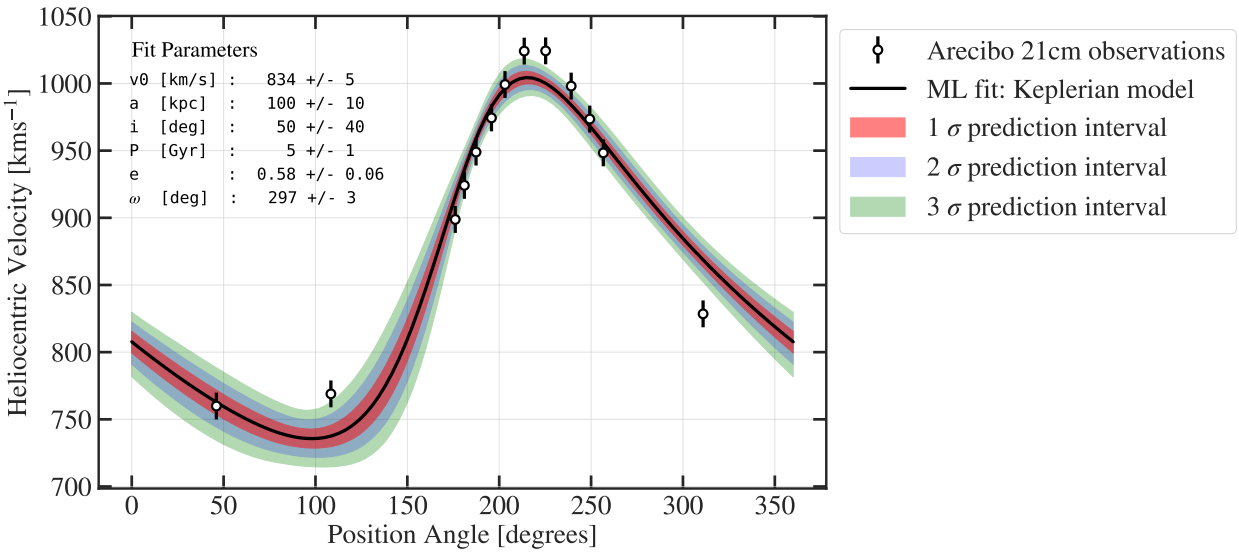

Figure 13: Keplerian model of the line-of-sight velocities for the intergalactic gas ring. The heliocentric velocity of clouds II-VII in km/s is plotted versus the position angle (eccentric anomaly) relative to the center of the proposed ellipse. The solid black line shows the fit with the maximum likelihood best fit parameters in Table 3. These are also noted in the figure. The red, blue and green coloured regions show the 1, 2 and 3σ region from the maximum likelihood. Note that the position angle (eccentric anomaly) is shifted 180° relative to the periapse.

The derived model does not fit the data well with multiple outliers beyond the 3σ confidence region. When comparing with the overplot of the model to the velocities of Pegasi 51b in Figure 11, it is clear that the model does not fit nearly as well to the HI structure.

Given the derived parameters, we can compute several other parameters. The position angle of the periapse would be equal to the maximum velocity. We find it to be $PA_{\text{periastron}} = 215^{+62}_{-36}$ deg. Note that the curve shown in Figure 13 is quite asymmetric around the peak, which makes it difficult to determine an uncertainty. We have used Full Width Half Maximum (FWHM), although strictly speaking this is only for a Gaussian function.

Using eq. (74), we find $M = (4 \pm 3) \cdot 10^{11} M_\odot$. The propagated error on the mass is quite large as expected given the uncertainties on the semi-major axis and the orbital period. With $L_{\text{NGC 3379}} = 2.2 \cdot 10^{10} L_\odot$ and $L_{\text{NGC 3384}} = 5.81 \cdot 10^9 L_\odot$ (Cappellari et al., 2006), this yields a mass-to-light ratio of $M/L_V = (14 \pm 11) \frac{M_\odot}{L_\odot}$ in the visible band.

Finally, we determine the distance from the centre of the ellipse to the focus. Using $c = ae$, we find a distance of $c = (60 \pm 10)$ kpc. We can subsequently conclude that the focus will

not lie in the same location as marked on Figure 3, which is around 36 kpc (S85), but rather closer to clouds II-IV.

The orbital period is significantly larger than the mean crossing time of Leo I estimated at $t_{\text{cross}} \approx 2.7$ Gyr (Karachentsev & Karachentseva, 2004), which questions the ring's stability. Additionally, the computed mass and mass-to-light ratio are relatively low. The outer parts of elliptical galaxies consist mainly of dark matter and from Sparke & Gallagher (2007), we would expect $M/L_V \approx 50$ within 50 kpc of the centre. The constraints, therefore, imply a significant amount of matter is missing from the system compared to what is expected from a traditional dark matter distribution extending from a galaxy.

Furthermore, considering the alternative fits in Appendix C, the goodness of fit is very similar, casting some doubt on the robustness of the fit as it becomes increasingly unlikely with multiple combinations of the orbital parameters providing the same result. Especially in the case of the Keplerian model, which is physically well-understood and should provide one unique solution.

2.5 Discussion on the dynamics of the Leo ring

We find a disagreement between the Keplerian model and the velocity profile of the intergalactic gas in Leo I. A closer look at the contours of the gas would suggest that the majority of the gas is located at the periapse of the supposed ellipse, which could follow a partial Keplerian behaviour in that region. However, we reject the Keplerian model and the overall picture, therefore, indicates that the ring is not primordial, but rather a transient phenomenon. Importantly, the Keplerian model relies heavily on the focus to be close to NGC 3379 and/or NGC3384. However, from the determined ellipse, this is not the case. Additionally, we do not find any object in the system that would suggest removal of an individual cloud which, in turn, could alter the results. Ideally, the distance to each cloud would be known as this would provide more accurate constraints on the semi-major axis, which could improve the fit.

The dynamics of the system must follow a more complex model and we, therefore, do not necessarily find a link between NGC 3379 and NGC 3368. This reveals the possibility for

more complex models of the mass. If the Keplerian model was valid, we would expect all mass to be confined within the focus. We find the derived M/L constraint invalid as we would expect a dark matter distribution to extend in this region.

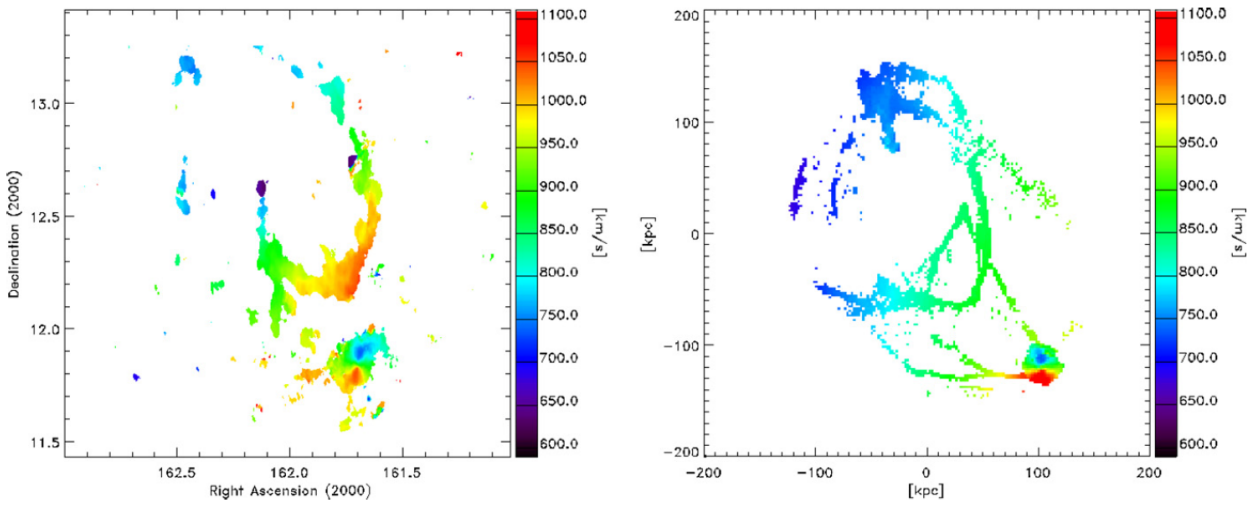

Figure 14: Figure 4 from Michel-Dansac et al. (2010): **Left**: Velocity field of the HI gas, as mapped by the WSRT. The field of view is 400 × 400 kpc, assuming a distance of 11.6 Mpc. **Right**: Velocity field of the gas in the numerical model of the collisional ring.

The origin of the ring is heavily debated. Oosterloo et al. (2010) suggest that the HI structure is a spiral caused by collision. This is further analysed in Michel-Dansac et al. (2010), in which a head-on collision between NGC 3384 and NGC 3368 is simulated. They find the structure to be consistent with the collision model. Michel-Dansac et al. (2010) use newer data from the group as presented in Oosterloo et al. (2010), in which the spiral seems to originate at NGC 3384 and spiral towards NGC 3368 where the gas is more diffuse. Results from Michel-Dansac et al. (2010) that illustrate this is shown in Figure 14. The model is based on an expanding gas ring with mostly NGC 3384 material, which through 1.2 Gyr of evolution, reproduces the main observational features such as size, mass, column density and the asymmetry of the HI structure. This collisional model is a possible explanation as to why cloud I, as seen in Figure 3, is shifted from the others creating the so-called 'S'-symmetry.

3 The structure and kinematics of the Leo I group

Galaxy groups and clusters are the largest known gravitationally bound objects that are formed in the process of cosmic structure formation (Voit, 2005). They may contain ten to thousands of individual galaxies and, as such, are powerful tracers for the distribution of matter on the largest scales. Thus, understanding key properties from their structure allows us to measure properties of the Universe itself.

In the cosmological context under investigation in this thesis, we must accurately determine the distance to the members of the Leo I group in order to step out to larger distances, from which we can determine the Hubble constant.

Although the problem might seem simple, it is complicated due to the number of members in Leo I. In the previous section (see Section 2), we found the link between NGC 3379, NGC 3368 and NGC 3384 to be questionable. That assumption, however, was useful since we could independently measure the same distance from 3 different observations. Based on the conclusions from analysing the HI structure in Leo I, we must re-analyse the structure of the Leo I group and gain the necessary insight needed for determining accurate distances to the group and each of its members.

In addition, we will investigate the recessional velocities of the members in the group. The dynamics of the group allows us to put constraints on mass. This will provide an insight into the likelihood that the probed members are in fact part of the group, the dark matter content and the stability of the group.

3.1 The cosmic distance ladder

The phenomena we investigate in the Universe all unfold on a two-dimensional stage. Observations supply the coordinates, right ascension and declination, that describe the position of the object on the celestial sphere. The distance to the object is not so easily obtained and depends on a variety of techniques. These techniques rely on properties that range from individual stars to larger structures such as globular clusters, planetary nebulae, supernovae and HII regions, and some on whole galaxies and galaxy clusters. The third dimension of distance is of great significance in astronomy. It provides important information about the position of celestial objects, but as we peer deeper into space, we also observe more ancient light. It is, therefore, vital to not only know the position, but the depth in time as well so as to understand the underlying physics.

In 1761, the method of trigonometric parallax was used to measure the distance to Venus, which, in turn, was used to calibrate the size of the Kepler's Solar System (Carroll & Ostlie, 2007). In 1962, Friedrich Wilhelm Bessel measured the shift in the position of the star 61 Cygni. He combined trigonometric parallax with the calibrated size of Earth's orbit and determined that the star was 650,000 times more distant than the sun (Carroll & Ostlie, 2007). The parallax method is today useful within 200 pc, but distances to nearer planets can be determined within a few kilometres by measuring the round-trip time taken by radio waves sent from Earth and reflected back from the planet's surface. This is very limited as the strength of the reflected wave diminishes as $1/r^4$ (Carroll & Ostlie, 2007).

Stepping further out, distances to stellar clusters have been determined from the moving cluster method, for e.g. the Hyades star cluster. From there, main-sequence fitting has been used to determine the distance to open clusters out to about 7 kpc by comparing their main sequences on an H-R diagram with that of the Hyades cluster (Carroll & Ostlie, 2007).

This repeated pattern of calibration and measurements through a variety of methods constitutes the *cosmological distance ladder*. The methods described are only applicable within relatively small distance scales compared to that of the Leo I group. From the observa-

tions described in S85, we know that the distance to the group is of order 10^1 Mpc. This immediately gives us an indication of what techniques may be used. At this scale, we are unable to make direct measurements and we, therefore, rely on secondary distance indicators. In other words, these indicators require a galaxy with an established distance for their calibration. Furthermore, we find both early- and late-type galaxies in the group and consequently, different methods apply. In basic terms, all methods we apply at this distance scale rely on some known light source with a well-determined absolute magnitude, M. We can then obtain a distance through the distance modulus by comparing it to the apparent magnitude, m:

$$D_{\mathrm{L}} = 10^{\frac{\mu}{5}+1}, \tag{76}$$

where D_{L} is the luminosity distance in parsecs and $\mu = m - M$ is the distance modulus.

When investigating the structure of the group, we focus on *relative distance* measurements to the members. Given the differences between observational technique and calibration, we cannot obtain a clear insight into the structure as we introduce systematic uncertainty. The relative distances are free from this uncertainty by adopting the same technique, calibration and preferably the same detector. We adopt the method of Cepheids, Tip of the Red Giant Branch (TRGB) and Surface Brightness Fluctuation (SBF) as these have been shown to be the most common, precise and well-understood mechanisms available. Additionally, a type Ia supernova, SN1998bu, was found in NGC 3368 (Cappellaro et al., 2001), although this particular supernova is subject to high reddening.

In the following sections, we describe the background of each method and how it is calibrated.

3.1.1 Cepheid variables as distance indicators

In 1595, the star, *o* Ceti, was observed over a period of several months. The amateur astronomer David Fabricius found that the brightness of the star slowly faded until the star completely vanished from the sky before returning months after (Carroll & Ostlie, 2007). Although the phenomenon was thought to be caused by dark patches on the surface of a rotating star, we know today that it is a *pulsating star*, a star that dims and brightens as its

surface expands and contracts. *o* Ceti has a pulsation period of 11 months and is one of the long-period variables (Carroll & Ostlie, 2007).

Later, the *classical Cepheids* were found which have regular periods on the order of days to months. An example of such Cepheid is δ Cepheid whose light curve is shown in Figure 15. Classical Cepheids may have small fluctuations within a few magnitudes as seen on Figure 15. Classical Cepheids are Population I variable stars which range from 4 to 20 times the mass of the Sun and even 100,000 times more luminous. They are bright yellow giants or supergiants which range in spectral class from F6 to K2 (Carroll & Ostlie, 2007).

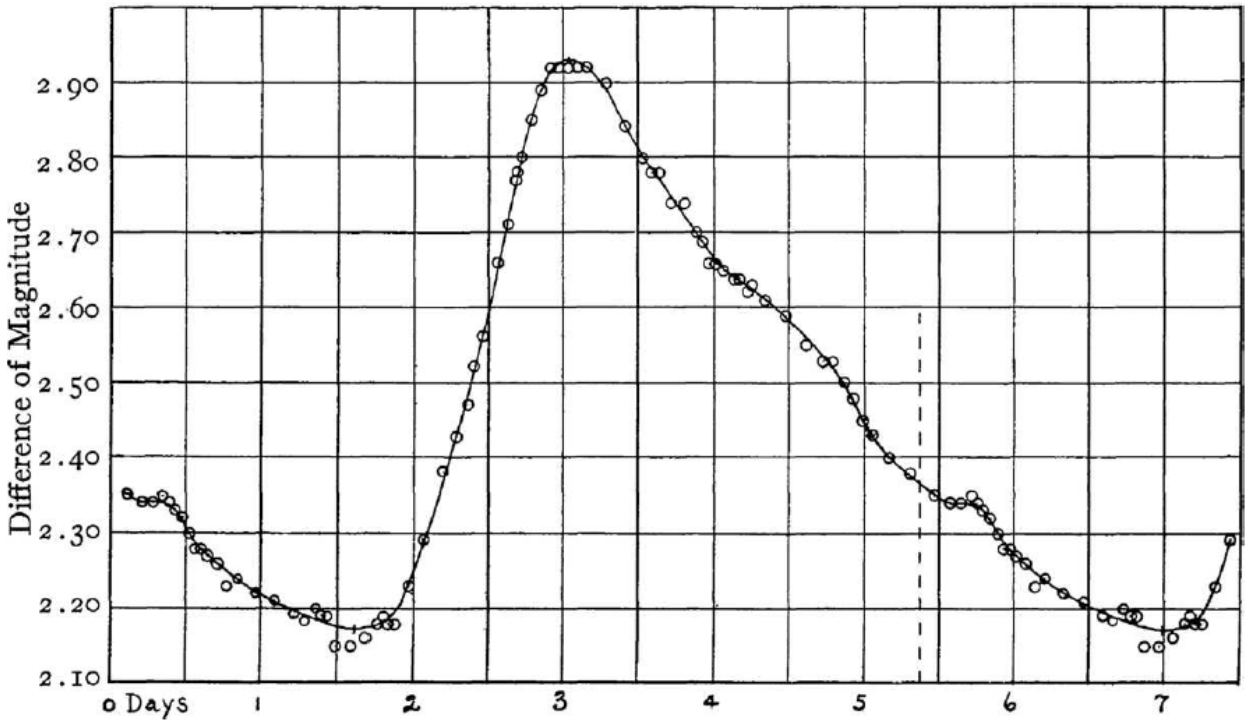

Figure 15: Figure 14.2 from Carroll & Ostlie (2007). The light curve of δ Cephei. Its pulsation period is 5.37 days.

The Period-Luminosity relation

Henrietta Swan Leavitt is a great contributor to the study of Cepheids. In 2005, nearly 40,000 pulsating stars had been catalogued of which she had discovered more than 5% (Carroll & Ostlie, 2007). Leavitt studied classical Cepheids in the Small Magellanic Cloud (SMC) and noticed that more luminous Cepheids took longer to complete their pulsation cycle. She plotted the apparent magnitudes against their pulsation periods. This is shown

in Figure 16.

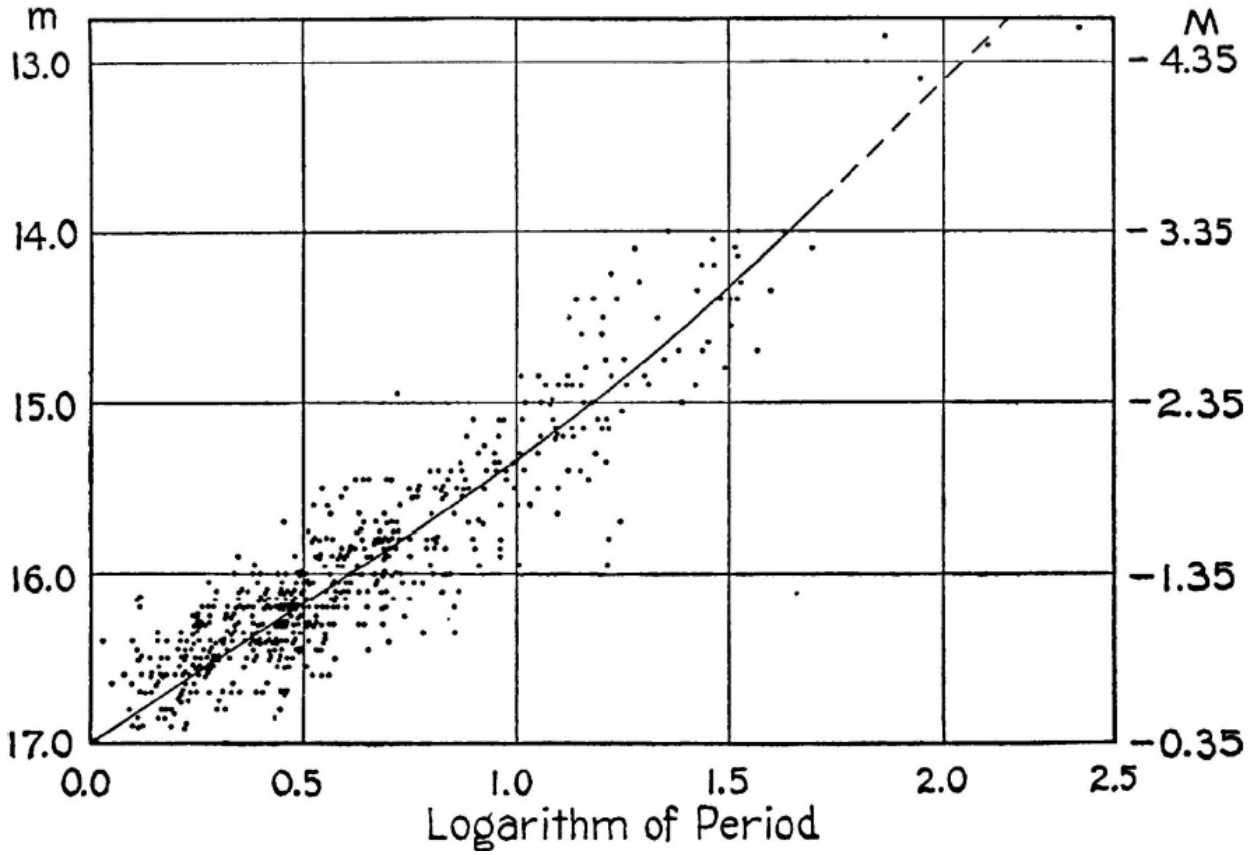

Figure 16: Figure 14.4 from Carroll & Ostlie (2007). Classical Cepheids in the Small Magellanic Cloud. The period is in units of days.

The resulting graph in Figure 16 shows how the apparent magnitude of the classical Cepheids are correlated with their periods. Since these Cepheids are all in the SMC at roughly 61 kpc, the differences in their apparent magnitudes must be the same as in their absolute magnitudes. The observed differences in the stars' apparent magnitudes, therefore, reflect intrinsic differences in their luminosity. Leavitt's relation allows us to find the absolute magnitude of a classical Cepheid simply by timing its pulsation. Hence, it became a useful tool for determining distances, as distances are easily obtained from the distance modulus (eq. (76)) once the apparent and absolute magnitudes are known.

In Appendix D, we describe some classes of Cepheids and their position on the HR-diagram. In addition, we explain how to obtain the pulsation period as a function of the mean density of the star and the physics of stellar pulsation.

Calibrating the Period-Luminosity relation

Distances to classical Cepheids have been measured directly from the parallax method, providing a strong basis for calibrating the Period-Luminosity relation. The scatter of the relation, as depicted in Figure 16, can be reduced by making observations in the infrared band where extinctions becomes less significant. Additionally, adding a colour-term reduces the scatter even further. Thus, today it is in fact a *Period-Luminosity-Colour* (PLC) relation, even though it is often referred to as the Period-Luminosity relation. The absolute magnitude can be expressed as:

$$M = \alpha \log P + \beta C_0 + \gamma \tag{77}$$

where C_0 is the intrinsic colour and P is the pulsation period[2]. The slopes α and β, as well as the zero-point γ all depend on the observed band and distance.

Recall that the calibration is important when comparing relative distances. For the Cepheid-based distances in Leo I, we make use of two different calibrations as both are suitable for such analysis. The first calibration is outlined in Paturel et al. (2002a). They note how the slopes of the PLC-relation differ for the Milky Way and the Large Magellanic Cloud (LMC), since the PLC-relation also has a weak dependence on metallicity. The choice of slope in different bands is, therefore, difficult. In Paturel et al. (2002a), they avoid this dilemma by applying the method of *sosie*, as this does not require knowledge of the slope and zero point of the PLC-relation. The method of sosie is named after the French word sosie, meaning someone who looks similar to someone else without being genetically related. This idea applies for the Cepheids by comparing their light curves and periods. Two Cepheids are considered sosie if their light curves have similar shapes and same periods within a given error. Two Cepheids in this case are considered to have the same period if the difference between their $\log P$ is smaller than 0.07. With the adopted PLC slope of $\alpha \approx -3$, this gives a systematic uncertainty of 0.16 mag.

[2]The use of both Π and P for the pulsation period is unfortunate (see Appendix D). P is commonly adopted when using the PLC relation and Π when discussing pulsation theory to avoid confusion with pressure.

In addition, since the selection is based on the light curve, they consider all Cepheids in the sample to pulsate in the fundamental mode, meaning all gas moves in the same direction at every point. This ensures that they obey the same PLC-relation. The correction for extinction is made using both the V and I bands, but they find no need for colour excess estimation, since the sosie method is applied (thus, the Cepheids have similar intrinsic colour).

Next, the sample is corrected for incomplete bias. The bias arises as we observe more distant Cepheids, for which the fainter end of the PLC-distribution is progressively missed (Paturel et al., 2002a). As such, restricting the sample to Cepheids of a period larger than a given limit reduces this bias.

Finally, this gives a calibrated distance scale from Cepheids. An advantage of using the LMC is that it has numerous Cepheids located at the same distance (at 18.5 mag), which allows for accurate determination of the slope for the PLC-relation. However, Paturel et al. (2002a) note the low metallicity in the LMC sample is cause for concern as they are not sure the derived slope can be applied to all kinds of metallicity.

The second calibration is described in Saha et al. (2006). Similar to Paturel et al. (2002a), they calibrate the slope and zero point of the PLC-relation from the LMC with a similar distance of 18.54 mag. Both V and I bands are used for determining extinction and metallicity. In this calibration, the method of sosie is not used and instead the slope and zero point are determined directly from the LMC sample. The adopted relations for the absolute magnitude are:

1. LMC ($P > 10$ days)

$$M_V = -2.567 \log P - 1.634 \tag{78}$$

$$M_I = -2.822 \log P - 2.084. \tag{79}$$

2. LMC ($P < 10$ days)

$$M_V = -2.963 \log P - 1.335 \tag{80}$$

$$M_I = -3.099 \log P - 1.846. \tag{81}$$

The two different relations are due to a break in the PLC-relation for the LMC at $P = 10$ days. Additionally, we see the slopes differ from that of Paturel et al. (2002a) as they find this new PLC-relation for the LMC based on a revised photometric zero point of the HST-WFPC2 and new metallicity corrections. The Classical Cepheid variable stars are amongst the most accurate distance indicators for distances within 0.5 kpc - 10 Mpc (Jacoby et al., 1992), but can be used even farther with the most distant at 29 Mpc (Carroll & Ostlie, 2007). While the method has many strengths as outlined in this section, the largest source of error is the interstellar extinction, which, as mentioned, is typically reduced via measurements at multiple wavelengths (Carroll & Ostlie, 2007). We are limited to NGC 3351 and NGC 3368 when using Cepheid-based distances in Leo I, since classical Cepheids are Population I stars and, therefore, mostly reside in the spiral arms of star-forming galaxies.

3.1.2 The Tip of the Red Giant Branch method

Low mass, globular cluster-like stars begin their main sequence phase by burning hydrogen in a radiative core surrounded by a convective envelope. Towards the late stages of their evolution, the hydrogen levels drop in the core and the energy production shifts to a thick hydrogen-burning shell. As the core begins to contract, the temperature rises and the shell actually produces more energy than the core did in the main-sequence phase.

A schematic of the evolution of the low-mass star is shown in Figure 17. The described core contraction is indicated on the figure, where the star leaves the zero-age main sequence (ZAMS). As the shell consumes the available hydrogen, the mass of the helium core increases and becomes nearly isothermal. This process continues until the Schönberg-Chandrasekhar limit is reached (Carroll & Ostlie, 2007). The limit describes the maximum mass of a non-fusing isothermal core for which it can still support the surrounding envelope. As a result, the core begins to contract rapidly and the gravitational energy released

in this process causes the envelope of the star to expand. The effective temperature thus drops, and the star starts to evolve along a redward path on the H-R diagram known as the subgiant branch (SGB).

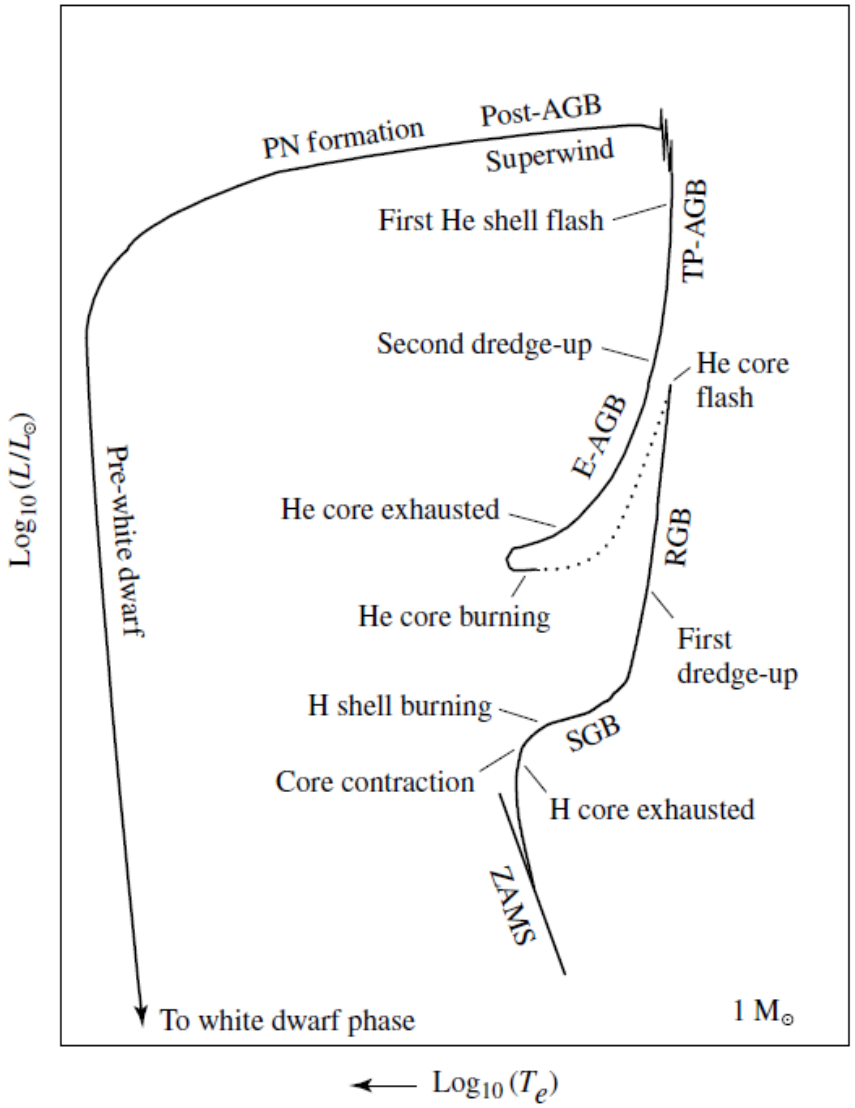

Figure 17: Figure 13.4 from Carroll & Ostlie (2007). A schematic diagram of the evolution of the low-mass star of 1 $M_\odot$ from the zero-age main sequence formation to the formation of a white dwarf star. The dotted phase of evolution represents rapid evolution following the helium core flash. The various phases of evolution are labelled as follows: Zero-Age-Main-Sequence (ZAMS), Sub-Giant Branch (SGB), Red Giant Branch (RGB), Early Asymptotic Giant Branch (E-AGB), Thermal Pulse Asymptotic Giant Branch (TP-AGB), Post- Asymptotic Giant Branch (Post-AGB), Planetary Nebula formation (PN formation), and Pre-white dwarf phase leading to white dwarf phase.

As the star expands and the effective temperature drops, the photospheric opacity increases due to a contribution of the H^- ion. The result of this is a convection zone at the surface which begins to extend deeper into the star's interior until it approaches the

Hayashi line of fully convective objects and now moves upwards in the H-R diagram at the *Red Giant Branch* (RGB). The helium core continues to collapse as we move along the RGB and keeps growing in mass from the ashes of the burning hydrogen, leading to a rise in density and rendering the core strongly electron-degenerate. Once the temperature and density reach approximately 10^8K and 10^7 kg m^{-3}, respectively, the triple-alpha process is initiated (Carroll & Ostlie, 2007).

The ignition of helium burning starts in a shell around the centre, but shortly after, the core is ignited resulting in what is known as *The Helium Core Flash* which occurs at the *Tip of the Red Giant Branch* (TRGB). This violent explosion is very bright with luminosities reaching up to $10^{11} L_\odot$ (Carroll & Ostlie, 2007). The reason for this explosive energy release is related to a weak temperature dependency of electron degeneracy pressure and strong temperature dependency of the triple alpha process. Thus, the energy generated must first lift the degeneracy before helium burning can take place.

After this violent flash, the star contracts and starts to burn helium in the core along the horizontal branch. The discontinuity between the He core flash and He core burning is due to the rapid process as the energy released in the flash is short-lived with a duration of only a few seconds. Due to the degeneracy, the helium ignition happens at roughly the same mass. This means the ignition occurs at a predictable luminosity (Rizzi et al., 2007).

The observable evidence of this phenomenon is a sharp cut-off in the luminosity function of the Red Giant Branch, which is located at $M_I \sim 4$. Given this prediction, we are able to determine distances to TRGBs.

The TRGB method is a very valuable distance indicator within $\sim$ 10 Mpc (Rizzi et al., 2007). Its main advantages is that the observable is very bright, the physical process behind the method is well-understood and it can be applied to almost all galaxy types as long as they contain a significant old population. In addition, RGBs are dispersed, such that reddening in the host galaxy does not play a significant role and observations are typically made in the near IR as well. Although foreground contamination is still a problem and the bolometric magnitude of the tip is known to depend strongly on the metallicity of the stellar population.

Zero Point calibration of Tip of the Red Giant Branch Distances

The TRGB-based distances to the members of Leo I are based on the calibration provided in Rizzi et al. (2007). They aim at providing a new estimate of the TRGB magnitude dependency of the stellar population (i.e. the metallicity), a new zero point of the TRGB versus colour relation and a new calibration in the Hubble Space Telescope (HST) flight system. They provide a robust calibration for which accurate, methodologically coherent distances could be obtained for all $\sim$ 500 galaxies in their sample within 10 Mpc. They arrive at the calibration for the absolute magnitude:

$$M_I = -4.05(\pm 0.02) + 0.22(\pm 0.01)[(V - I) - 1.6]. \tag{82}$$

The systematic uncertainty associated with this calibration is estimated to be 0.12 mag. In Rizzi et al. (2007), they demonstrate how it is possible to independently estimate the reddening from the same colour-magnitude diagram (CMD) that gives the TRGB as long as there is a well-formed main sequence. The calibrated zero point is found to be in agreement with the Cepheids scale. However, it does not require the assumed metallicity dependency in the PLC-relation, which raises a discussion towards the zero point of the Cepheids scale. In (Rizzi et al., 2007), they state that the Cepheids scale is none too firm as it is generally being set by the distance of the LMC alone as we explored in the previous section, whereas they establish the TRGB scale from an assumed luminosity for the Horizontal Branch and five Local Group galaxies.

3.1.3 The Surface Brightness Fluctuations method

In the previous sections, we explored Classical Cepheids and TRGBs. Their methods depend on observations, where we are able to resolve individual stars. However, the Surface Brightness Fluctuation method is instead based on the global properties of galaxies, and can thus be used to probe distances even farther. Consider, for instance, an image of an elliptical galaxy. Even if our resolution is relatively poor, the discreteness of stars (or rather the most massive stars) causes measurable bumps in the surface brightness. This is what is known as *Surface Brightness Fluctuations* (SBF).

Surface brightness fluctuations are fundamentally a simple effect and take advantage of how a detector, such as a CCD camera, works. We cannot resolve individual stars, but we can measure the mean flux per pixel in the CCD and the associated rms variation in flux between the pixels (Jacoby et al., 1992). In Figure 18, schematics of two galaxies are shown. The galaxy on the right is twice as distant as the one on the left. The grid represents the CCD's pixels superposed on the images. We cannot distinguish the galaxies based on the mean flux per pixel due to the number of stars which are projected into a single pixel of fixed angular size (Jacoby et al., 1992).

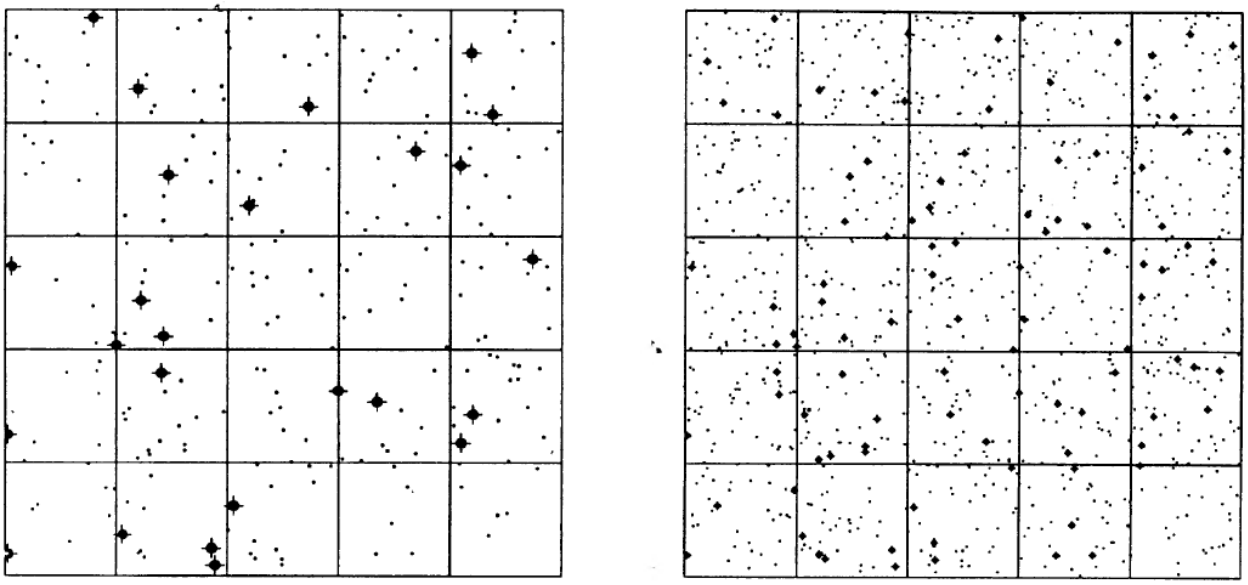

Figure 18: Figure 18 from Jacoby et al. (1992). The schematic galaxy in the right panel is twice as distant as the one in the left panel. Large dots are giant stars and small dots are main sequence stars. The grid represents the pixels of a CCD.

The mean number of stars, N, scales with distance as $N \propto d^2$, whereas the flux per star decreases as $\bar{f} \propto d^{-2}$, where $\bar{f}$ is the mean flux per star. The mean flux can be written as $N\bar{f}$, while the variance in flux can be written as $N\bar{f}^2$. With the given scaling relations, the variance scales as d^{-2} and the rms scales as d^{-1}. This provides the means to distinguish them, as the galaxy which is twice as distant, would appear twice as smooth as the nearer galaxy (Jacoby et al., 1992).

When determining distances with the SBF method, we need measurements of fluctuation flux and a conversion to distance by assuming a fluctuation luminosity. The method is applicable to relatively dust free systems, i.e. E and S0 galaxies, spiral bulges and glob-

ular clusters (Jacoby et al., 1992). Typically the I band is used for this method, since the absolute fluctuation magnitudes, $\bar{M}$, are so bright at infrared wavelengths that it overcomes the brighter sky background. Additionally, I-band measurements minimise dust absorption.

Calibration of Surface Brightness Fluctuations

A significant strength of the SBF method is that, like the previous methods, it is based on luminosities of stars for which we have a good fundamental understanding. This allows us to evaluate the luminosities of the stellar populations we observe both theoretically and empirically for systems with known distances. Previous studies of SBFs have shown that the fluctuation luminosity in the blue photometric bands depends strongly on metallicity, age and the Initial Mass Function (IMF) of the stellar population, whereas the luminosities are significantly less sensitive to the population parameters in the I-band (Jacoby et al., 1992).

The calibration adopted for SBF-based distances in Leo I are described in Jensen et al. (2003) [3]. The main goal of their work is to provide a new calibration of the absolute fluctuation magnitudes in the F160W (1.6 m) filter ($\bar{M}_{F160W}$) on the Hubble Space Telescope (HST).

Accurate SBF distance measurements rely on the empirical calibration of the absolute fluctuation amplitudes. The I-band SBF (I-SBF) distances employed are calibrated using Cepheids distances to galaxies, where both methods are applicable. The resulting distances of the I-SBFs are, therefore, subject to the same systematic uncertainty as in the Cepheid distance scale (0.16 mag). Similar distance modulus to the LMC is used, i.e. 18.50 mag. Note that all Cepheid distances used for calibration are direct measurements. The method of calibrating Cepheids is described in Section 3.1.1. Although no metallicity correction to the Cepheid distances is adopted in Jensen et al. (2003), they instead apply

[3] It is worth mentioning that the first measurements of SBF was done by Tonry and Schneider (1988), whose work and calibration of the method is carried on in Jensen et al. (2003).

a galaxy colour correction. They obtain the calibrated absolute fluctuation magnitude:

$$\bar{M}_{F160W} = (-4.86 \pm 0.03) + (5.1 \pm 0.05)[(V-I)_0 - 1.16] \quad \text{for} \quad 1.05 < (V-I)_0 < 1.24, \tag{83}$$

where $(V-I)_0$ is the optical extinction-corrected colour. Finally, from a comparison of fluctuation magnitudes and distance-independent fluctuations colours to the predictions of stellar population models, it is noted that the total systematic error in the Cepheid scale could possibly be $\lesssim 0.1$ mag.

3.1.4 Type Ia supernovae as a distance indicator

The standard model for type Ia supernovae is the destruction of a white dwarf star in a binary system (Carroll & Ostlie, 2007). As mass is being accreted onto the white dwarf from the companion star, it approaches the Chandrasekhar mass. White dwarfs resist gravitational collapse through electron degeneracy pressure. The Chandrasekhar mass of $1.4M_\odot$ is the limit at which the white dwarf becomes unstable. When the white dwarf exceeds this limit, we are able to observe the resulting tremendous explosion.

Supernovae, as extremely luminous objects, are particularly useful when determining extragalactic distances. For supernovae, we typically make use of the peak luminosity, rate of decline and presence of rapid fluctuations. For type Ia supernovae, these vary relatively little in a systematic way, because of the explosion mechanism, which means they can be used as *standard candles*. They are very consistent in their energy output. Most type Ia supernovae reach an average maximum magnitude in the blue and visual bands of (Carroll & Ostlie, 2007):

$$\langle M_B \rangle \simeq \langle M_V \rangle \simeq -19.3 \pm 0.03. \tag{84}$$

Specifically for type Ia supernovae, there exists a clear relationship between the peak luminosity and the rate of decline in the light curve; the brightest decline the slowest. This makes it possible to accurately determine the maximum luminosity of individual supernovae by simply measuring the rate of decline, thereby yielding the absolute magnitude

from which we can determine the distance.

Type Ia supernovae do not exhibit hydrogen and helium lines. Instead, they have a strong presence of Si II lines along with neutral and ionised lines of I, Mg, S, Ca and Fe (Carroll & Ostlie, 2007). Given that hydrogen is the most abundant element in the Universe and type Ia supernovae lack hydrogen, this implies that they are evolved objects that have either lost their hydrogen or converted it to heavier elements.

Type Ia supernova in Leo I

One type Ia supernova called SN1998bu was found in the Leo I group. It was observed in NGC 3368 and peaked in May 1998. An analysis of the Leo I group would not be complete without a mention of SN1998bu. However, in the words of Hernandez et al. (2000), *the extinction of SN1998bu is unusually high with* $A_V = 1.0 \pm 0.11$.

In the work of Jha et al. (1999) and Hernandez et al. (2000), they aim at correcting the light curve of SN1998bu in order to use it for determining the Hubble constant. They calibrate the distance to SN1998bu using the well-determined Cepheid distances to NGC 3368 published at the time. As discussed in Section 3.1.1, the PLC relation used is calibrated from the LMC. Although SN1998bu is relatively close to us compared to the observed type Ia supernovae today, its high reddening makes it quite complicated to obtain an independent distance as it relies on another calibration such as Cepheids, TRGBs or SBFs. For NGC 3368, Cepheids are the only ones used to calibrate SN1998bu. This places SN1998bu in a tertiary role and unsuitable for this analysis of the Leo I group. Instead, we will include a distance estimate to NGC 3368 obtained through SN1998bu for comparison.

We make use of a distance estimate determined through a comprehensive statistical model of type Ia supernovae light curves combined with the calibration from Jha et al. (1999) and Hernandez et al. (2000), presented in Mandel et al. (2011). The adopted Bayesian framework models multiple random and uncertain effects including the intrinsic co-variance in the light curve, dust extinction, reddening and distances. From this analysis, they obtain a standard deviation of predictions over bootstrap of 0.02 mag and an average standard

deviation on the uncertainty of a prediction of 0.1 mag, which are surprisingly low considering the challenges associated with SN1998bu, especially considering an expected uncertainty of 0.46 mag on the distance modulus, when it is computed from the redshift.

In order to reliably determine an independent distance to SN1998bu, one would have to accurately account for the reddening of SN1998bu. In Mandel et al. (2011), they use two different reddening laws. One for interstellar dust found in the Milky Way and one for circumstellar dust. They note that for highly dusty environments, the model tends to go towards total extinction, which they suggest should be accounted for in an extension of the model.

3.2 Recession velocities and mass of the galaxy groups

We examine the recession velocities of the members in the system. For a large gravitationally bound structure like the Leo I group, we can obtain an estimate of the mass through the virial theorem, which may be expressed in terms of the velocity dispersion, σ_r, and the radius of the system, R. Additionally, we determine a mass-to-light ratio of the Leo I group. This provides useful insight into the stability of the group as we expect a system in virial equilibrium to be relaxed.

We write the common expression of the virial theorem in terms of the time-averaged kinetic and potential energies:

$$-2\langle K\rangle = \langle U\rangle. \tag{85}$$

From this relation, it can be shown that the virial mass in terms of the velocity dispersion and radius of the system are related by:

$$M_{\text{virial}} \propto \frac{R\sigma_r^2}{G}. \tag{86}$$

We use a discrete model of the virial mass. In practice, we observe the projected separations R_i and radial velocities $\sigma_{z,i}$ for N particles. We assume spherical symmetry, i.e. $R = N^{-1}r_i$. We can write the viral theorem estimator of the mass as derived in Bahcall &

Tremaine (1981):

$$M_{\rm VT} = \frac{3\pi}{2G}\left(\sum_{i=1}^{N}\sigma_{z,i}^2\right) / \left(\sum_{i=1}^{N}\frac{1}{R_i}\right). \tag{87}$$

The z-axis is set to coincide with the line of sight. Bahcall & Tremaine (1981) address a number of problems with the estimator, with the most concerning ones being the inefficiency and inconsistency found for low number of N and bias related to the estimated mass from a finite N. We, therefore, adopt an additional method as an alternative to the virial theorem, called the *projected mass estimator*, where the projected mass q is expressed as

$$q = \frac{\sigma_r^2 R}{G}. \tag{88}$$

In order to obtain an estimator for the mass, a multiplicative factor must be determined. This factor depends on the distribution of orbits and hence their eccentricities. We consider two different models, one with isotropic orbits and one with radial orbits. From Bahcall & Tremaine (1981), we write the mass for the isotropic model, $M_{\rm I}$, and radial model, $M_{\rm R}$:

$$M_{\rm I} = \frac{16}{\pi G N}\sum_{i=1}^{N}\sigma_{z,i}^2 R_i \tag{89}$$

$$M_{\rm R} = \frac{32}{\pi G N}\sum_{i=1}^{N}\sigma_{z,i}^2 R_i. \tag{90}$$

In the absence of any specific information on the distribution of eccentricities, the recommended estimator is

$$M_0 = \frac{1}{2}(M_{\rm I} + M_{\rm R}). \tag{91}$$

Let f be the constant of proportionality. From N-experiments, it is shown by Heisler et al. (1985) that f is equal to $64/\pi$ for radial orbits and $32/\pi$ for isotropic orbits. Although they recommend that if such information about the orbits are not given, then one should

adopt a value of $32/\pi$ as this is in good agreement with numerical experiments. Thus,

$$M_{\rm I} = \frac{32}{\pi GN} \sum_{i=1}^{N} \sigma_{z,i}^2 R_i \tag{92}$$

$$M_{\rm R} = \frac{64}{\pi GN} \sum_{i=1}^{N} \sigma_{z,i}^2 R_i, \tag{93}$$

which, as noted in Heisler et al. (1985), differs by a factor of 2 from Bahcall & Tremaine (1981). We make no assumption concerning the orbits as the eccentricities are unknown. We will, therefore, compute the mass from the virial theorem ($M_{\rm VT}$), the combined model from Bahcall & Tremaine (1981) (M_0) and for each of the orbital models from Heisler et al. (1985) ($M_{\rm I}$ and $M_{\rm R}$). Given the discrepancy between the models, we deem it reasonable to test $M_{\rm R}$ from eq.(93) as this would provide the upper limit of the mass. We compute M/L from each model, although in general the mass is not easily constrained and we expect large uncertainty given low value of N.

3.3 The Data

In this section, we present the distance measurements and data reduction used for the structural analysis of Leo I, and the redshift measurements used to obtain the dynamical mass of the system.

3.3.1 Distance measurements and data reduction

In Figure 19, we show a collection of all published distance estimates in The NASA/IPAC Extragalactic Database (NED)[4]. NED contains a total of 271 distance measurements[5] for the members of Leo I based on 16 different distance indicators as shown in the legend on Figure 19. Descriptions for these abbreviations may be found in Table 21 in Appendix K. The measurements presented in the figure, however, are not all independent or suitable for the task at hand. We must, therefore, establish a set of criteria from which we can reduce the data.

[4]The NASA/IPAC Extragalactic Database (NED) is operated by the Jet Propulsion Laboratory, California Institute of Technology, under contract with the National Aeronautics and Space Administration.

[5]Note that all measurements with no stated errors are already discarded and not included in this total

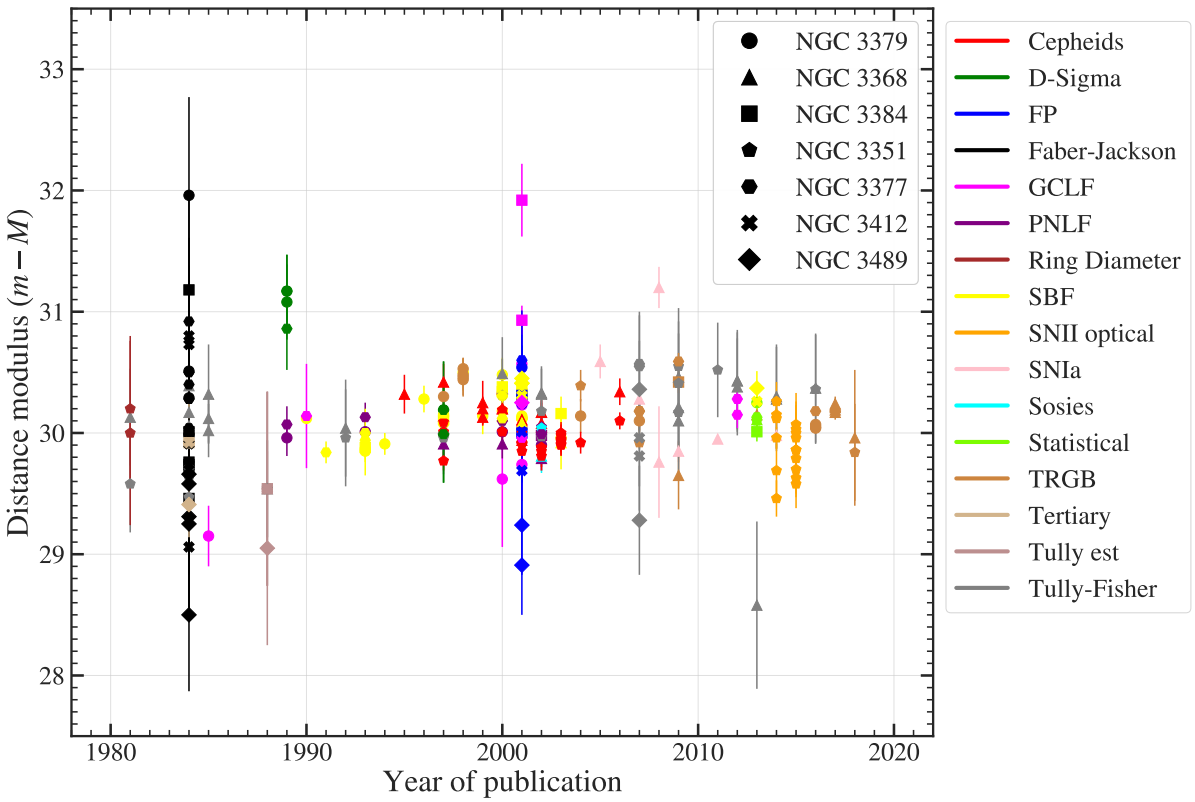

Figure 19: Distance modulus for the 7 members of the Leo I group collected from the NASA/IPAC Extragalactic Database. The applied distance indicator is indicated by colour as shown in the legend. Description of the abbreviations may be found in Table 21 in Appendix K. The marker indicates the distance modulus to a specific member as indicated in the smaller legend.

To cast some light on the issues at hand, we shall use NGC 3379 as an example. The galaxy has 58 recorded distances in NED. The main criterion for the analysis is that we need as precise measurements as possible. In the case of NGC 3379, TRGBs and SBFs are the most common, precise and latest measurements. With the adopted methods, this reduces the number of measurements drastically.

For the remaining measurements, we must now consider time-dependent trends. For example, NGC 3379 has been studied since the 1980's. We find two clear trends with time (Kumar, 2020). One is the uncertainties which drop and the other is a systematic shift towards slightly lower values. This is the case for all three methods across all the members. Possible causes for this are the use of different observatories and calibrations of the different methods, which also improve with time as newer data and statistical methods become available. This naturally leads us to be cautious with the older measurements.

Our approach to this particular issue has been to choose the most recently updated and

most precise calibration for each distance indicator, and compare measurements which adopt this calibration (see previous section). In addition, we consider the observational limitations. Given the visible and near-infrared/infrared bands used in the adopted methods, the HST provides the most precise and reliable measurements of Leo I. The HST has also been serviced multiple times since its launch, but the calibrations have been made for specific equipment on board, which apply for all the measurements compared. The instruments used are (Garner, 2017):

- **Advanced Camera for Surveys (ACS)**: A camera optimised to perform surveys or broad imaging campaigns.
- **Wide Field and Planetary Camera 2 (WFPC2)**: The main imager on the telescope. The camera records in visible and ultraviolet wavelengths. This has since been replaced with the Wide Field Camera 3 (WFC3).
- **Near Infrared Camera and Multi-Object Spectrometer (NICMOS)**: Imaging and spectroscopy at near-infrared wavelengths.

For the type Ia measurement, observations were made by Peters Automated IR Imaging Telescope (PAIRITEL), which was previously the 2MASS North telescope that completed an all-sky near-infrared survey (Mandel et al., 2011). This is very unfortunate as it raises concerns about the reliability of the measurements and a method that is already tertiary and riddled with caveats. As stated in Mandel et al. (2011), the improved precision and accuracy of the inferences about cosmic expansion may justify the effort in obtaining the data with the HST or the James Webb Space Telescope.

The final step in the reduction approach is to filter out measurements, which are not independent as some measurements may be quoted multiple times in NED. The resulting sample from this reduction approach is quite sparse with 1-6 measurements per distance indicators for each galaxy. The final reduced sample can be found in Tables 15, 16 and 17 in Appendix E. The data is also plotted in Figures 41, 42 and 43 in the same appendix.

Table 4: **Reduced sample**: $m - M$ shows the distance modulus for each measurement in the final sample. σ_{m-M} is the random uncertainty in the distance modulus. The systematic uncertainty is 0.12 mag for all measurements. **Column 3** shows the distance in Mpc with associated random uncertainty in **Column 4**. **Columns 5** and **6** show the galaxy and publication year, respectively, for each measurement. The source for each measurements are stated in **Column 7**. This table is truncated and only shows the highlighted measurements used for the analysis. For the full tables see Tables 15, 16 and 17 in Appendix E.

$m - M$	σ_{m-M}	D [Mpc]	σ_D [Mpc]	Galaxy	Year	Source
Cepheids Sample						
29.88	0.08	9.5	0.35	NGC3351	2002	Paturel et al. (2002a)
30.10	0.07	10.5	0.34	NGC3351	2006	Saha et al. (2006)
30.17	0.10	10.8	0.50	NGC3368	2002	Paturel et al. (2002a)
30.34	0.11	11.7	0.59	NGC3368	2006	Saha et al. (2006)
Tip of the Red Giant Branch Sample						
29.920	0.050	9.6	0.22	NGC3351	2007	Rizzi et al. (2007)
30.150	0.030	10.70	0.15	NGC3368	2013	Lee & Jang (2013)
30.180	0.020	10.9	0.1	NGC3377	2016	Lee & Jang (2016)
30.050	0.020	10.200	0.094	NGC3379	2016	Lee & Jang (2016)
30.420	0.100	12.10	0.56	NGC3384	2009	Mould & Sakai (2009)
Surface Brightness Fluctuations Sample						
30.02	0.22	10.09	1.02	NGC3368	2003	Jensen et al. (2003)
30.21	0.09	11.00	0.46	NGC3377	2001	Tonry et al. (2001)
30.06	0.11	10.28	0.52	NGC3379	2003	Jensen et al. (2003)
30.26	0.14	11.27	0.73	NGC3384	2003	Jensen et al. (2003)
30.28	0.14	11.38	0.73	NGC3412	2001	Tonry et al. (2001)
30.39	0.15	11.98	0.83	NGC3489	2001	Tonry et al. (2001)
SN1998bu Sample						
29-95	0.02	9.772	0.09	NGC 3368	2011	Mandel et al. (2011)

The figures show that some of the data is slightly inconsistent even though they apply the same calibration, extinction etc. Including all measurements would yield an ambiguous

result. The highlighted solid curve indicates the measurement used for the structural analysis, as this is the most precise and provides the clearest interpretation of the system structure. These values are presented in Table 4. Note that Table 4 is truncated and only shows the values used for the analysis. The full sample is shown in Tables 15, 16 and 17.

The catalogue of SBF measurements presented in Tonry et al. (2001) and Jensen et al. (2003) has been corrected for bias in Blakeslee et al. (2010). The measurements in Table 4 show the corrected values. The correction is described in Appendix E.

3.3.2 Recession velocities

We obtain recession velocities of the members in the group from the spectroscopic data presented by Hudson et al. (2001). The aim of the paper is to determine the central velocity dispersion, recession velocity and magnesium line-strength as a contribution to the Streaming Motions of Abell Clusters (SMAC) project for Fundamental Plane data for peculiar velocity studies.

The data were collected during three observing runs at the 3.9-m Anglo-Australian Telescope (AAT) and three at the 2.5-m Issac Newton Telescope (INT) (Hudson et al., 2001). Single-slit spectrographs are used for all runs with the aim of obtaining spectra with a signal-to-noise ratio of 20 per Å. This criterion was set to obtain a precision of 10 percent or better in the velocity dispersion.

Recession velocities (heliocentric), cz, were measured by comparing galaxy spectra to stellar templates using the Fourier quotient method. The uncertainty on the recession velocity is determined from bootstrapping with typical errors within $\sim$ 10kms^{-1}. The recession velocities and the associated uncertainty, σ_{cz}, for each member are shown in Table 5.

Table 5: Recession velocities (heliocentric) of members in the Leo I group.

Galaxy	cz [km/s]	σ_{cz} [km/s]
NGC 3379	911	3
NGC 3368	897	4
NGC 3384	698	3
NGC 3351	777	1
NGC 3377	695	3
NGC 3412	841	2
NGC 3489	677	2

3.4 Results

3.4.1 Structure of the group

In Figure 20, we plot the measurements from Table 4. The colours reference the different members and the line styles indicate unique sources within each method. Note that the y-scales are not equal as the shape of the distributions vary across the different methods. For reference, the distance estimate to SN1998bu is included in Figure 20 in the lower right panel.

The SBF measurements do not show a clear separation between the galaxies and could indicate that the members are consistent with the group centre. However, if we consider the Cepheids and TRGBs, it seems that a pattern appears. The solid curves in the Cepheids panel of Figure 20 indicate measurements from Paturel et al. (2002a) and the dashed from Saha et al. (2006). We treat these as two different comparisons. Nonetheless, both seem to show a trend which positions NGC 3368 in the background relative to NGC 3351. The TRGB measurements appear to show the same trend with NGC 3368 positioned along with NGC 3377 in the background.

The Cepheid and SBF measurements are considerably more uncertain compared to the TRGBs. Even though SBFs are measured and can be useful at this distance, it is an advantage that we are able to resolve individual stars, and hence, it is expected that the Cepheid and TRGB method would perform better.

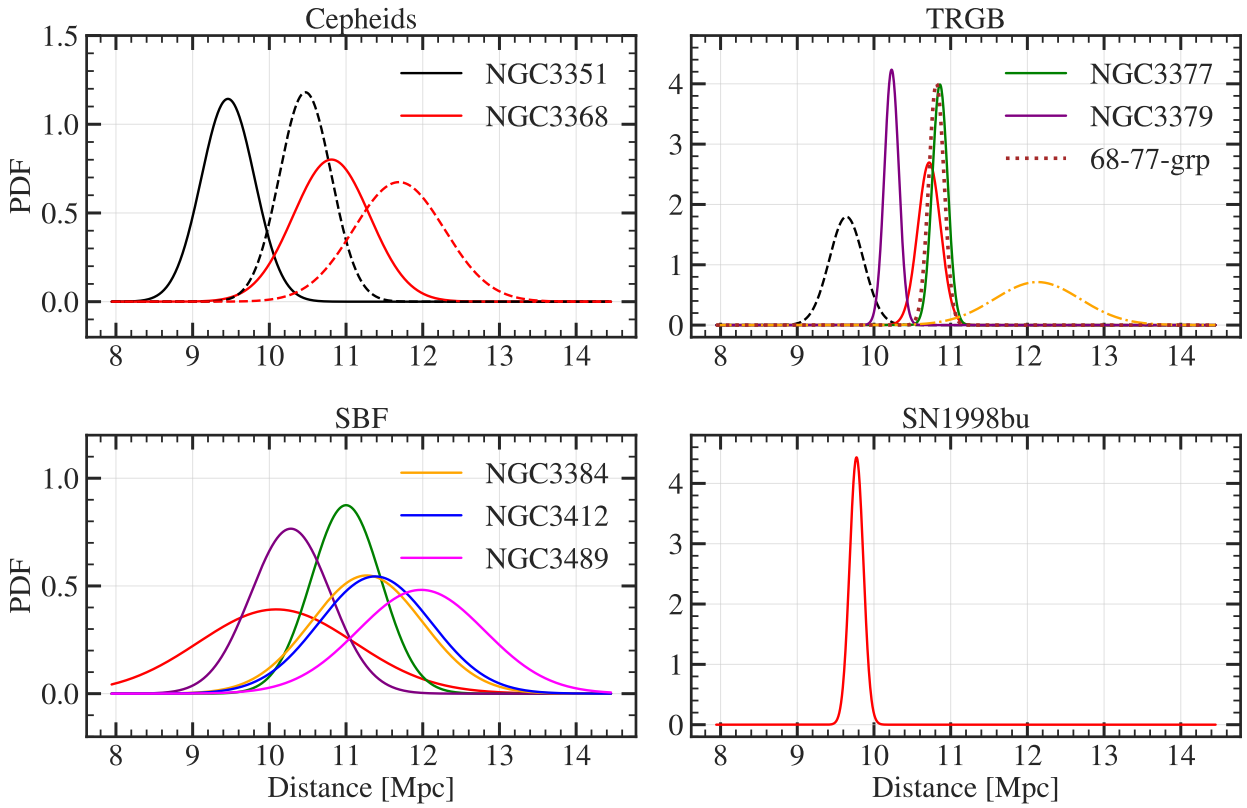

Figure 20: **Relative distance comparison.** The measurements from Table 4 are plotted as Gaussian distributions for each distance indicator with the distance in Mpc. Note that the y-scale differs for each plot. Colour coding indicates the galaxy as shown in the legends. Line styles indicate different sources within each method as referenced in Column 7 in Table 4. 68-77-grp refers to a weighted measurement based on the value for NGC 3368 and NGC 3377.

Given the broad usage of Cepheids at this scale, it is surprising to see such a big difference in the uncertainty compared to the TRGB measurements, with uncertainties up to 3 times as large for NGC 3368 and 1.6 times for NGC 3351. As we discussed in the calibration of the Cepheids, it may have a dependency on the metallicity, which deviates from the LMC, and the calibration might, therefore, not be applicable everywhere. This is a cause for concern, but the higher precision in the TRGB measurements is probably due to the more recent observations. In addition, the TRGB calibration appears to perform better. Comparing the systematic uncertainty related to the calibration, we find it is 0.16 mag for the Cepheids and 0.12 for the TRGBs. Jang & Lee (2017) provides an even better measurement with a random uncertainty of 0.054 and a systematic uncertainty of 0.057. This will be used later, but is not suitable for this analysis given an updated calibration method, which has only been applied for NGC 3368.

From the TRGB panel, we observe two sub-groups. One with NGC 3368 and NGC 3377, and another with NGC 3379 and NGC 3351. Given the high level of agreement between the Lee & Jang (2013) and Lee & Jang (2016) measurements, we have computed a weighted measurement which is shown in Figure 20 (referenced as *68-77-grp*). Additionally, NGC 3384 would appear to be positioned in close proximity to NGC 3368 and NGC 3377, but this is less clear given its high uncertainty (see Figure 42 in Appendix E).

To quantify these observations, we compute the differences between each of the measurements for all methods and the associated uncertainty through error propagation. This allows us to validate the significance of the separation. The results from this procedure are shown in Figures 21, 22, 23 and 24, along with the sigma level of the difference relative to the uncertainty.

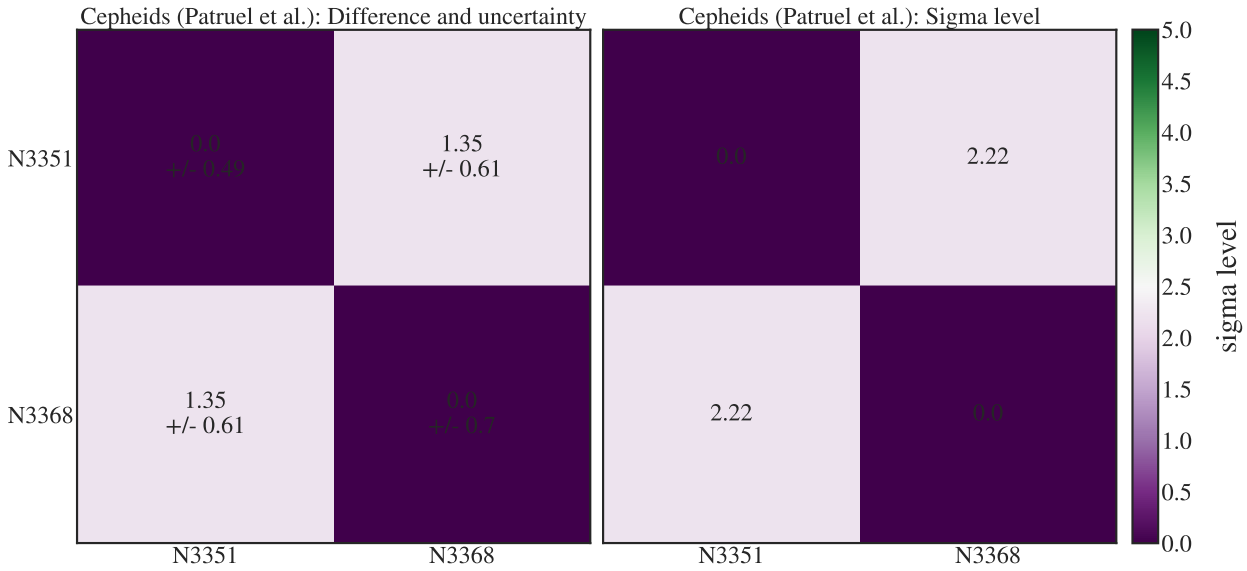

Figure 21: Cepheids. **Left panel**: Difference and uncertainty between the Paturel et al. (2002a) measurements in Mpc. **Right panel**: The sigma level of the difference relative to the uncertainty. The colour bar indicates the sigma level. Galaxy acronyms (NGC) are abbreviated as N.

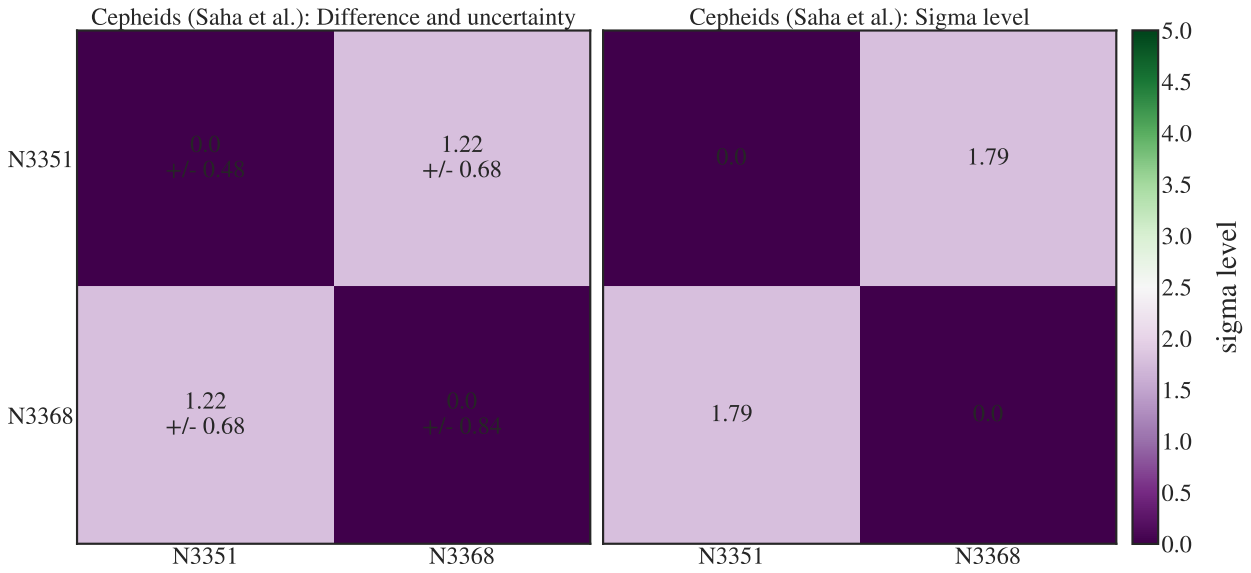

Figure 22: Cepheids. **Left panel**: Difference and uncertainty between the Saha et al. (2006) measurements in Mpc. **Right panel**: The sigma level of the difference relative to the uncertainty. The colour bar indicates the sigma level. Galaxy acronyms (NGC) are abbreviated as N.

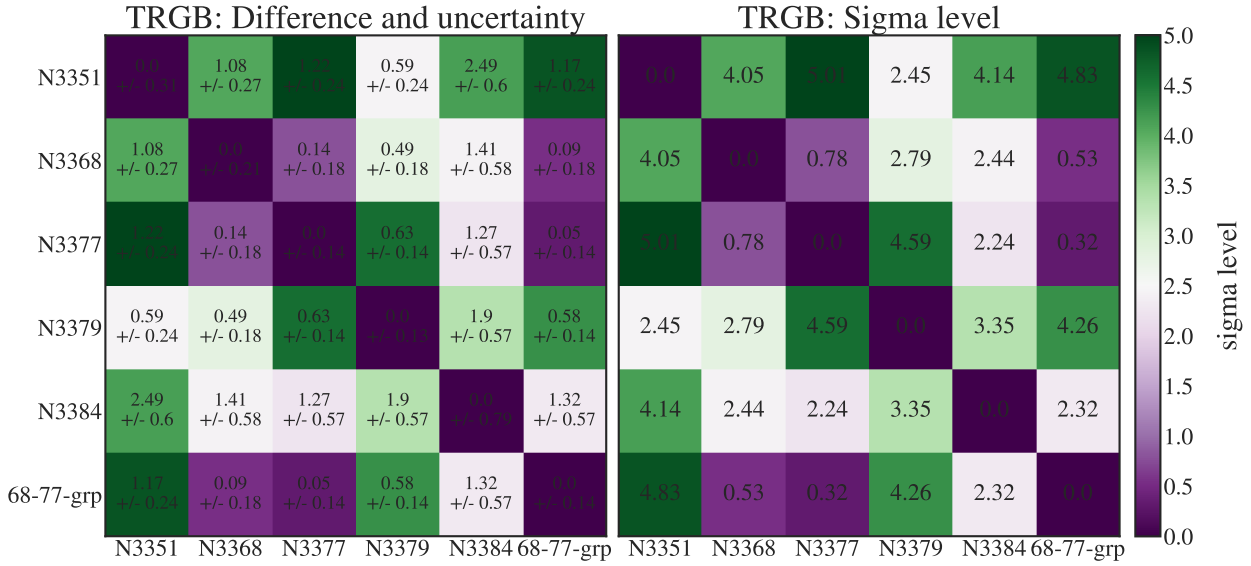

Figure 23: TRGB. **Left panel**: Difference and uncertainty between the TRGB measurements in Mpc. **Right panel**: The sigma level of the difference relative to the uncertainty. The colour bar indicates the sigma level. Galaxy acronyms (NGC) are abbreviated as N.

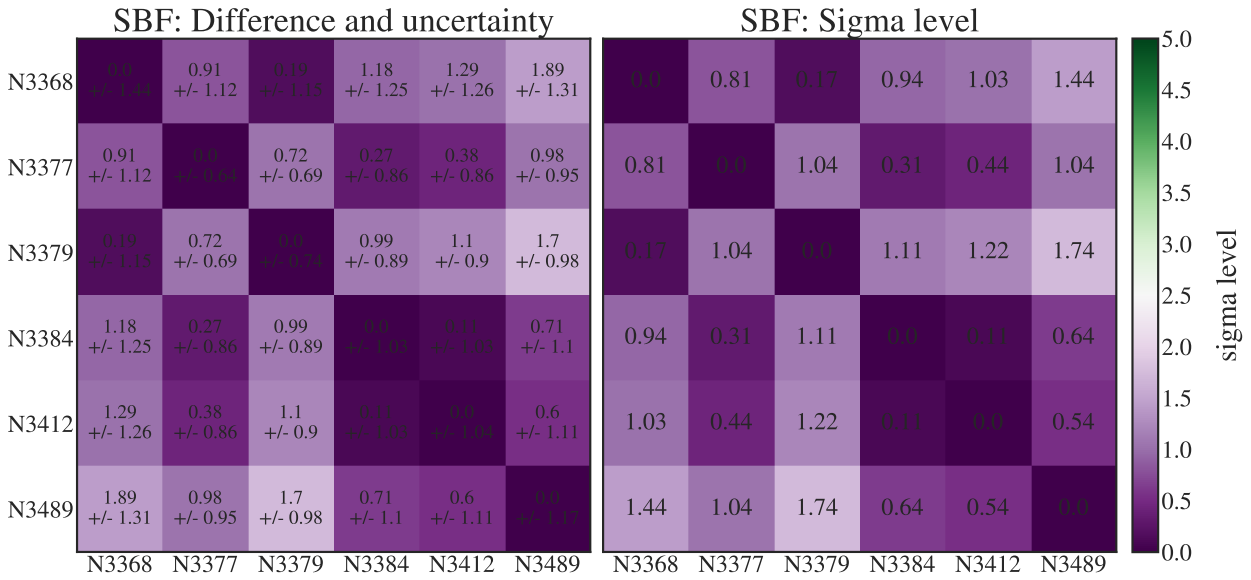

Figure 24: SBF. **Left panel**: Difference and uncertainty between the SBF measurements in Mpc. **Right panel**: The sigma level of the difference relative to the uncertainty. The colour bar indicates the sigma level. Galaxy acronyms (NGC) are abbreviated as N.

We consider differences between measurements to be very likely if they are above 2.5σ corresponding to a confidence interval of 98.75%, and define them to be statistically significant if they are above 3σ corresponding to a confidence interval of 99.73%.

If we consider the SBF measurements, we do not find any significant patterns as shown in Figure 24, with all differences falling below a sigma level of 2. We test if this is independent of the bias correction from Blakeslee et al. (2010). This is shown in Figures 44 and 45 in Appendix F. It is reassuring that in either case we find that the SBF measurements are not precise enough to show any significant patterns and thus, are not related to the correction. Nevertheless, it is worth mentioning that the difference between NGC 3379 and NGC 3377 corresponds to 2.06 sigma (96% confidence interval), which is consistent with the patterns observed in the TRGB measurements.

Similarly, due to large uncertainties, we do not find any significant difference between the Cepheids measurements, but the comparison of Paturel et al. (2002a) is consistent with a likely difference between NGC 3351 and NGC 3368.

If we instead consider the TRGB measurements, it is clear that many of the measured differences are significant with sigma levels well above 3. Let us now revisit the proposed hypothesis of the two sub-groups. The separation between NGC 3368 and NGC 3377 is

equal to 0.78 sigma, indicating a separation not different from 0. Likewise, the separation between NGC 3351 and NGC 3379 is equal to 2.45 sigma. The uncertainty in the measurement of NGC 3351 is 2.5 times that of NGC 3379. The lower sigma level is, therefore, caused by this, with NGC 3351 contributing 86% to the uncertainty in the difference. This falls into a grey-area as it just falls short of the 2.5 sigma limit. However, NGC 3351 and NGC 3368 are both late-type galaxies, while NGC 3377 and NGC 3379 are early-type galaxies. Hence, the comparison between the early-type and late-type galaxies are considered to be most important, as we can expect subtle systematic effects when comparing the different galaxy types.

NGC 3351 and NGC 3368 are separated by $\sim 4\sigma$, while the separation between NGC 3379 and NGC 3377 is $\sim 4.6\sigma$. In addition, we find the separation between NGC 3368 and NGC 3379 to be 2.79σ. We, therefore, conclude that there is a clear pattern in the group. NGC 3368 and NGC 3377 are situated by itself and we thus adopt the proposed 68-77-grp. NGC 3379 falls between NGC 3351 and 68-77-grp, but with indications of closer proximity to NGC 3351.

Given the considerations of different galaxy types and a significance level of 2.45σ, there is not enough information to reject a possible subgroup consisting of NGC 3351 and NGC 3379. Similarly, the proposed sub-groups could include more members of the group, but this would require a comparably high precision to quantify.

We can further investigate this observed structure of Leo I by comparing the depth and width of the group. In Figure 25, we illustrate the field view of Leo I. If we assume the system shape is well-represented by a sphere, we can overlay the projected 2D size as circles. The 2D centre coordinates of the system are determined from the geometric extent of the group. The larger grey circle is the estimated size of Leo I. The smaller red circle shows the size when excluding NGC 3489 given its large projected separation. We will, therefore, consider both cases, since the measured distances to NGC 3489 do not provide sufficient precision to discard it.

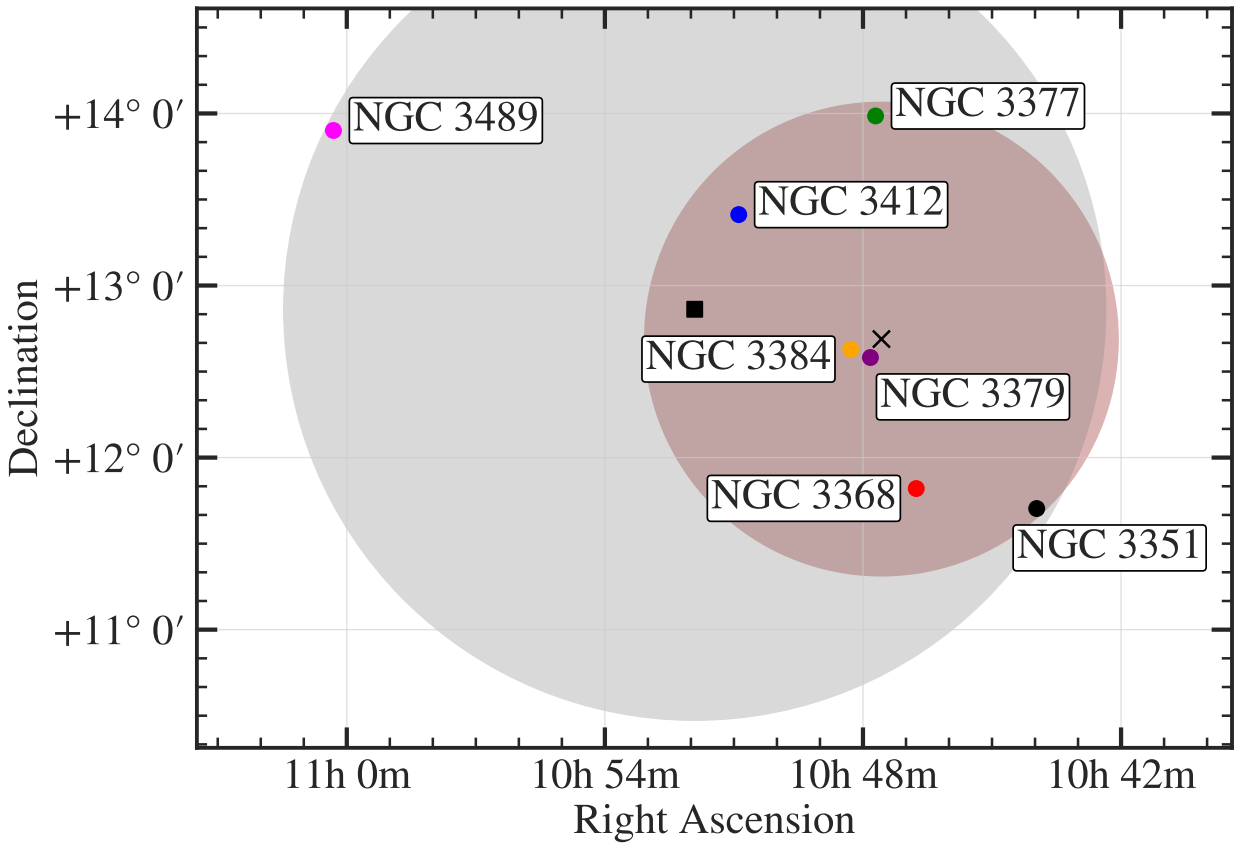

Figure 25: Field illustration of Leo I. The grey circle shows the estimated projected 2D size of the group when including all members (the black square marks the centre). The red circle shows the projected size when excluding NGC 3489 (the black cross marks the centre).

We would expect the difference between the width and depth to be consistent with zero. From the obtained structure of the group, we shall consider 3 different depths of the group. One is the observed maximum separation, which is between NGC 3351 and 68-77-grp. The other is relative to NGC 3379, resulting in NGC 3351 versus NGC 3379 and NGC 3379 versus 68-77-grp. The projected radii are $R_{\text{small}} = 5.50'$ and $R_{\text{large}} = 9.55'$.

In order to obtain the width in Mpc we must assume a distance to the group. However, the apparent structure of Leo I does not indicate a clear group centre. Instead, we compute a weighted distance between the compared members (denoted $\bar{LC}$) from which we obtain the width in Mpc by $W = \tan(2R) \cdot \bar{LC}$. The depth, DP, is obtained from the measured differences in Figures 21 and 23. The difference between the width and depth is denoted $|DP - W|$. The associated uncertainty is obtained through error propagation and is based on the uncertainties in the distance measurements, as we assume no error on the radius. The results are summarised in Table 6.

Table 6: **Depth and width of Leo I**: The top and bottom tables show the results excluding and including NGC 3489, respectively. Column 1 shows the two members/groups from which the depth is computed. All values are based on the TRGB measurements except for the last row where we use the Paturel et al. (2002a) Cepheids. $\bar{LC}$ and $\sigma_{\bar{LC}}$ are the weighted distance and uncertainty, respectively, between the members relative to us. Similarly, W and σ_W correspond to the computed width, while DP and σ_{DP} refer to the computed depth/separation between the members/groups. $|DP - W|$ shows the difference between the width and depth with associated sigma level relative to the uncertainty stated in Column 9. All distances are stated in Mpc.

Excluding NGC 3489	$\bar{LC}$ [Mpc]	$\sigma_{\bar{LC}}$ [Mpc]	W [Mpc]	σ_W [Mpc]	DP [Mpc]	σ_{DP} [Mpc]	$\|DP - W\|$ [Mpc]	Sigma Level
NGC 3351 vs. NGC 3379	10.14	0.09	0.487	0.004	0.6	0.2	0.11	0.56
NGC 3379 vs. 68-77-grp	10.51	0.07	0.505	0.003	0.6	0.1	0.09	0.95
NGC 3351 vs. 68-77-grp	10.62	0.09	0.510	0.004	1.2	0.2	0.69	3.45
NGC 3351 vs. NGC 3368 (Cepheids)	9.9	0.3	0.48	0.01	1.3	0.6	0.82	1.37
Including NGC 3489	$\bar{LC}$ [Mpc]	$\sigma_{\bar{LC}}$ [Mpc]	W [Mpc]	σ_W [Mpc]	DP [Mpc]	σ_{DP} [Mpc]	$\|DP - W\|$ [Mpc]	Sigma Level
NGC 3351 vs. NGC 3379	10.14	0.09	0.847	0.008	0.6	0.2	0.25	1.23
NGC 3379 vs. 68-77-grp	10.51	0.07	0.878	0.006	0.6	0.1	0.28	2.78
NGC 3351 vs. 68-77-grp	10.62	0.09	0.887	0.008	1.2	0.2	0.31	1.56
NGC 3351 vs. NGC 3368 (Cepheids)	9.9	0.3	0.83	0.03	1.3	0.6	0.47	0.78

First, we consider the scenario in which we exclude NGC 3489. We find $|DP - W|$ to be consistent with 0 for both NGC 3351 versus NGC 3379, and NGC 3379 versus 68-77-grp. The significance of 3.45σ is drastically higher for NGC 3351 versus 68-77-grp (if we do not consider the Cepheid measurements). This may indicate consistency with the proposed groups as the depth is more than twice the width of the system.

Consider now the scenario where we include NGC 3489. In this case, the width is increased significantly. We find that the width is larger than the measured depths relative to NGC 3379. Possible causes could be that the depth is underestimated, which is likely based on the weak comparison between NGC 3351, NGC 3379, NGC 3368, NGC 3377 and the other members. Although we find a significant difference between NGC 3379 and 68-77-grp, we do not consider it meaningful given the 1.56 sigma level for NGC 3351 versus 68-77-grp.

From the results that include NGC 3489, the difference between the width and depth are overall not different from 0. Although it is rather contradictory that we do not find similar significance between NGC 3379 versus 68-77-grp and NGC 3351 versus 68-77-grp. The opposite is the case for the results including NGC 3489, where the width and depth appear to be significantly different.

Given the 2D projection observed in Figure 25, these results are surprising. NGC 3489 is situated quite remotely compared to the other members, but its inclusion in the estimation of the size indicates agreement with the overall maximum computed depth. Given that the other members appear to be in very close proximity (all within the red circle on Figure 25), we would expect this to be a better representation of the system. This analysis may suggest that NGC 3489 is an intermediate member between the Leo I and M66 groups. This inclusion of NGC 3489 as part of Leo I could indicate that the Leo I group is gravitationally loosely bound compared to regular groups and clusters. We find it more likely that Leo I is an irregular group with no well-defined centre.

3.4.2 Virial mass estimate

In Figure 26, we plot the velocities from Table 5. We find a mean recessional velocity of $\bar{cz} = 785$ km/s and a velocity dispersion of $\sigma_r = 99$ km/s. The velocity dispersion is relatively low for such a system.

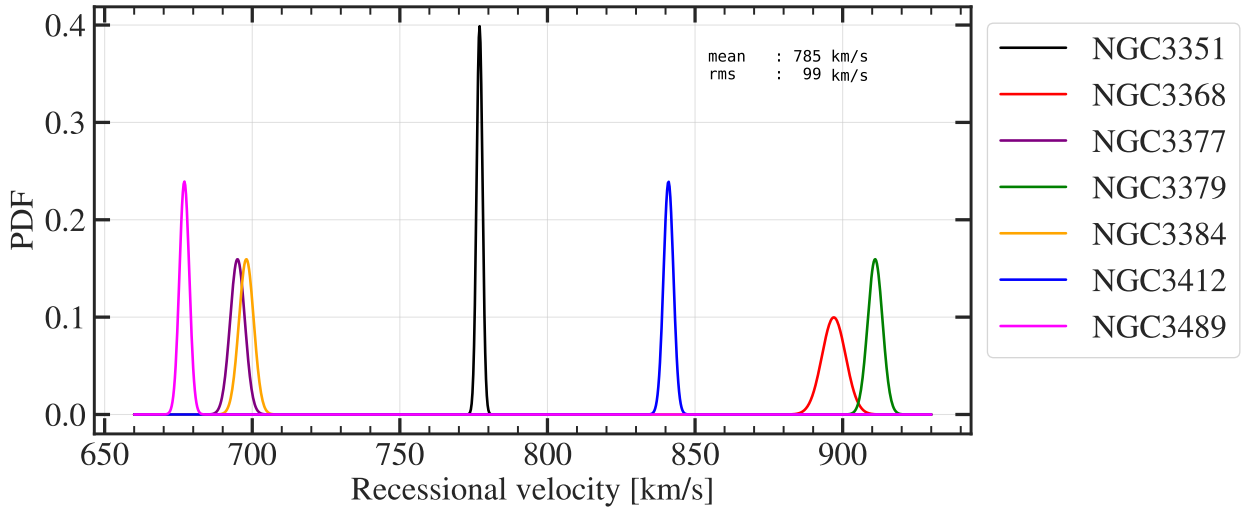

Figure 26: Recessional velocities (heliocentric) of the members in Leo I. The mean and standard deviation (rms) of the velocities are indicated in the upper right corner.

Given the irregular pattern of Leo I, as explored so far, casting doubt on the membership of NGC 3489, we would have expected its velocity to differ as well. However, adopting the criterion for membership of Leo I from Stierwalt et al. (2009), 600 km/s $< cz <$ 1200 km/s, we do not find any outliers. The low velocity dispersion is consistent with Stierwalt et al. (2009). They find a velocity dispersion for Leo I of 175 km/s. This is then reduced to 98 km/s when choosing the cutoff for membership at 1200 km/s. We find similar velocity profiles across different depths of the group as seen in Figure 26. For e.g., we find NGC 3368 and NGC 3379 to have very similar velocities, which differ from NGC 3384 and NGC 3377. Intuitively, we would have expected NGC 3384 and NGC 3377 to be closer to NGC 3368. This is not of any significance, however, given the low velocity dispersion.

We can now estimate the mass from eqs. (87), (91), (92) and (93). We consider the mass estimates in both scenarios when including and excluding NGC 3489. We find the average projected separation; $\langle R_{\text{large}} \rangle = (276 \pm 1)$ kpc and $\langle R_{\text{small}} \rangle = (153 \pm 1)$ kpc. Similarly, we find the average projected radial velocity dispersion; $\langle \sigma_{z,\text{large}} \rangle = (92 \pm 14)$ km/s and

$\langle \sigma_{z,\text{small}} \rangle = (87 \pm 13)$ km/s.

For the conversion between arc minute and Mpc, we adopt the weighted distance between NGC 3351 and 68-77-grp of (10.62 ± 0.09) Mpc. Note that the number of bodies, N, is set to 6 when excluding NGC 3489. The resulting virial mass is summarised in Table 7.

Table 7: Mass of Leo I for the virial theorem mass estimator and the projected mass estimator.

	M_{VT} $[10^{11} M_\odot]$	M_0 $[10^{11} M_\odot]$	M_I $[10^{11} M_\odot]$	M_R $[10^{11} M_\odot]$
Excluding NGC 3489	13 ± 4	40 ± 10	27 ± 8	50 ± 20
Including NGC 3489	26 ± 8	80 ± 20	60 ± 20	110 ± 30

We find that the viral mass ranges between $10^{12} M_\odot$ - $10^{13} M_\odot$ depending on the adopted model. The majority of the estimates, however, are of the order $10^{12} M_\odot$, which is considerably low as the mass of NGC 3379 alone is of order $10^{11} M_\odot$. We would expect a group of this size and the given members to be on the order of a few $\sim 10^{13} M_\odot$ (Sparke & Gallagher, 2007). This estimate is under the assumption of the Plummer sphere, which has the same multiplicative factor as the isotropic model in eq. (92).

We can qualitatively validate the predicted masses by calculating the mass-to-light ratio for the group. Luminosities for the visible band are retrieved from NED. The mass-to-light ratio in the visible band are tabulated in Table 8.

Table 8: Mass-to-light ratios of Leo I in the visible band for the predicted masses. All values are in units of $M_\odot / L_\odot$.

Excluding NGC 3489

Spectral Region	M_{VT}/L	M_0/L	M_I/L	M_R/L
Visible	15 ± 4	40 ± 10	30 ± 9	60 ± 20

Including NGC 3489

Spectral Region	M_{VT}/L	M_0/L	M_I/L	M_R/L
Visible	29 ± 9	90 ± 20	70 ± 20	120 ± 30

Amongst the 4 models, we find that the virial mass estimator provides the lowest predic-

tions independent of the chosen size of the system. Given this low estimate, we find it likely that the proposed bias and inefficiency complications related to low N render the virial mass estimator unsuitable for the group. Considering the projected mass estimator models, we find all 3 to be roughly within a factor of 2 when choosing the size of the system with the largest estimate from the radial model. However, all estimates are relatively low.

Generally, for groups in the visible band, we would expect the mass-to-light ratio to lie in the range $80 M_\odot/L_\odot \lesssim M/L_V \lesssim 300 M_\odot/L_\odot$ (Sparke & Gallagher, 2007). However, this range has been constrained further in Hradecky et al. (2000) and Girardi et al. (2002), where typical values for groups and clusters lie in the range $140 M_\odot/L_\odot \lesssim M/L_V \lesssim 300 M_\odot/L_\odot$. Additionally, it is shown in Hradecky et al. (2000) that the mass-to-light ratio is roughly independent of the cluster/group mass.

We can, therefore, conclude, regardless of what model we choose, that all computed mass-to-light ratios are quite low compared to the expectation value. As previously mentioned, the mass is quite difficult to constrain, as seen from the large uncertainties. This is not thought of to have any effect as we repeatedly find low mass-to-light ratios across the different models.

Given the picture of the group that we have established in this analysis, we find Leo I to be an irregular group which is ill-described by spherical symmetry as assumed in the mass predictions. We find a crossing time of $\tau_{\text{cross}} = 2R_{\text{max}}/\sigma_r = 8.77 \cdot 10^9$ years, for $\sigma_r = 99$ km/s. Combining this with the structural and kinematic analysis would suggest that Leo I has not had time to become virialised.

3.5 Discussion and conclusion on the structure of the Leo I group

Amongst the 3 distance indicators, the TRGB-based measurements appear to perform the best with precision significantly higher than Cepheid- and SBF-based measurements. This is unfortunate, as it leaves an ambiguous insight into the true relationship between the members. We find significant distance between the members to conclude that the

Leo I group may be better described by dividing it into two entities. While the link between NGC 3351 and NGC 3379 might be weak due to unaccounted effects related to the different galaxy types, we find a strong connection between NGC 3368 and NGC 3377.

In Section 2, we cast doubt on the link between NGC 3368, NGC 3379 and NGC 3384, which is consistent with the picture of the group obtained in this analysis. While measurements to NGC 3384 are not precise, we find indications that it would be in the proximity of NGC 3377 and NGC 3368, which is in agreement with the origin of the HI structure in the group resulting from a collision between NGC 3384 and NGC 3368.

The distances determined to Leo I are determined by means of the cosmic distance ladder. While Leo I is situated roughly at 10-11 Mpc from us, we find the propagated uncertainties in the distances to be quite large, which further complicates this type of analysis. On top of this, the presence of only seven members in the group leaves us with a qualitative discussion of the group's structure as we are dominated by low statistics. For this analysis to provide a robust result, we would need more data that could be used compare more of the members, preferably in an independent manner across different methods.

Nonetheless, the proposed subgroups and their relationship between each other are vital for using Leo I in the next step of the cosmic distance ladder. Given no clear centre, we must consider the absolute distance to each galaxy itself with exemption of NGC 3351 and NGC 3368.

From the structural and kinematic analysis, we find Leo I to be an irregular group. The low mass-to-light ratio in the visible band would indicate that a large amount of dark matter is absent from the group. Given the usual ranges of the mass-to-light ratio, we find it more likely that this is not the case, but rather a poor match between the models and the group. Given the derived crossing time of ~ 9 Gyr, we find it most likely that Leo I is not virialised, thus invalidating the use of the proposed mass estimators.

4 Estimating the Hubble constant

We have now established the necessary information about the Leo I group to proceed onto the next step of the cosmic distance ladder. In our aim to establish an independent measurement of the Hubble constant, we must consider two things. The Hubble constant depends on both the distance and the recessional velocity relative to the CMB. As we have already encountered in Section 3, determining precise distances are complicated and the uncertainty increases each time we step out farther and farther. On the other hand, the velocity is less sensitive to the peculiar velocity at higher redshifts. This local approach of estimating the Hubble constant is thus sensitive to a trade-off between these two quantities.

In order to obtain a precise estimate of the Hubble constant, we choose to measure the distance to the Coma cluster. The cluster is roughly 100 Mpc away from us and is a massive cluster containing $\sim$ 1000 galaxies. The cluster is well-studied, and as usual for a cluster of this richness, it contains a large amount of elliptical and S0 galaxies that can be characterised through the Fundamental Plane. From Jorgensen et al. (1996), we obtain the Fundamental Plane of Coma, which is well-determined given the large number of member galaxies. Through a revised Fundamental Plane of Leo I, we compute the ratio between the Fundamental Plane of Coma and Leo I, from which we are able to estimate the distance to Coma.

Finally, we determine the peculiar velocity of the Coma cluster in order to obtain a precise velocity estimate of the group. We make use of simulations of the local volume as presented in Carrick et al. (2015) and Jasche & Lavaux (2019), where the matter distribution within $200h^{-1}$Mpc is reconstructed using redshifts from the 2M++ redshift compilation (Lavaux & Hudson, 2011).

4.1 The Hubble–Lemaître law

Already in the first decades of the twentieth century, astronomers made systematic observations of the radial velocities of galaxies through Doppler shifts (Carroll & Ostlie, 2007).

Later, Edwin Hubble confirmed the existence of cosmic expansion through his relation between the recessional velocity of a galaxy, v, and its distance, d,

$$v = H_0 d, \tag{94}$$

known as the *Hubble-Lemaître law*[6], where the constant of proportionality H_0 is the Hubble constant and describes the current expansion rate of the Universe. Usually v is in units of kms^{-1}, d in Mpc and hence H_0 in $\mathrm{kms}^{-1}\mathrm{Mpc}^{-1}$. The expansion can be described as isotropic and homogeneous. Note that the term recessional velocity refers to a galaxy's motion due to the expansion of the Universe while its peculiar velocity is due to its motion through space. The motion of galaxies as they play a part in the expansion of the Universe is referred to as the *Hubble flow*.

As we have explored in Section 3, there is an uncertainty associated with secondary distance indicators arising from different factors, such as the calibration. Historically, difficulty in determining the value of H_0 arose from having to use remote galaxies for its calibration. This resulted in diverse values of the constant. In addition, a known selection effect called *Malmquist bias* can occur when using a magnitude-limited sample of objects, in which we only consider the objects brighter than a certain apparent magnitude (Carroll & Ostlie, 2007). At large distances, this means that we only include the brightest objects in the sample, which skew the statistics. In order to incorporate the uncertainty in the constant, we define the dimensionless parameter, h,

$$h = \frac{H_0}{100} \quad \left[\mathrm{kms}^{-1}\mathrm{Mpc}^{-1}\right]. \tag{95}$$

h is defined as such, since H_0 was only known within a factor of two between 50 $\mathrm{kms}^{-1}\mathrm{Mpc}^{-1}$ and 100 $\mathrm{kms}^{-1}\mathrm{Mpc}^{-1}$ until the end of the twentieth century. Today, we see the value of H_0 converging towards the middle ground values of H_0.

From Hjorth et al. (2017), we adopt a cosmology corrected definition of eq. (94), which to

[6] Although attributed to Edwin Hubble, the expansion of the Universe was first derived from general relativity equations by Alexander Friedmann (Carroll & Ostlie, 2007).

a good approximation at low redshift, is expressed as:

$$H_0 = \frac{cz_{\text{cosmic}}}{D_z}\left(1 + \frac{1 - q_0}{2} z_{\text{cosmic}}\right), \tag{96}$$

where D_z is the luminosity distance, c is the speed of light, $z_{\text{cosmic}} = v/c$ is the cosmic redshift, and $q_0 = -0.53$ for standard cosmological parameters.

4.2 The Fundamental Plane

In order to understand elliptical galaxies as a class, we must know how to characterise them, i.e. determine how many parameters are required to accurately model them. It became clear from the work on early-type galaxies by Djorgovski & Davis (1987) that the effective radius, R_e, the central velocity dispersion, σ, and the mean effective surface brightness, $\langle I \rangle_e$, are related by a plane in the three-dimensional logarithmic space between the parameters. This is called the Fundamental Plane (FP):

$$\log R_e = \alpha \log \sigma + \beta \log \langle I \rangle_e + \gamma, \tag{97}$$

where α and β are dimensionless coefficients and γ is the zero-point. The FP is thought to originate from the formation and evolution processes of the galaxies (Jorgensen et al., 1996), but it is an empirical relation whose physical origin is yet not fully understood. We can elaborate on this by considering the virial theorem. If we assume that early-type galaxies are gravitationally bound systems that satisfy the virial theorem, we can write:

$$\langle V^2 \rangle = \frac{GM_{\text{tot}}}{\langle R \rangle}, \tag{98}$$

where M_{tot} is the total mass of the galaxy, $\langle R \rangle$ is a suitable mean radius, and $\langle V^2 \rangle$ is a mean kinetic energy per unit mass (D'Onofrio et al., 2017). Per definition, any virialised system belongs to the Virial Plane (VP), which, similar to the FP, is formed by the three-dimensional space between M_{tot}, $\langle R \rangle$ and $\langle V^2 \rangle$. However, none of these are observable

quantities. The equation is, therefore, written as:

$$M_{\rm tot} = \frac{K_V \sigma^2 R_{\rm e}}{G}, \tag{99}$$

where $R_{\rm e}$ is the effective radius (radius within which half of the galaxy's luminosity is contained) and $K_V = 1/(k_{\rm v} k_{\rm r})$ is a dimensionless quantity. K_V takes into account projection effects, density distribution and stellar orbit distribution (D'Onofrio et al., 2017). The expression for K_V is obtained through:

$$\langle V^2 \rangle = k_{\rm v} \sigma^2 \qquad \text{and} \qquad \langle R \rangle = k_{\rm r} R_{\rm e}. \tag{100}$$

We can write the mean effective surface brightness as $\langle I \rangle_{\rm e} = L/2\pi R_{\rm e}^2$. The effective radius for the VP can then be expressed as:

$$R_{\rm e} = \frac{K_V}{2\pi G} \left(\frac{M_{\rm tot}}{L} \right)^{-1} \langle I \rangle_{\rm e}^{-1} \sigma^2, \tag{101}$$

or in logarithmic form as:

$$\log R_{\rm e} = 2 \log \sigma - \log \langle I \rangle_{\rm e} + \log K_V - \log \frac{M_{\rm tot}}{L} - \log(2\pi G), \tag{102}$$

which is comparable to the FP. The zero point of eq. (102) is given by:

$$\gamma = \log K_V - \log \frac{M_{\rm tot}}{L} - \log(2\pi G). \tag{103}$$

If early-type galaxies were perfectly homologous systems (same K_V and constant M/L), the zero point would be constant and the galaxies would follow the VP ($R_{\rm e} \propto \sigma^2 \langle I \rangle_{\rm e}^{-1}$). However, the observed FP scales as $R_{\rm e} \propto \sigma^{1.2} \langle I \rangle_{\rm e}^{-0.8}$ (Carroll & Ostlie, 2007). Thus, as hinted earlier, this indicates that either one or both of these assumptions must be broken.

Determining the distance to Coma from the Fundamental Plane

From Jorgensen et al. (1996), we obtain the FP of the Coma cluster expressed as:

$$\log R_{\rm e} = 1.24 \log \sigma - 0.82 \log \langle I \rangle_{\rm e} + \gamma, \tag{104}$$

with $\gamma_{\rm Coma} = 0.182 \pm 0.009$. We shall refer to the FP-relation in eq. (104) as the *classical FP-relation*. Jorgensen et al. (1996) also provide an Mg_2 corrected relation from the Mg_2-$\log \sigma$ relation. Hereafter, we will refer to this as the *Mg_2 FP-relation*, and it is defined as:

$$\log R_{\rm e} = 1.05 \log \sigma - 0.78 \log \langle I \rangle_{\rm e} + \gamma - 0.40 \Delta {\rm Mg}_2, \tag{105}$$

where ΔMg_2 is the residual between the observed value for Mg_2 (line indices) and the fitted relation $Mg_2 = 0.196 \log \sigma - 0.155$.

We adopt the measured $R_{\rm e}$, $\langle I \rangle_{\rm e}$ and σ for the Leo I members from Hjorth & Tanvir (1997), as shown in Table 9.

Table 9: Table 1 from Hjorth & Tanvir (1997). Parameters for Leo I Group Early-Type Galaxies.

Galaxy (NGC)	m_{R_c} (mag)	R_e (arcsec)	A_B (mag)	$\log\langle I\rangle_e$ ($L_\odot$ pc^{-2})	$\tilde{\sigma}$ (km s^{-1})	$V_{\rm eff}$ (km s^{-1})	σ (km s^{-1})	$\Delta\sigma$ (km s^{-1})	Mg_2
3377	9.40	56.9	0.07	2,37	97	75	117	12	0.242
3379	8.54	55.9	0.005	2.72	194	42	197	14	0.304
3384	9.32	29.4	0.07	2.98	140	80	156	11	0.265
3412	10.13	22.4	0.06	2.88	103	57	114	12	0.188
3489	9.75	18.4	0.02	3.20	115	60	126	10	0.150

The effective measured velocity dispersion, σ, inside a circular aperture is a combination of pressure and bulk unresolved rotation. Assuming intrinsic velocity dispersion, $\tilde{\sigma}$, is isotropic, the observed velocity dispersion can be expressed as $\sigma^2 = \tilde{\sigma}^2 + qV_{\rm eff}^2$, where $V_{\rm eff}$ is the effective rotational velocity along the major axis. In this work, we adopt $q = 0.75 \pm 0.25$ from Hjorth & Tanvir (1997). In the latter study, the zero point of the FP of Leo I is obtained by fitting eq.(104) to the E and S0 galaxies with the exception of NGC 3489.

We will reproduce the result and provide a revised estimate of the zero points based on the established structure of Leo I. This will allow us to compare the zero points and the luminosity distance ratios between Leo I and Coma from two different assumptions. One in which we assume all members are at the same distance (as in Hjorth & Tanvir, 1997), and the other where we only focus on NGC 3379 and NGC 3377 at their respective distances. Given the results and proposed subgroups in Section 3, we deem it suitable to only use NGC 3379 and NGC 3377 given the low precision in the distance measurement of the other E and S0 galaxies.

R_e is measured in arc seconds, and hence, the zero point ratios correspond to an angular diameter distance ratio. Let D_L be the luminosity distance and D_A the angular diameter distance. We then obtain the luminosity distance ratio through:

$$D_L = D_A(1+z)^2 \tag{106}$$

$$\Rightarrow \frac{D_{A,\text{Coma}}}{D_{A,\text{Leo I}}} = \frac{\frac{D_{L,\text{Coma}}}{(1+z_{\text{Coma}})^2}}{\frac{D_{L,\text{Leo I}}}{(1+z_{\text{Leo I}})^2}} = \frac{D_{L,\text{Coma}}}{D_{L,\text{Leo I}}} \frac{(1+z_{\text{Leo I}})^2}{(1+z_{\text{Coma}})^2} \tag{107}$$

$$\Rightarrow \gamma_{\text{Leo I}} - \gamma_{\text{Coma}} = \log_{10}\left(\frac{D_{L,\text{Coma}}}{D_{L,\text{Leo I}}}\right) + \log_{10}\left[\frac{(1+z_{\text{Leo I}})^2}{(1+z_{\text{Coma}})^2}\right] \tag{108}$$

$$\Rightarrow \log_{10}\left(\frac{D_{L,\text{Coma}}}{D_{L,\text{Leo I}}}\right) = \gamma_{\text{Leo I}} - \gamma_{\text{Coma}} - \log_{10}\left[\frac{(1+z_{\text{Leo I}})^2}{(1+z_{\text{Coma}})^2}\right]. \tag{109}$$

Finally, the relation in eq. (104) has a significant intrinsic scatter of roughly $\sim 14\%$ (0.057 dex) (Jorgensen et al., 1996). As noted in Hjorth & Tanvir (1997), the observed formal rms scatter in γ is significantly smaller than expected from the intrinsic scatter and observational errors in Jorgensen et al. (1996). We define the total scatter as:

$$\sigma^2_{\text{total}} = \sigma^2_{\text{intrinsic}} + \sigma^2_{\text{observed}}, \tag{110}$$

where $\sigma_{\text{intrinsic}}$ is the intrinsic scatter and σ_{observed} is the observed measurement error. We

can express the intrinsic scatter as:

$$\sigma^2_{\text{intrinsic}} = \frac{1}{N-1}\sum_{i=1}^{N}(y_i - \bar{y})^2 - \frac{1}{N}\sum_{i=1}^{N}\sigma^2_{i,\text{observed}}, \tag{111}$$

where N is the number of measurements and y_i is the ith FP value for a given galaxy. We shall explore the discrepancy by sampling the observed FP values for each galaxy, and computing the statistical significance of the observed scatter and the a priori estimate from the 14% intrinsic scatter plus measurement errors.

4.3 Peculiar velocities

A galaxy's measured velocity v_{los} has two components. One is the cosmic expansion, as expressed in eq. (94), and the other is the peculiar velocity, v_{pec}, as follows:

$$v_{\text{los}} = H_0 d + v_{\text{pec}}. \tag{112}$$

Peculiar velocities arise from gravitational instability and are, therefore, linked to the surrounding distribution of matter (Lavaux & Hudson, 2011). As such, peculiar velocities provide a powerful tool for probing the underlying distribution of dark matter, and are in fact the only practical means of doing so on large scales in the low-redshift Universe (Carrick et al., 2015).

In order to determine the Hubble constant, we must compute the component due to the cosmic expansion. This is easily done when both the measured radial velocity and the peculiar velocity are known. The observed radial velocity of Coma is measured to be (6942 ± 50) km s^{-1} (Wegner et al., 1999) in the heliocentric rest-frame. In order to convert it to the CMB rest-frame, we must first correct it for the Sun's peculiar motion, estimated at (371 ± 1) km s^{-1} (Fixsen et al., 1996). This amounts to $v_{\text{Coma,CMB}} = (7211 \pm 53)$ km s^{-1} when accounting for the Sun's motion projected onto the line of sight to Coma. In order to obtain the cosmic expansion component, we now only need to account for Coma's peculiar velocity, which we will estimate from two low-redshift Universe simulations.

In order to understand the motion in the Local Group relative to the CMB, a deep all-

sky map, named 2M++, of the galaxy distribution was made (Lavaux & Hudson, 2011). This map covers almost the entire sky, reaches depths of $200h^{-1}$Mpc and contains 69160 galaxies.

Both simulations use the 2M++ map, but have different approaches of determining the positions from the redshifts in the 2M++ map. The inverse problem of determining positions from redshifts are referred to as reconstruction. We will not outline the entirety of the models here, but instead refer to the respective papers for full details.

The first model, presented in Carrick et al. (2015) (CARRICKS), makes use of an iterative procedure to obtain distances from measured redshifts, in which the density contrast field, peculiar velocities and co-moving distances are computed for each step. Computed distances are then used in subsequent iterations. This procedure treats the Local Volume as a static frame.

The second model, presented in Jasche & Lavaux (2019), is named Bayesian Origin Reconstruction from Galaxies (BORG). This model is more complex and accounts for the non-linear regime of gravitational structure formation. The simulation is based on a set of initial conditions for the Universe, which are then evolved through time. Note that these initial conditions are constrained using the 2M++ survey. Unlike the first model, this does not treat the Local Volume as a static frame, but rather as a fluid.

From both models, we obtain the co-moving distance, d_C, the line-of-sight velocity, v_{los}, the peculiar velocity and the density contrast $\Delta = \delta\rho/\rho$. For the CARRICKS model, the associated uncertainty on the peculiar velocity is estimated to be ± 150 km s^{-1}. From the 2M++ analysis, BORG yields a few thousands of sampled initial conditions (ICs). The forward model in BORG is then run using this ensemble of ICs to obtain the velocity fields. The mean and standard deviation is computed from the resulting ensemble of velocity fields.

In order to obtain the peculiar velocity of Coma, we must first locate the cluster in the simulation. This is done by locating the cluster from its galactic coordinates and sampling 1000 points in a 10 degree radius and choosing the point that maximises the density

contrast. This is done iteratively until the maximum density contrast is found.

Given the spherical structure of the cluster, its density profile can be modelled as a Gaussian distribution in the co-moving space along the line of sight. We determine the centre of the cluster by computing the Full Width Half Maximum of the density profile. Once the position of the centre is known, we can estimate $v_{\rm pec}$ by computing the deviation from zero in the peculiar velocity profile at the centre location.

4.4 Results

In this section, we present the estimated value of the Hubble constant from derived distances to the Coma cluster and correction for its peculiar velocity.

4.4.1 Distance to the Coma cluster

From Table 9, we compute the FP (both classic and Mg_2) for each of the Leo I galaxies. These values are shown in Figure 27.

The solid lines are fitted FP relations from eqs. (104) and (105). Note that NGC 3489 is excluded from the fit. We find a strong agreement between the observed FP and the relations from Jorgensen et al. (1996). For the classic FP, we find $\chi^2_\nu = 0.50$ per degree of freedom and $P(\chi^2) = 0.68$. Similarly, for the Mg_2, we find $\chi^2_\nu = 0.44$ per degree of freedom and $P(\chi^2) = 0.72$. This implies a possible overestimation of the measurement errors, which is solely determined from the uncertainty in the velocity dispersion. It is clear that the larger galaxies such as NGC 3379, NGC 3377 and NGC 3384 are quite consistent while NGC 3489 falls below the fit, although the Mg_2 FP seems to reduce the scatter. From the fits, we obtain the zero points: $\gamma_{\rm classic} = 1.16 \pm 0.02$ and $\gamma_{\rm Mg_2} = 1.46 \pm 0.02$ (consistent with Hjorth & Tanvir, 1997).

For the classic FP, we find a total scatter of $\sigma_{\rm cl,total} = 0.028$ dex (or $\sim$6% in $R_{\rm e}$), which is in agreement with Hjorth & Tanvir (1997). With $\sigma_{\rm cl,observed} = 0.048$ (or $\sim$11% in $R_{\rm e}$) and 14% (0.06 dex) estimated intrinsic scatter in the FP relation obtained from Coma, we would expect $\sigma_{\rm cl,a\ priori} = \sqrt{0.06^2 + 0.048^2} = 0.077$ ($\sim$18% in $R_{\rm e}$). Given the definition of the total

scatter from eq. (110), the total scatter is significantly smaller than expected. In addition, using eq. (111), we find the observed intrinsic scatter of the FP in Leo I to be zero (as it cannot be negative by definition). This is also the case for the Mg_2 FP.

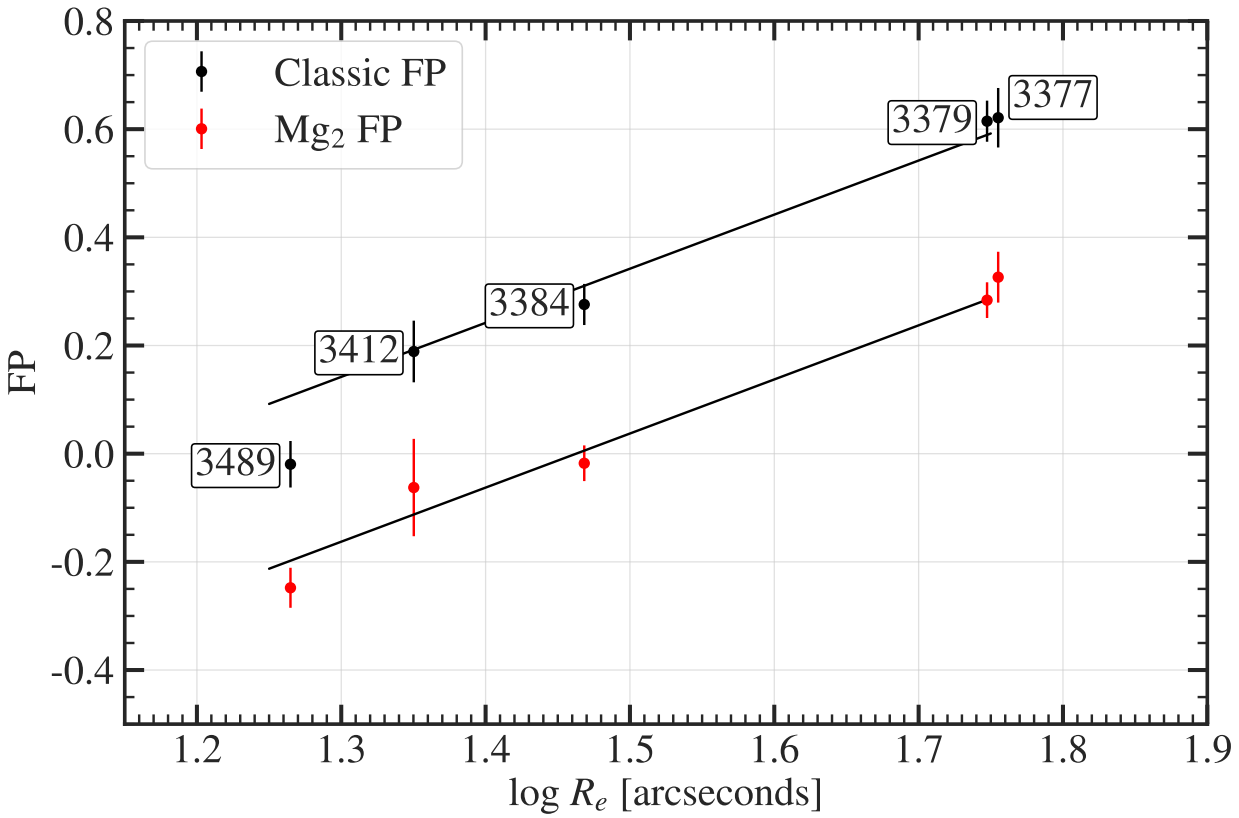

Figure 27: Fundamental plane in Leo I. The black circles are the classic FP ($FP_{\rm cl} = 1.24 \log\sigma - 0.82 \log\langle I\rangle_{\rm e}$) values for Leo I galaxies. The red circles are the Mg_2 FP ($FP_{\rm Mg_2} = 1.05 \log\sigma - 0.78 \log\langle I\rangle_{\rm e} - 0.40\Delta{\rm Mg_2}$) values for Leo I galaxies. The solid lines are fitted FP relations from eqs. (104) and (105). Note that NGC 3489 is excluded from the fit.

This is not surprising, however, when we compare the FP values in Figure 27 with the classic FP relation. All but NGC 3489 lie very close to the fit. This naturally drives the total scatter down. We test the statistical significance of the observed total scatter as described in Section 4.2. We sample a total of $n = 10^6$ trials, where each trial is a set of FP values for each galaxy (except NGC 3489) drawn from their likelihood (which is Gaussian given the errors). Note that we add 14% to the measurement errors as expected from the a priori estimate. The sampled FP value is thus drawn from a distribution with a mean of the observed FP value and a standard deviation of $\sqrt{\sigma^2_{\rm observed} + 0.06^2}$.

For each trial, we compute the total scatter. The distribution of computed total scatter

is shown in Figure 28 for both the classic and Mg_2 FP. The vertical dashed lines indicate the median, a priori and observed formal rms scatter. The shaded areas indicate the 1, 2, 3 and 4σ deviation from the median. The confidence intervals are determined from the cumulative mass function of σ_{tot} (see Figure 46 in Appendix G).

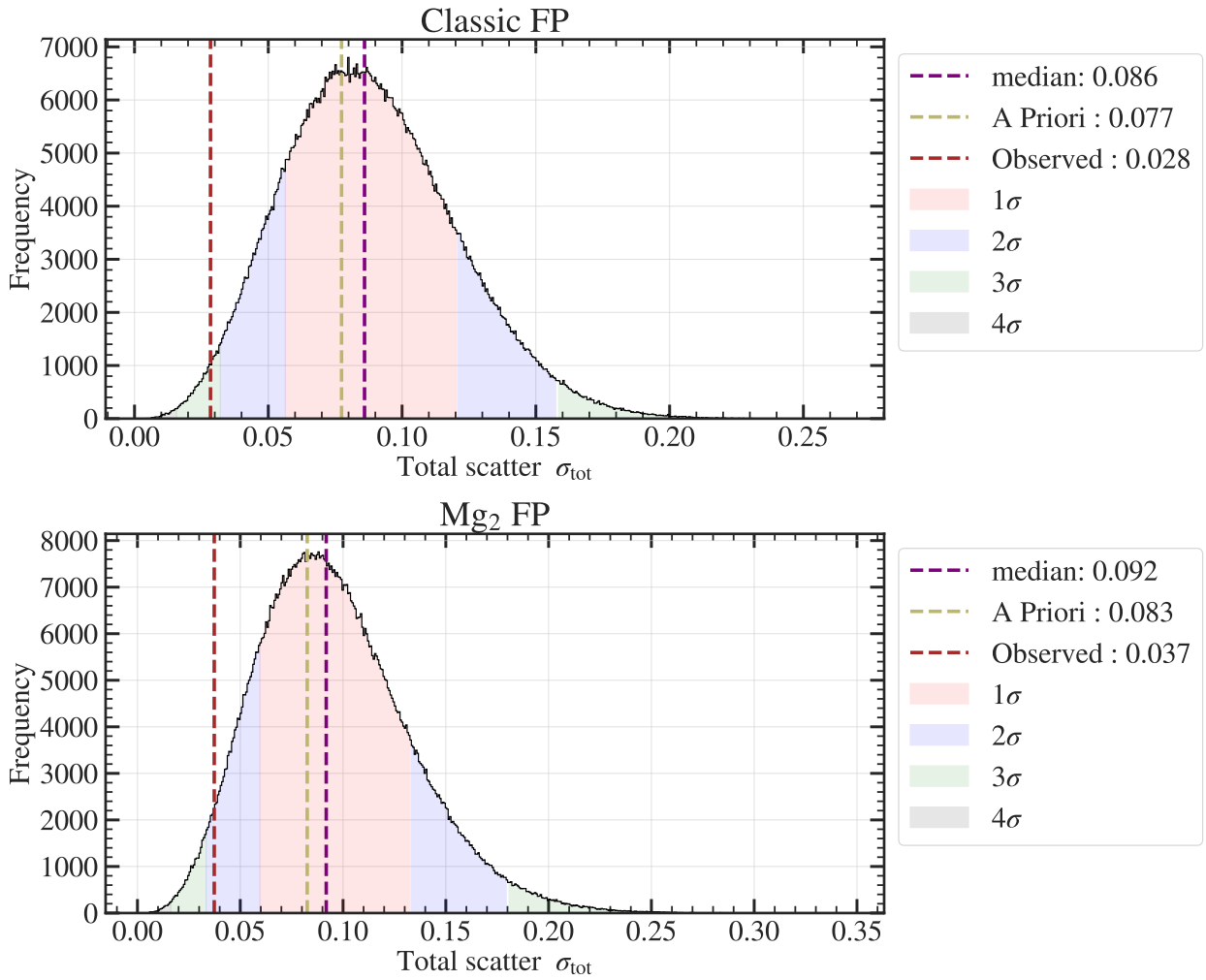

Figure 28: Histogram of the sampled total scatter (σ_{tot}) in dex from the classic (top panel) and Mg_2 (bottom panel) FP values as shown in Figure 27. The sample consists of $n = 10^6$ trials. Both distributions use 500 bins. Vertical dashed lines indicate the median, a priori and observed formal rms scatter as indicated in the legends. Shaded areas indicate the 1, 2, 3 and 4σ deviation from the median.

We observe a strong agreement between the median and a priori value which falls within the 21th percentile of the median. Naturally, the distribution is shifted towards higher values compared to the observed value, since we have added 14% intrinsic scatter to the measurement errors. However, sampling the distribution without the intrinsic scatter would also result in a shift towards higher values. This is simply due to the observed value falling very close to the FP relation, thus driving the total scatter down. As we

sample enough σ_{tot}, we increasingly include values in the wings of the likelihood function for each point. We find the distribution of σ_{tot} for the Mg_2 FP relation, shown in the bottom panel, to be narrower than that of the classic FP. This is due to the observed total scatter, which is slightly smaller around the Mg_2 FP.

In both cases, we find the observed σ_{tot} value to lie around the 2σ interval. More specifically, they fall in the 93^{th} for the Mg_2 FP and 97^{th} for the classic FP. This is perhaps not as significant as expected, but still a clear 1σ outlier. We thus find it likely that the observed scatter in the FP in Leo I is different from that of the Coma cluster. Additionally, this emphasises the suspicion of overestimated measurement errors for the observed velocity dispersion. Nevertheless, given the observed significance, we cannot reject any of the models. For transparency, we will consider 3 assumptions.

In the first assumption, we include both measurement errors and the estimated intrinsic scatter from Coma. This will provide the largest uncertainty on the distance estimate and can be considered a conservative approach. We denote this scenario by $\sigma_{\text{int+obs}}$. Secondly, we will determine the distance only based on the measurement errors (denoted σ_{obs}).

Finally, we will assume that the measurement error is overestimated and discard it entirely along with the intrinsic scatter (denoted σ_{alt}). Instead, we position NGC 3379 and NGC 3377 at the same distance, thus changing the zero points. From this, we can determine a new relation between NGC 3379 and NGC 3377 from which we compute the total scatter, which is then propagated through the distance estimate. For simplicity, we shall call this a revised FP (or alternative relation) as it is based on the structural analysis in this thesis. Note that this is not actually a new FP for Leo I as it is done using only two galaxies. We can determine the new zero point γ' at a given distance using:

$$\gamma' = \gamma_0 - \log\left(\frac{D'}{D_0}\right), \tag{113}$$

where γ_0 is the known zero point, D_0 is the known distance associated with the zero point and D' is the distance we wish to calibrate to. We choose $D' = 10.86$ Mpc, thus positioning NGC 3379 at the distance of NGC 3377. This is shown in Figure 47 in Appendix H. Given

that NGC 3379's size remains fixed and the galaxy is now placed further away, the new zero point will be smaller and as a result, NGC 3379 will move upwards compared to Figure 27.

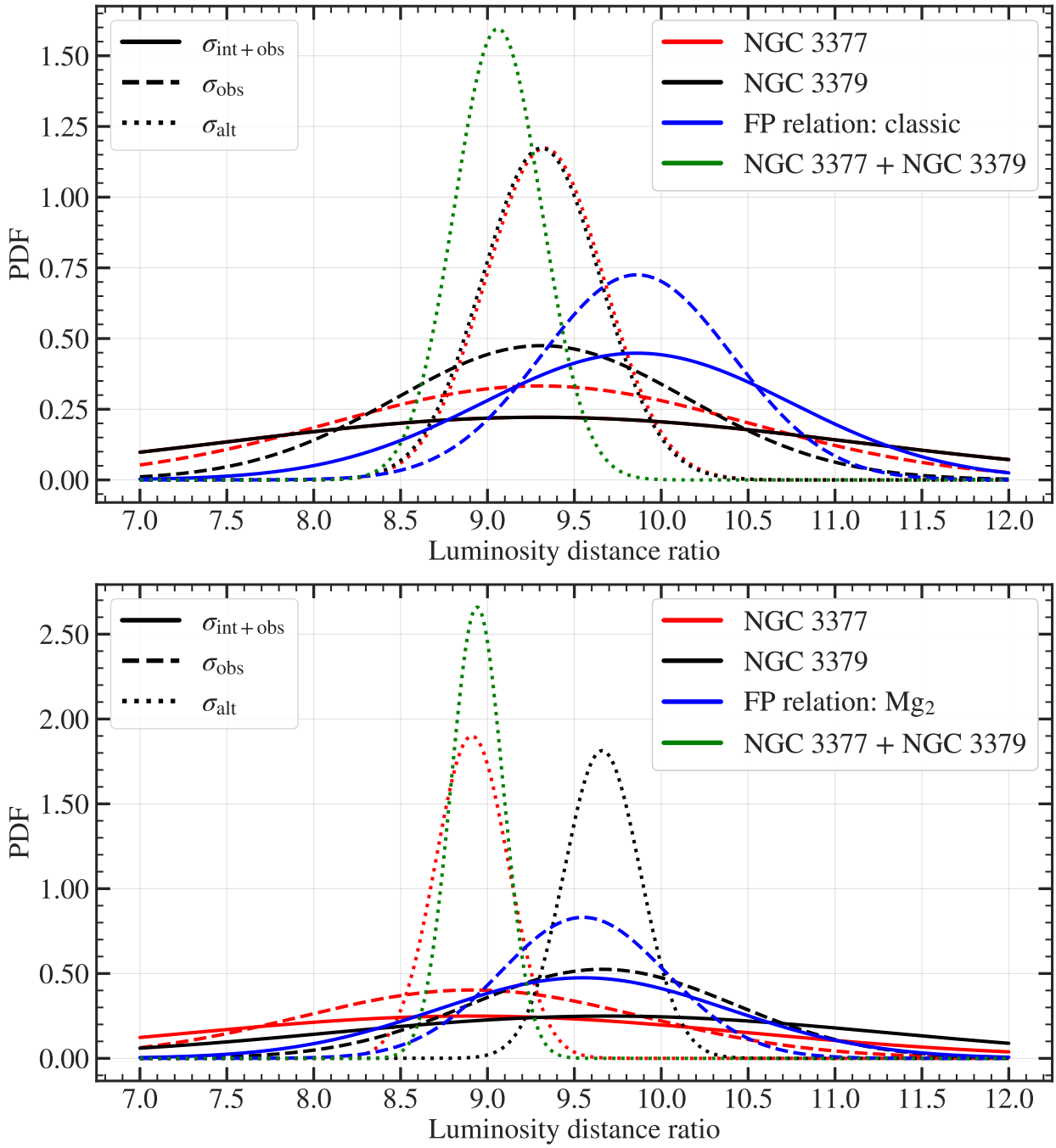

Figure 29: **Luminosity distance ratios between Leo I and Coma**. *Top panel*: Computed ratios for the classic FP. *Bottom panel*: Computed ratios for the Mg_2 FP. Line styles indicate the assumption of uncertainties. $\sigma_{\mathrm{int+obs}}$ includes both the measurement error and an additional 14% intrinsic error. σ_{obs} includes only the measurement error. For σ_{alt}, both the measurement and intrinsic errors are discarded and instead only the scatter between NGC 3379 and NGC 3377 is used. Colours indicate the object used to compute the ratios. The blue curve (FP relation) is based on the fit of NGC 3379, NGC 3377, NGC 3384 and NGC 3412. Similarly, the NGC 3377 + NGC 3379 curve is for the alternative relation between only these two members.

In Figure 29, we plot the luminosity distance ratios between Leo I and Coma for these 3 assumptions as indicated by the line styles in the legend. The colours show the object used to compute the zero point and subsequently the distance ratio. The full list of derived zero points, angular diameter distance and luminosity distance ratios is tabulated in Table 19 in Appendix I for both the classic FP and Mg_2 FP.

For the classic FP, we find both NGC 3379 and NGC 3377 provide a luminosity distance ratio of $D_{L,\mathrm{ratio}} \approx 9.3$ with errors ranging between 0.34 (σ_{alt}) and 1.8 ($\sigma_{\mathrm{int+obs}}$) depending on the assumption. The fitted classic FP relation provides a slightly higher estimate at $D_{L,\mathrm{ratio}} = 9.86$ with errors ranging between 0.55 (σ_{alt}) and 0.89 ($\sigma_{\mathrm{int+obs}}$), where the errors are determined from fit. Finally, we find a lower ratio of $D_{L,\mathrm{ratio}} = 9.06 \pm 0.25$ for the alternative relation. For the Mg_2 FP, we find similar patterns, but the ratio is shifted between -0.3 to -0.4 compared to the classic relation[7].

For the classic FP as shown in the top panel of Figure 29, we find the ratios determined from NGC 3377 and NGC 3379 to be consistent with each other and positioned between the two extremes in the working assumptions. We find a trend towards smaller ratios when choosing NGC 3379 and NGC 3377.

We now determine the distance to the Coma cluster. This is done using 4 objects. Since NGC 3368 is established as part of 68-77-grp, we can determine the distance by the ratio from NGC 3377. We use the discussed distance measurement by Jang & Lee (2017) of $D_{\mathrm{NGC\,3368}} = (11.1 \pm 0.3)$ Mpc ($\pm$0.3 Mpc in systematic error), and the distances for 68-77-grp, NGC 3379 and SN1998bu. We note that SN1998bu probably has unaccounted uncertainty as outlined in Section 3. The distances are shown for each assumption in Figure 30. For the full Table of distances, see Table 20 in Appendix I, where the systematic error are also listed.

For the classic FP relation, we find the distance to lie between (100 - 110) Mpc with uncertainties between (7-10) Mpc depending on the chosen object and assumption, where NGC 3379 and SN1998bu are in the lower limit and NGC 3368 and 68-77-grp are in the upper limit. We find that the alternative relation between NGC 3379 and NGC 3377 provides

[7]For full overview see Table 19.

the lowest estimates for the distance to the cluster, but also the most precise given the drastically lower uncertainty. In Table 10, we tabulate the weighted average of distances to Coma, $\bar{D}_{\mathrm{Coma}}$, for each assumption and the 3 objects: NGC 3368, 68-77-grp and NGC 3379. Note that SN1998bu is not included in the average.

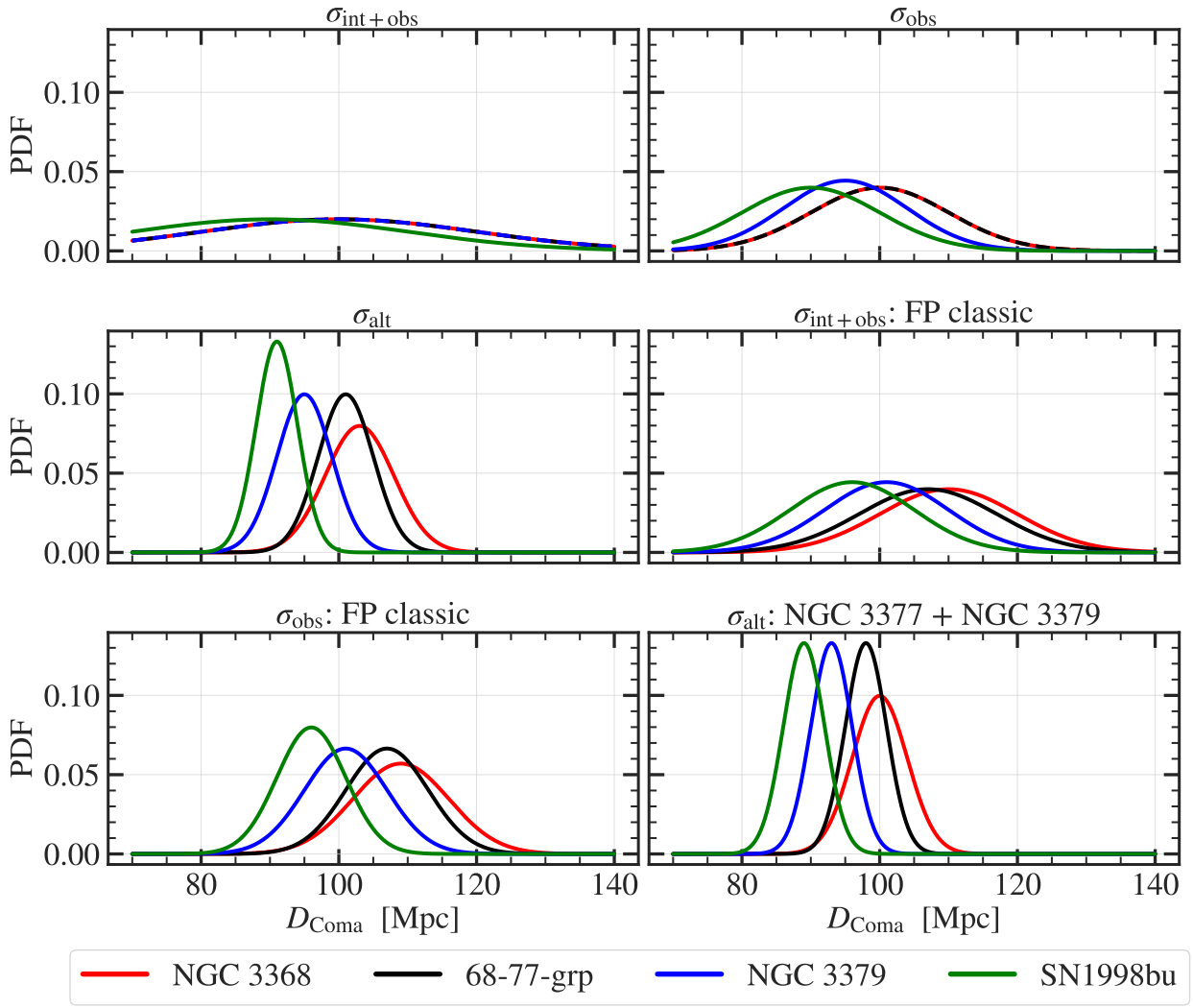

Figure 30: **Distance to Coma**: Computed distances are only for the classic FP. Note that only random uncertainties are plotted (see Table 20 for systematic uncertainties). Each subplot is labelled based on the 3 working assumptions. $\sigma_{\mathrm{int+obs}}$ includes both the measurement error and an additional 14% intrinsic error. σ_{obs} includes only the measurement error. For σ_{alt}, both the measurement and intrinsic errors are discarded and instead only the scatter between NGC 3379 and NGC 3377 is used. Subplots labelled *FP Classic* or *NGC 3377 + NGC 3379* show distances obtained through the fit of the classic FP and the alternative approach using NGC 3377 and NGC 3379. Colours indicate the object used to compute the distance as indicated in the legend.

Table 10: **Distance to Coma:** Column 1 shows the assumption for determining the uncertainty, where $\sigma_{\text{int+obs}}$ includes both the measurement error and an additional 14% intrinsic error. σ_{obs} includes only the measurement error. For σ_{alt}, both the measurement and intrinsic errors are discarded and instead only the scatter between NGC 3379 and NGC 3377 is used. The FP classic rows in Column 1 are based on the fit of NGC 3379, NGC 3377, NGC 3384 and NGC 3412. The NGC 3377 + NGC 3379 rows are from the alternative approach including only these galaxies. Column 2 shows the weighted average distance to Coma. Columns 3 and 4 show the random and systematic uncertainty respectively. All distances are in Mpc.

Assumption	$\bar{D}_{\text{Coma}}$ [Mpc]	$\sigma_{D_{\text{Coma}}}$ (random) [Mpc]	$\sigma_{D_{\text{Coma}}}$ (systematic) [Mpc]
$\sigma_{\text{int+obs}}$	100	10	10
σ_{obs}	98	6	6
σ_{alt}	99	2	3
$\sigma_{\text{int+obs}}$: FP classic	106	6	6
σ_{obs}: FP classic	105	4	4
σ_{alt}: NGC 3377 + NGC3379	96	2	3

4.4.2 The peculiar velocity of the Coma cluster

Once the Coma Cluster is located in the discussed simulations, we can determine the centre position along the line of sight in terms of the co-moving distance. We find Coma to be positioned at roughly $\sim$76 h^{-1}Mpc for the BORG model and $\sim$74 h^{-1}Mpc for CARRICKS. In Figure 31, we plot the density profile from the BORG model.

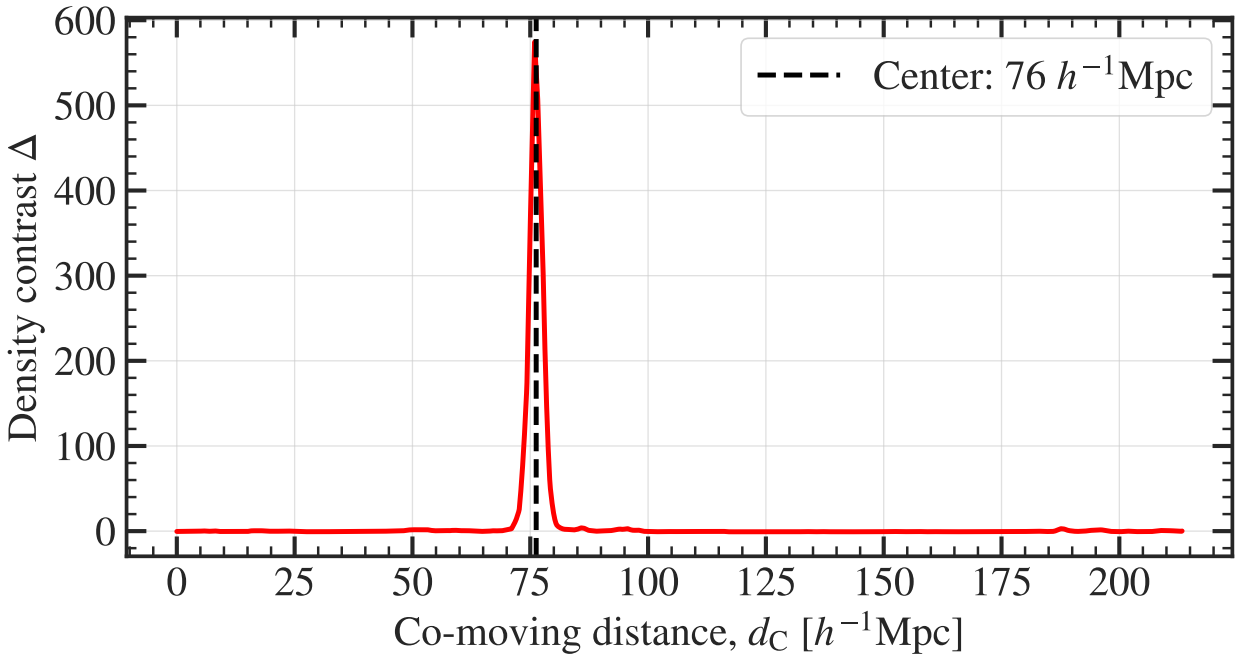

Figure 31: Density profile of the Coma cluster from the BORG model.

As shown in Figure 31, we find a very clear and distinct profile of the Coma cluster,

allowing us to locate the centre easily. It is worth mentioning that the density profile is different in the CARRICKS model as shown in Figure 48 in Appendix J. However, given the analysis is identical for both models, we have chosen to only illustrate the profiles from the BORG model as this also provides the uncertainty profile along the line of sight.

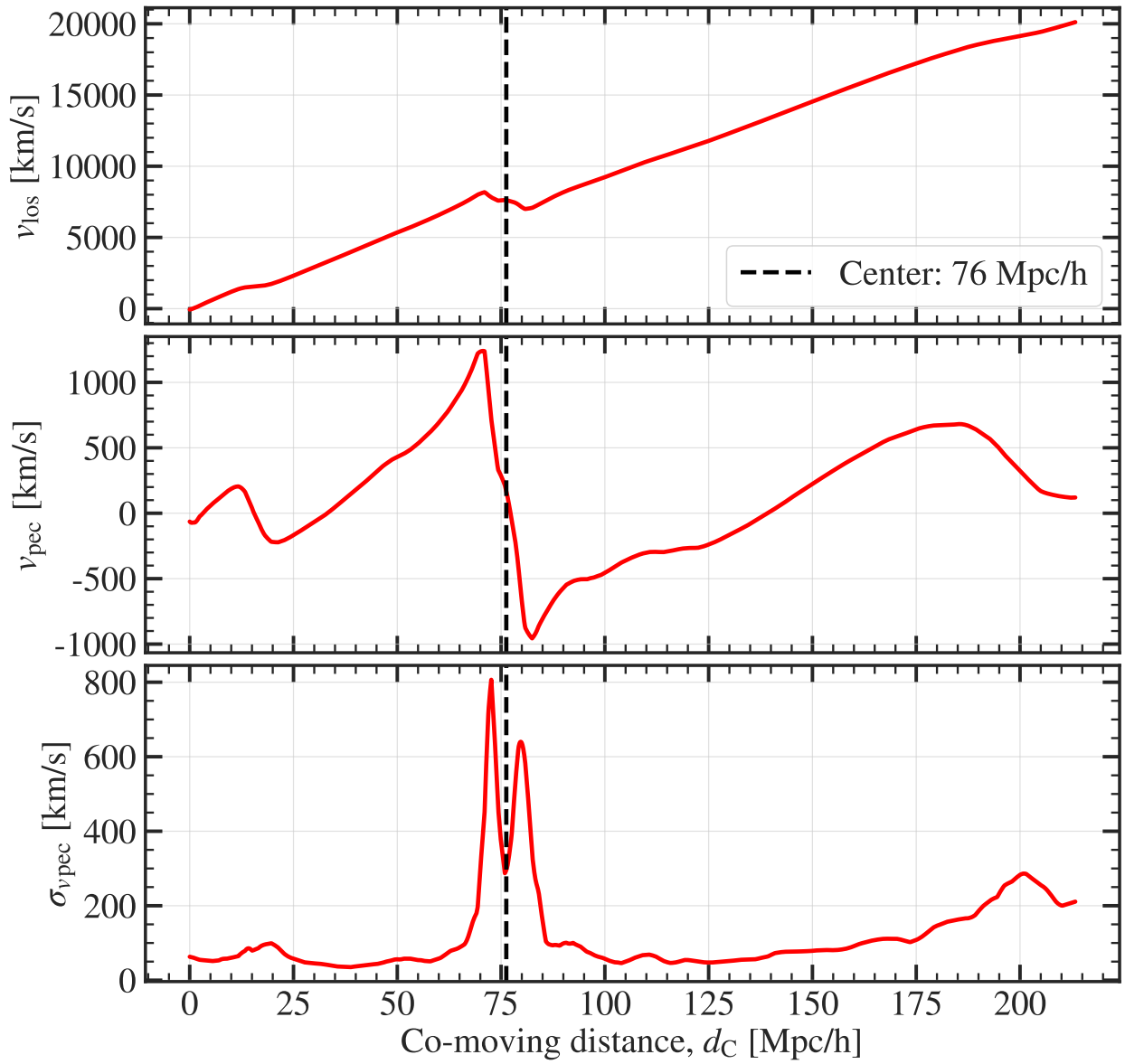

Figure 32: **Velocity profiles of the Coma cluster**: The *top panel* illustrates the line-of-sight velocity profile, the *middle panel* shows the peculiar velocity profile, while the *bottom panel* depicts the uncertainty on the peculiar velocity estimate. The vertical dashed line indicates the centre.

In Figure 32, we show the velocity profiles for the line-of-sight velocity (v_{los}), peculiar velocity (v_{pec}) and the uncertainty on the peculiar velocity ($\sigma_{v_{\text{pec}}}$). The line-of-sight profile demonstrates what we would expect from the Hubble-Lemaître law quite well. The bump

along the curve is the cluster. In terms of radial velocity, there is an increase along the line of sight in velocity as we approach the edge of the cluster due to in-falling material towards the centre. Likewise, we see a decrease in velocity as the material on the opposite side falls towards the centre. This is more prominent in the peculiar velocity profile where we observe a rapid transition around the centre of the cluster.

The uncertainty profile is described by a 'double-horn' shape, where the uncertainty on the peculiar velocity is at its minimum at the centre of the cluster. The two peaks are positioned at a transition between in-falling and virialised parts of the cluster. Thus, the predicted peculiar velocity is very sensitive to the estimated halo mass as it can easily vary between the peculiar velocity of Coma and the in-falling velocity.

The predicted peculiar velocity of Coma at the centre is observed to be $v_{\mathrm{pec,Coma}} = (170 \pm 300)\mathrm{kms}^{-1}$ for the BORG model and $v_{\mathrm{pec,Coma}} = (20 \pm 150)\mathrm{kms}^{-1}$ for the CARRICKS model. Note that both estimates include an estimate of v_{ext}, which accounts for external interactions with the volume surrounding the cluster. Alternatively, one could determine the peculiar velocity directly from the profile without determining the centre from the density profile. In this case, one would locate the middle between the maximum and minimum. We find this to be consistent with the stated values, but in both cases, these are found to be shifted by roughly -20 kms^{-1}.

In order to test the robustness of this estimate, we wish to redo the computation by choosing random points scattered along the projected size of the cluster. We adopt a virial radius of Coma of $R_{\mathrm{virial}} = 1.99\ h^{-1}\mathrm{Mpc}$ (Kubo et al., 2007). We sample a total of $N = 5497$ points ranging from the centre to the edge of the cluster. In Figure 33, we plot the distribution of the predicted peculiar velocity for each point and the associated uncertainty. It is reassuring to see that the distributions are quite narrow and agree to a high degree with the estimated values for the centre.

For the BORG model, we find $v_{\mathrm{pec,mean}} = (164 \pm 31)\ \mathrm{kms}^{-1}$ and similarly $v_{\mathrm{pec,mean}} = (-3 \pm 6)\ \mathrm{kms}^{-1}$ for the CARRICKS model. Note that the uncertainty is the standard deviation and not the uncertainty on the predicted value. We find a very small spread in the uncertainty with a standard deviation of 4 kms^{-1}, suggesting that the predicted

uncertainty is robust.

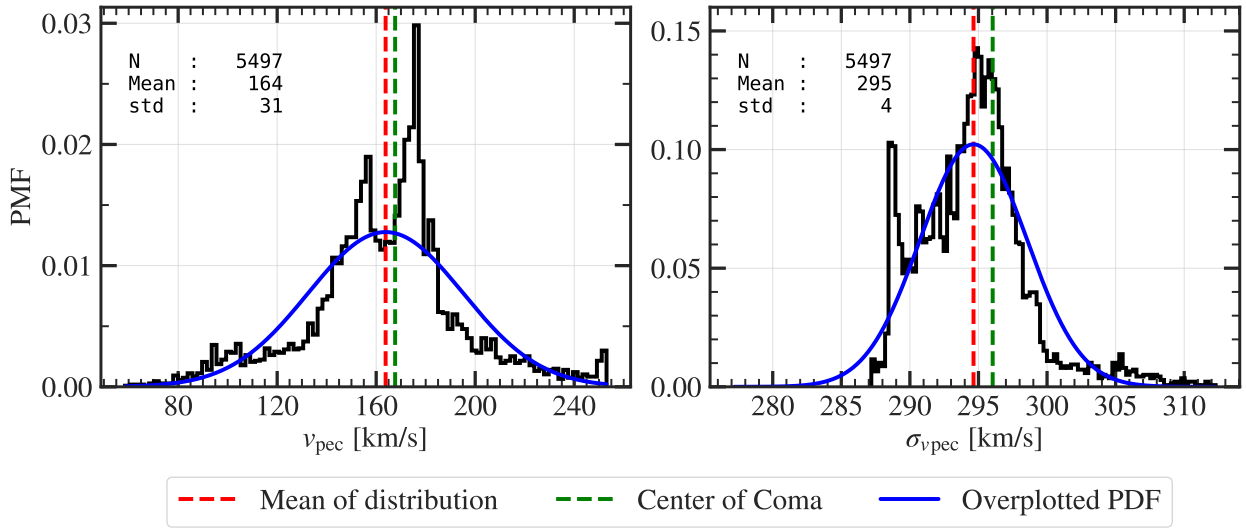

Figure 33: **Left panel**: Distribution of sampled predicted peculiar velocities of the Coma cluster (BORG model). **Right panel**: Distribution of the associated uncertainty on the predicted peculiar velocity. The blue curve show the overplotted PDF. Vertical lines indicate the mean of the distribution and the predicted value from the centre of the cluster (see legend).

We find the estimated peculiar velocities to be quite small and close to zero (especially for the CARRICKS model), which may indicate some issues with either this approach or the simulations. To overcome this concern and validate the results, we have estimated the peculiar velocities of four other larger clusters in the low-redshift Universe. We repeat the sampling and tabulate the mean peculiar velocity for the clusters and the standard deviation of the sampled distribution in Table 11. Note that this is done with the CARRICKS model.

Table 11: Mean peculiar velocity ($v_{\mathrm{pec,mean}}$) for 5 clusters in the low-redshift Universe from the CARRICKS model. The standard deviation from the sampled distribution is shown in Column 3, while the uncertainty on the predicted value is ± 150 kms^{-1}.

Cluster	$v_{\mathrm{pec,mean}}$ [kms^{-1}]	$\sigma_{v_{\mathrm{pec}}}$ [kms^{-1}]
COMA	20	20
VIRGO	320	30
PERSEUS	-90	20
HYDRA	-80	100 [a]
FORNAX	-180	6

[a] This estimate is not stable as the density profile around HYDRA is double-horned.

As shown in the table, we find a variety of estimates of the peculiar velocities for the clusters. We, therefore, accept the predicted peculiar velocity of Coma. The resulting recession velocity of Coma corrected for the peculiar velocity is then $v_{\rm Coma} = (7050 \pm 300)$ kms^{-1} for the BORG model and $v_{\rm Coma} = (7190 \pm 160)$ kms^{-1} for the CARRICKS model.

4.4.3 Estimates of the Hubble constant

In Table 12, we tabulate the derived estimates of the Hubble constant. The values are weighted averages for the 3 objects: NGC 3368, 68-77-grp and NGC 3379. We provide an error budget as shown in Columns 5, 6 and 7 for the 3 quantities: the distance (cont$_D$), the velocity of Coma (cont$_V$) and the adopted luminosity distance ratio (cont$_\gamma$). These values show the relative contribution in percentage to the random uncertainty.

Unsurprisingly, we find the velocity of Coma to have the smallest contribution to the error in the estimate. We find the largest contribution from the luminosity distance ratio under the assumptions where we include intrinsic scatter. Vice-versam when we use the alternative relation, which increases the contribution from the velocity. This is particularly seen when using the BORG model, where the larger uncertainty on the peculiar velocity results in up to 50% contribution to the total error on the Hubble constant.

Table 12: **Hubble constant estimates**: Column 1 lists the assumption for determining the uncertainty in the luminosity distance ratio, where $\sigma_{\rm int+obs}$ includes both the measurement error and an additional 14% intrinsic error. $\sigma_{\rm obs}$ includes only the measurement error. For $\sigma_{\rm alt}$, both the measurement and intrinsic errors are discarded and instead only the scatter between NGC 3379 and NGC 3377 is used. Columns 2, 3 and 4 show the weighted average of the estimated values of the Hubble constant, the random uncertainty and the systematic uncertainty, respectively. The weighted average is for the 3 objects: NGC 3368, 68-77-grp and NGC 3379. Columns 5, 6 and 7 show the contribution to the error from the 3 quantities: the distance (cont_D), the velocity of Coma (cont_V) and the adopted luminosity distance ratio (cont_γ). All contributions are given in percentages.

Assumption	H_0 [km s^{-1}Mpc^{-1}]	$\sigma_{\rm random}$ [km s^{-1}Mpc^{-1}]	$\sigma_{\rm systematic}$ [km s^{-1}Mpc^{-1}]	cont_D [%]	cont_V [%]	cont_γ [%]
CARRICKS						
$\sigma_{\rm int+obs}$	73	9	9	51	1	48
$\sigma_{\rm obs}$	75	4	4	42	2	56
$\sigma_{\rm alt}$	74	2	3	50	14	36
$\sigma_{\rm int+obs}$: FP classic	69	4	4	49	3	48
$\sigma_{\rm obs}$: FP classic	69	3	3	50	7	43
$\sigma_{\rm alt}$: NGC 3379 + NGC 3377	76	2	2	48	21	31
BORG						
$\sigma_{\rm int+obs}$	72	9	9	50	2	48
$\sigma_{\rm obs}$	73	5	5	40	7	53
$\sigma_{\rm alt}$	72	3	3	37	37	26
$\sigma_{\rm int+obs}$: FP classic	68	4	4	45	10	45
$\sigma_{\rm obs}$: FP classic	68	3	3	42	22	36
$\sigma_{\rm alt}$: NGC 3379 + NGC 3377	74	2	3	30	50	20

In Figure 34, we plot the H_0 estimates along with the recent estimates from type Ia supernovae and Cepheids (black curve) (Riess et al., 2021) and CMB (red curve) (Planck Collaboration et al., 2020). In addition, we plot the H_0 estimates from SN1998bu distances and velocities obtained from CARRICKS. Solid curves indicate estimates based on single objects (NGC 3379, NGC 3368 and 68-77-grp), while dashed curves are based on either the classic FP relation or the alternative relation based on NGC 3379 and NGC 3377 (see Table 12).

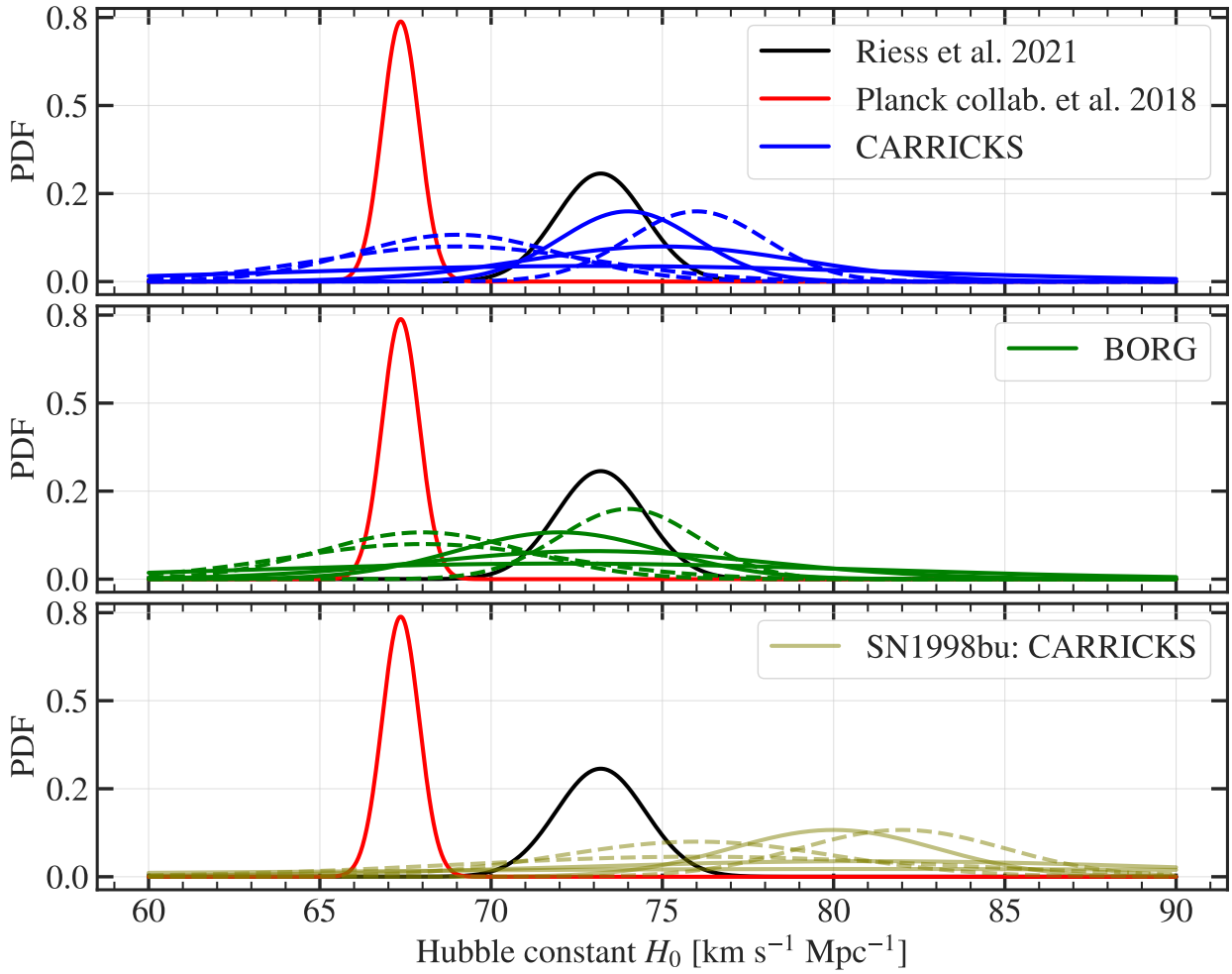

Figure 34: **Hubble constant estimates**: *Top panel*: Estimates adopting $v_{\rm Coma} = (7190 \pm 160)$ kms^{-1} from the CARRICKS model. *Middle panel*: Estimates adopting $v_{\rm Coma} = (7050 \pm 300)$ kms^{-1} from the BORG model. *Bottom panel*: Estimates adopting the CARRICKS model and SN1998bu. The black and red curves show recent estimates from Riess et al. (2021) and Planck Collaboration et al. (2020) respectively. Solid curves indicate estimates based on single objects (NGC 3379, NGC 3368 and 68-77-grp), while dashed curves are based on either the classic FP relation or the alternative relation based on NGC 3379 and NGC 3377 (see Table 12).

As seen in Figure 34, we find the lowest estimates of H_0 when using the BORG model. Estimates based on the classic FP relation, which assumes the same distance for the members of Leo I, are shifted towards the Planck Collaboration et al. (2020) value of (67.36 ± 0.54) kms^{-1}Mpc^{-1}, while estimates based on the alternative relation are in better agreement with the Riess et al. (2021) value of (73.2 ± 1.3) kms^{-1}Mpc^{-1}. SN1998bu estimates are only for reference. They are the largest estimates, but also with the largest uncertainties.

If we consider the alternative approach ($\sigma_{\rm alt}$), we find an estimate of $H_0 = (74 \pm 2\,(\text{stat}) \pm$

3 (sys)) kms^{-1} Mpc^{-1} for the CARRICKS model, and $H_0 = (72 \pm 3$ (stat) ± 3 (sys)) kms^{-1} Mpc^{-1} for the BORG model. This is surprising, since the classic FP relation obtained from Hjorth & Tanvir (1997) provides estimates closer to the CMB-based value. Thus, from the structural analysis and revised FP ratios, we find the estimated H_0 values shifting towards the Cepheid-based value.

4.5 Discussion of H_0 estimates

From a revised structure of the Leo I group, we obtain new estimates of the distance to the Coma cluster through a revised Fundamental Plane. We find a significant discrepancy between the estimated intrinsic scatter of the FP in Leo I and that in the Coma cluster. We, therefore, estimate the Hubble constant while employing 3 different assumptions to determine the uncertainty on the luminosity distance ratio. This shows a significant difference in the contribution to the error on H_0 from the distance ratio, which drops from 48% to 36% (CARRICKS) or 26% (BORG), depending on the adopted model of peculiar velocities.

However, the dominant source of uncertainty is the distance estimate to the Coma cluster. Obtaining a precise value of the Hubble constant is a complex task especially when carried out in the low-redshift Universe. The choice of Coma comes with its advantages and disadvantages. The main advantages are that the cluster is well-studied and it contains a larger number of members, thereby avoiding some of the low-statistics issues we have faced when studying Leo I. The main disadvantage is its large distance. From eq. (112), we find that the recession velocities of objects are dominated by $v_{\rm pec}$ at small distances, but becomes increasingly negligible with larger distances (directly proportional). This means that the velocity is more precise at larger distances.

Ideally, we would choose objects even closer than Coma, where the distances are more precise. The challenge, in this case, is that the velocity then becomes more uncertain. This can be avoided if the peculiar velocities can be determined with high accuracy. In fact, this approach might be more beneficial as we can choose clusters with significantly more members than Leo I and, hence, avoid low statistics. Nevertheless, predicting peculiar ve-

locities remains a complex task. This analysis would suggest that peculiar velocities may be adequately determined through either the CARRICKS or BORG model, but one runs the risk of introducing biases or yet unknown systematic effects when using simulations.

5 Discussion

Establishing accurate extragalactic distances is an immense challenge. The situation will keep on improving as better detectors and new techniques become available. Nevertheless, we are faced with numerous challenges related to the quality of observations and calibration, which subsequently influence the estimated value of H_0. One of the main advantages of Leo I is its relatively close distance to us at about $\sim$10-11 Mpc. While this offers the opportunity of applying accurate techniques such as the period-luminosity function or the TRGB method, we are dominated by low statistics as Leo I contains a sparse number of galaxies.

We approach this problem by probing the structure of the group and its unique giant HI structure. Understanding the origin of the HI structure is crucial for understanding the history of Leo I. Fortunately, 21 cm observations of the HI allow us to study it from a dynamical perspective, thereby avoiding the challenges related to distance estimation. From our analysis in Section 2, we find that the structure is ill-described by a simple single Keplerian orbit. The stability of the model is particularly in question when considering the derived period of $P = (5 \pm 1)$ Gyr. Given the well known dynamics described by Kepler's laws, we would not expect the period to be on similar scales as the Hubble time. In addition, we find the period of the ring to be almost twice that of the crossing time of Leo I, further casting doubt on the model and invalidating the derived mass-to-light constraints of $M/L = (14 \pm 11) M_\odot / L_\odot$. Given the likely origin of the structure through a collision between NGC 3368 and NGC 3384, we still consider the HI structure to deviate from the overall dynamics of the group as it cannot be virialised.

This has consequences for the structure of the Leo I group as NGC 3368, NGC 3379 and NGC 3368 are not linked by the HI structure. This is in disagreement with the findings of Schneider (1985) and Hjorth & Tanvir (1997) which adopt this depiction of the group. As a result, we have to undertake the challenge of proposing a new structure of the group, which per definition will provide weaker distance estimates. The proposed link between the members by Schneider (1985) allows one to compute distances to each member and deriving an accurate measure of the groups distance from a simple average. In the ex-

treme case where all members are placed at the same distance, the uncertainty on this estimate will drop as $\sqrt{7}$. Given precise enough techniques, this would provide a very precise estimate of the distance to the group.

However, doing so also naively assumes that the group is well-described by a sphere. In Section 3, we find that this is not the case. Adopting the well-understood and precise techniques available for determining distances in Leo I, we compare the relative distances to each of the members and yet we find that only TRGB-based measurements provide sufficiently high precision for obtaining statistically significant results. From TRGB measurements, we discover a large separation within Leo I, suggesting that it may be described by two subgroups; one consisting of NGC 3379 and NGC 3351, and the other of NGC 3368 and NGC 3377. Although not as significant, we find similar patterns reflected in the SBF- and Cepheid-based measurements. From collision models of the origin of the HI structure between NGC 3368 and NGC 3384, as presented by Michel-Dansac et al. (2010), it is very likely that NGC 3384 would belong to the 68-77-grp. This raises questions as to whether we can assume a spherical model for the group's structure as emphasised when comparing the projected size of the group to its depth.

Considering the groups' recession velocities, it becomes quite clear that the group is irregular. The mass estimates of the group obtained from the virial theorem and through the projected mass all fall short of what is expected when comparing the derived mass-to-light ratio to that of similar groups. As stated by Heisler et al. (1985), the virial theorem mass estimator has obvious challenges as it is biased and inefficient especially in the low statistics case. While adopting alternative definitions through the projected mass estimator increases the predicted mass-to-light ratio up to $120 \pm 30 M_{\odot}/L_{\odot}$, it still falls significantly below the lower limit for groups of 140 $M_{\odot}/L_{\odot}$ as derived in Girardi et al. (2002). Note that since we have no prior knowledge about the information of the distribution of the eccentricities of the galaxy orbits, we tested both limits of pure isotropic and radial orbits.

Using the velocity dispersion of the group, we obtain a crossing time of ~ 9 Gyr, clearly indicating the group is not virialised. From Stierwalt et al. (2009), we know that the

galaxies in the Leo constellation as a whole are not virialised, suggesting that they should be divided into two entities (M66 Group and Leo I). It is surprising to find that the Leo I group are not in equilibrium as well. This could indicate that the group is younger than expected and have not had enough time to be virialised. Adding further confusion to the structure of the Leo I group is its proximity to the Virgo cluster, which leads to velocity crowding and thus the appearance of more group structure than what may actually exist in practice (Stierwalt et al., 2009). In Table 13, we summarise the previous assumptions on the structural properties of the group, along with the results from this analysis explaining why these assumptions are not valid.

Table 13: Previous assumptions on the structural properties of Leo I are listed in Column 1. Column 2 contains summarised results from the analysis in this thesis explaining why the previous assumptions are invalid.

Previous structural properties	This analysis
The HI structure in Leo I follows an elliptical orbit.	The HI structure does not follow an elliptical orbit given the poor match with such model. It is more likely a spiral structure which originated from a collision between NGC 3384 and NGC 3368.
NGC 3379 is in the focus of the HI structure's motion.	The derived position of the focus is shifted from that of NGC 3379 and it can, therefore, not be the central mass. NGC 3379 is more likely located in the foreground relative to the HI structure given the distance obtained through TRGB-based measurements.
The mass-to-light ratio derived from the HI structure's motion is modest, indicating low dark matter content.	The derived mass-to-light constraint on NGC 3379 is not valid given the overall poor match with the fitted model. We find it more likely that the mass is underestimated.
NGC 3368 is located at the same distance as NGC 3379 due to interaction with the HI structure.	The observed interaction between the HI structure and NGC 3368 tie the two objects together. However, NGC 3379 is not at the same distance as NGC 3368, since it is not at the focus of the HI structure.
The Cepheid-based distance to NGC 3368 can be used to calibrate the FP since it is at the same distance as NGC 3379, providing an accurate estimate of the distance to the Coma cluster.	Given the revised structure of the group, we know that the distance to NGC 3368 cannot be used along with NGC 3379 to calibrate the FP. However, it is useful when considering NGC 3377, but given much higher precision of the TRGB measurements, the previous approach involving Cepheids would be futile.

Equipped with the knowledge about the groups structure, we determine the distance to

the Coma cluster. There is plenty of room for improvement in this approach as we are left with only NGC 3379 and NGC 3377 for obtaining reliable results. We find that the luminosity distance ratio, as obtained through the Fundamental Plane, contributes between 53% and 56% of the total uncertainty in H_0 when adopting only measurement errors and depending on the estimate of peculiar velocity. This may be reduced significantly by 23-30% when adopting the revised relation in which we discard the expected intrinsic scatter of the FP from Coma and the measurement errors, and instead determine the uncertainty from scatter between NGC 3379 and NGC 3377. We must stress, nevertheless, that there is a strong caveat to this approach as we essentially determine the uncertainty from two measurements.

The predicted peculiar velocities contribute with 2-7% when including measurement errors and up to 37% when adopting the alternative relation. Hence, given high enough precision on the distance estimate to Coma, the uncertainty on the peculiar velocity estimate becomes important. While the peculiar velocity of Coma is only about $\sim$2% of the observed radial velocity, its uncertainty is 6 times as large in the case of the BORG estimate.

The obtained estimates of H_0 vary between the very precise values from observations of type Ia supernovae and Cepheids, $H_0 = (73.2 \pm 1.3)$ kms^{-1}Mpc^{-1} (Riess et al., 2021), and of the CMB, (67.36 ± 0.54) kms^{-1}Mpc^{-1} (Planck Collaboration et al., 2020). On one hand, we find a trend towards the CMB-based prediction when considering Leo I as a whole and thus assuming equal distances for all its early-type members when determining the FP. On the other hand, when following the revised structure in this thesis, we shift towards the Cepheid-based prediction. This is the case for both the CARRICKS and BORG models, although values based on the BORG model are shifted towards lower values.

The derived estimates based on the revised structure are, therefore, in good agreement with the recent estimate from Riess et al. (2021). While we aimed at providing independent estimates of H_0 from Leo I that could help clarify the Hubble tension, we find that it is instead cemented by our analysis. The major weakness of this approach is of course the use of the cosmic distance ladder. Even though we have precise measurements

available for Leo I, we are still left with large systematic uncertainties, which are continuously updated as better calibration methods becomes available, such that there might be yet unknown systematic uncertainty/effects. In addition, the measurements in Leo I are all obtained through secondary indicators and rely on well-established distances (in this case the LMC). This long chain of obtaining an estimate of the distance to Coma has an increasing uncertainty for each of the steps, with the uncertainties propagating through.

If we had similar precision on the distance to Coma as in Leo I, we would find uncertainties on H_0 that are actually comparable with that of Riess et al. (2021), as seen in the estimates based on the revised relation of the FP. This approach would suggest that we cannot circumvent the discussed balance between distance and velocity by measuring distance at small scales and stepping out to larger distances. However, given the capabilities of the James Webb Space Telescope, there is a possibility of obtaining high precision distance measurements of the Coma cluster. With the ability of resolving individual stars in Coma, we would be able to apply methods such as TRGB and Cepheids, which would justify redoing this analysis.

Alternatively, we may consider a completely different approach. The analysis in this thesis is based on the low statistics case in which we carry as much information as possible about nearby objects into obtaining an estimate of H_0. Based on the precision in the CARRICKS and BORG reconstruction of the low-redshift Universe, one could estimate H_0 at relatively short distances by accounting for the peculiar velocity of nearby clusters. Given the much larger number of members, this would allow for very accurate distances, but will of course be very sensitive to the estimate of the peculiar velocity.

6 Conclusions

We aim at estimating H_0 from precise distance measurements of the Leo I group. We provide a detailed structural and dynamical analysis of the group. We re-analyse the motion of the giant HI structure in the group and fit a model Keplerian orbit to its radial velocities. We find the observed motion to be ill-described by such a model and conclude that it is more likely a transient phenomenon rather than a primordial one as previously

thought.

From high precision TRGB measurements, we are able to probe the structure of the group in which we propose two subgroups. Whilst we expect all seven members to be associated with either one of the groups, we find the most significant connection between NGC 3368 and NGC 3377 from which we name one of the subgroups 68-77-grp. Taking into account recent collision models describing the origin of the HI structure, we expect NGC 3384 to be part of this group while NGC 3379 and NGC 3351 would form their own group. NGC 3412 is more ambiguous and we find indications that NGC 3849 might be an intermediate member between the Leo I and M66 groups. From derived mass-to-light ratios below $120 M_{\odot}/L_{\odot}$ and a crossing time of the system of $\sim$9 Gyr, we conclude that the system is irregular and not virialised.

From a revised Fundamental Plane based on the proposed structure, we obtain a distance ratio between the Leo I group and the Coma cluster. We find a weighted distance of $D_{\mathrm{Coma}} = (99 \pm 2\,(\mathrm{stat}) \pm 3\,(\mathrm{sys}))$ Mpc. From simulations on the reconstruction of the low-redshift Universe, we obtain the peculiar velocity of the Coma cluster. This is used to correct the observed radial velocity of the cluster, resulting in $v_{\mathrm{Coma}} = (7190 \pm 160)$ kms^{-1} (CARRICKS) and $v_{\mathrm{Coma}} = (7050 \pm 300)$ kms^{-1} (BORG). This, respectively, yield an estimate of $H_0 = (74 \pm 2\,(\mathrm{stat}) \pm 3\,(\mathrm{sys}))$ kms^{-1}Mpc^{-1} (CARRICKS) and $H_0 = (72 \pm 3\,(\mathrm{stat}) \pm 3\,(\mathrm{sys}))$ kms^{-1}Mpc^{-1} (BORG), which is in good agreement with the recent type Ia supernovae and Cepheid-based estimate of $H_0 = (73.2 \pm 1.3)$ kms^{-1}Mpc^{-1} (Riess et al., 2021).

7 Acknowledgements

I would like to thank my supervisor Jens Hjorth for a great collaboration and always being there to answer my questions. Thank you to Radoslaw Wojtak for sharing his insight, always being available for discussions and providing me access to the simulations. Thank you to Adriano Agnello for the many discussions and help on statistical questions. Thank you to Cecilie Cold and Doogesh Kodi Ramanah for reading through the thesis.

References

Bahcall J. N., Tremaine S., 1981, ApJ, 244, 805

Barlow R. J., 1989, Statistics: A Guide to the Use of Statistical Methods in the Physical Sciences (Manchester Physics Series), reprint edn. WileyBlackwell

Blakeslee J. P., et al., 2010, ApJ, 724, 657

Buchner J., 2021, The Journal of Open Source Software, 6, 3001

Cappellari M., et al., 2006, MNRAS, 366, 1126

Cappellaro E., et al., 2001, The Astrophysical Journal, 549, L215

Carrick J., Turnbull S. J., Lavaux G., Hudson M. J., 2015, MNRAS, 450, 317

Carroll B. W., Ostlie D. A., 2007, An Introduction to Modern Astrophysics, 2nd (international) edn

Clubb K. I., 2008, pp L1–L334

D'Onofrio M., Cariddi S., Chiosi C., Chiosi E., Marziani P., 2017, ApJ, 838, 163

Danby J. M. A., 1988, Fundamentals of celestial mechanics

Djorgovski S., Davis M., 1987, ApJ, 313, 59

Ferrarese L., et al., 2000, ApJ, 529, 745

Fixsen D. J., Cheng E. S., Gales J. M., Mather J. C., Shafer R. A., Wright E. L., 1996, ApJ, 473, 576

Garner R., 2017, Observatory - instruments, https://www.nasa.gov/content/goddard/hubble-space-telescope-science-instruments

Gibson B. K., et al., 2000, ApJ, 529, 723

Girardi M., Manzato P., Mezzetti M., Giuricin G., Limboz F., 2002, ApJ, 569, 720

Graham J. A., et al., 1997, ApJ, 477, 535

Gregg M. D., Ferguson H. C., Minniti D., Tanvir N., Catchpole R., 2004, AJ, 127, 1441

Harris W. E., Harris G. L. H., Layden A. C., Stetson P. B., 2007a, AJ, 134, 43

Harris W. E., Harris G. L. H., Layden A. C., Wehner E. M. H., 2007b, ApJ, 666, 903

Heisler J., Tremaine S., Bahcall J. N., 1985, ApJ, 298, 8

Hernandez M., et al., 2000, MNRAS, 319, 223

Hjorth J., Tanvir N. R., 1997, ApJ, 482, 68

Hjorth J., et al., 2017, ApJ, 848, L31

Hradecky V., Jones C., Donnelly R. H., Djorgovski S. G., Gal R. R., Odewahn S. C., 2000, ApJ, 543, 521

Hudson M. J., Lucey J. R., Smith R. J., Schlegel D. J., Davies R. L., 2001, MNRAS, 327, 265

Jacoby G. H., et al., 1992, PASP, 104, 599

Jang I. S., Lee M. G., 2017, ApJ, 836, 74

Jasche J., Lavaux G., 2019, A&A, 625, A64

Jensen J. B., Tonry J. L., Barris B. J., Thompson R. I., Liu M. C., Rieke M. J., Ajhar E. A., Blakeslee J. P., 2003, ApJ, 583, 712

Jha S., et al., 1999, ApJS, 125, 73

Jorgensen I., Franx M., Kjaergaard P., 1996, MNRAS, 280, 167

Kanbur S. M., Ngeow C., Nikolaev S., Tanvir N. R., Hendry M. A., 2003, A&A, 411, 361

Karachentsev I. D., Karachentseva V. E., 2004, Astronomy Reports, 48, 267

Kubo J. M., Stebbins A., Annis J., Dell'Antonio I. P., Lin H., Khiabanian H., Frieman J. A., 2007, ApJ, 671, 1466

Kumar K., 2020, Dynamics and structure of the Leo I group, Bachelor's thesis, University of Copenhagen

Lavaux G., Hudson M. J., 2011, MNRAS, 416, 2840

Lee M. G., Jang I. S., 2013, ApJ, 773, 13

Lee M. G., Jang I. S., 2016, ApJ, 822, 70

Mandel K. S., Narayan G., Kirshner R. P., 2011, ApJ, 731, 120

Michel-Dansac L., et al., 2010, ApJ, 717, L143

Mould J., Sakai S., 2009, ApJ, 694, 1331

Murray C. D., Correia A. C. M., 2011, Keplerian Orbits and Dynamics of Exoplanets (arXiv:1009.1738)

Ohta Y., Taruya A., Suto Y., 2005, ApJ, 622, 1118

Oosterloo T., et al., 2010, MNRAS, 409, 500

Paturel G., Theureau G., Fouqué P., Terry J. N., Musella I., Ekholm T., 2002a, A&A, 383, 398

Paturel G., Teerikorpi P., Theureau G., Fouqué P., Musella I., Terry J. N., 2002b, A&A, 389, 19

Planck Collaboration et al., 2020, A&A, 641, A6

Powell R., 2003, An Atlas of The Universe (accessed on April 30 2022), http://www.atlasoftheuniverse.com/index.html

Riess A. G., Casertano S., Yuan W., Bowers J. B., Macri L., Zinn J. C., Scolnic D., 2021, ApJ, 908, L6

Rizzi L., Tully R. B., Makarov D., Makarova L., Dolphin A. E., Sakai S., Shaya E. J., 2007, ApJ, 661, 815

Sabbi E., Calzetti D., Ubeda L., Adamo A., Cignoni M., Thilker D., Aloisi A., 2018, ApJS, 235, 23

Saha A., Thim F., Tammann G. A., Reindl B., Sandage A., 2006, ApJS, 165, 108

Sakai S., Madore B. F., Freedman W. L., Lauer T. R., Ajhar E. A., Baum W. A., 1997, ApJ, 478, 49

Sakai S., Ferrarese L., Kennicutt Robert C. J., Saha A., 2004, ApJ, 608, 42

Schneider S., 1985, ApJ, 288, L33

Schneider S., 2021, Private communication

Schneider S. E., Helou G., Salpeter E. E., Terzian Y., 1983, ApJ, 273, L1

Sparke L. S., Gallagher John S. I., 2007, Galaxies in the Universe: An Introduction

Stierwalt S., Haynes M. P., Giovanelli R., Kent B. R., Martin A. M., Saintonge A., Karachentsev I. D., Karachentseva V. E., 2009, AJ, 138, 338

Sylvain G. Korzennik A. R. C., 1997, AFOE observations of 51 Pegasi, https://www.cfa.harvard.edu/afoe/51Peg.html

Tanvir N. R., Ferguson H. C., Shanks T., 1999, MNRAS, 310, 175

Tonry J. L., Dressler A., Blakeslee J. P., Ajhar E. A., Fletcher A. B., Luppino G. A., Metzger M. R., Moore C. B., 2001, ApJ, 546, 681

Voit G. M., 2005, Reviews of Modern Physics, 77, 207

Watkins A. E., Mihos J. C., Harding P., Feldmeier J. J., 2014, The Astrophysical Journal, 791, 38

Wegner G., Colless M., Saglia R. P., McMahan R. K., Davies R. L., Burstein D., Baggley G., 1999, MNRAS, 305, 259

Wright J. T., 2018, Handbook of Exoplanets, p. 619–631

de Vaucouleurs G., de Vaucouleurs A., Corwin Herold G. J., Buta R. J., Paturel G., Fouque P., 1991, Third Reference Catalogue of Bright Galaxies

Appendices

A Comparison between the derived model for v_{los} and previous solutions

The results from the Keplerian fit presented in S85 are shown in Figure 35. The table shows the resulting orbital parameters from two models (kinematic and geometric).

PARAMETERS OF ORBIT MODELS

Parameter	Kinematic	Geometric
Eccentricity	0.41 ± 0.03	0.29 ± 0.05
PA of ascending node (deg)	219 ± 3	210 ± 7
PA of periapse (deg)	218 ± 6	203 ± 10
Inclination (deg)	47 ± 5[a]	50 ± 5
Heliocentric velocity of focus (km s^{-1})	829 ± 3	841 ± 13
Orbital velocity at periapse (km s^{-1})	256 ± 19	
Semi-major axis (kpc)	104 ± 7	
Mass ($M_\odot$)	$6.4 \pm 1.1 \times 10^{11}$	
Period (yr)	$3.9 \pm 0.3 \times 10^{9}$	

[a] Based on observed vs. predicted eccentricities only.

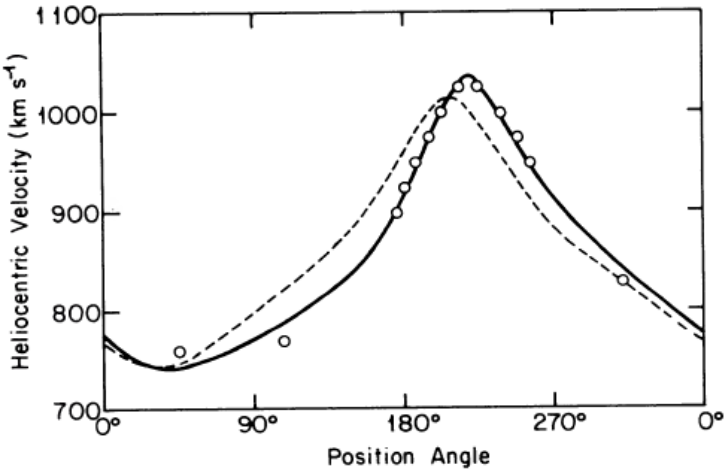

Figure 35: **Top:** Table 2 from S85 with parameters of orbit models. **Bottom:** Figure 2 from S85, shows the fitted Keplerian models to the line-of-sight velocities of the intergalactic ring. The solid line is the kinematic fit to the observed velocities, and the dashed line is a geometric fit. Position angles are reference to the center of the ellipse shown in the right panel of Figure 3. Note, the position angle (eccentric anomaly) is shifted 180° relative to the periapse.

In this section, we explain the method used in S85 and compare it to the derived model in eq. (69). The methods used in S85 is described in chapter 4 of the associated dissertation (Schneider, 2021, private communication).

In the plane of orbit, the position along the orbit can be expressed in the (x, y, z) coordinate-system in terms of the eccentric anomaly as:

$$x = a\cos(E)$$
$$y = a\sqrt{1-e^2}\sin(E)$$

S85 then writes out the projection of the velocity vector onto the x- and y-axes in terms of the true anomaly, and the radial and azimuthal velocities:

$$v_x = v_r\cos(\theta) - v_\theta\sin(\theta)$$
$$v_y = v_r\sin(\theta) + v_\theta\cos(\theta).$$

By expressing v_x and v_y in terms of E, the line of sight velocity can be obtained by projecting the total velocity onto the line of sight. However, the derived and fitted model in S85 is expressed as (Schneider, 2021):

$$v_{\rm los} = \left[\sqrt{\frac{GM(1-e^2)}{a(1-e^2\sin^2 E_\omega}}\right]\frac{\cos(E-E_\omega)}{1-e\cos E} + v_0, \tag{114}$$

where E_ω is eccentric anomaly of ω and v_0 is the proper motion of the centre of mass. There is a discrepancy between the model derived in this work and the one in eq. (114). S85 adopts the following definition of the radial and azimuthal velocities (Schneider, 2021):

$$v_r = \frac{2A_{\rm orb}e}{a(1-e^2)}\sin(\theta)$$
$$v_\theta = \frac{2A_{\rm orb}e}{r}.$$

Comparing with the derived components in our model from eqs. (34) and (35), we find a similar expression for v_r, whereas the definition of v_θ deviates with a factor of e. As described in the deviation of eq. (69), we can obtain $v^2 = G(m_1+m_2)(2/r - 1/a)$ by simply adding the components $v^2 = \dot{r}^2 + r^2\dot{\theta}^2 = v_r^2 + v_\theta^2$ as shown in eq. (27). Additionally, we showed that the same expression is obtained from energy conservation as shown in

eq. (43). We therefore conclude, that there is a fundamental difference in the definition of v_θ, which propagates and causes the discrepancy in the resulting models. Since we find the two models incomparable, we refrain from comparing the results from fitting the line-of-sight velocities.

B UltraNest

The ULTRANEST implementation of nested sampling can be summarised in 4 key points (Buchner, 2021):

1. **Constrained-likelihood sampling alogrithm**
   For sampling a new independent point, an ellipsoid is placed around each live point (sampled point) and the new point is then drawn from this ellipsoid. Its shape is determined from the live point distribution (Mahalanobis distance) and its size from cross-validation Buchner (2021).

2. **Nested sampler**
   A tool which manages the live point population. This component of the algorithm is able to add or remove points and applies several strategies to inject more points when needed to populated clusters. It is also used to reach an effective sample size, integration uncertainty or posterior accuracy.

3. **Nested integrator**
   A component that assigns weights to each sampled point. Via a bootstrapping scheme, it simulates other runs with fewer live points. It is used to give robust and realistic uncertainties.

4. **Termination criterion**
   A criterion must be set to terminate the sampling. You could terminate when the removed points have more weight that the live points. However, for flat likelihoods with very small peaks this is not suitable. Instead, UltraNest integrates until the live point weights are insignificant.

A typical run would initially draw points from the entire parameter space according to the prior. The lowest live points corresponding to the worst fit are then removed and the step is repeated until a better point is found. For each removal, the volume sampled is decreased by a constant factor. Next, the constrained-likelihood sampling algorithm is applied, i.e. placing ellipsoids around each live point. The nested sampling algorithm then proceeds to the peak and keeps track of the likelihood. Since the volume becomes smaller and smaller, we reach a point at which the remainder does not contribute any probability mass and the exploration is then finished. The posterior samples are then computed by weighing the removed points by their likelihood and the volume they represent.

C Nested Sampling: Alternative solutions

Option A: Same bounds

We have run the same procedure as described in Section 2.4 with $n = 10000$ live points. The results from nested sampling is shown in Figure 36 and 37.

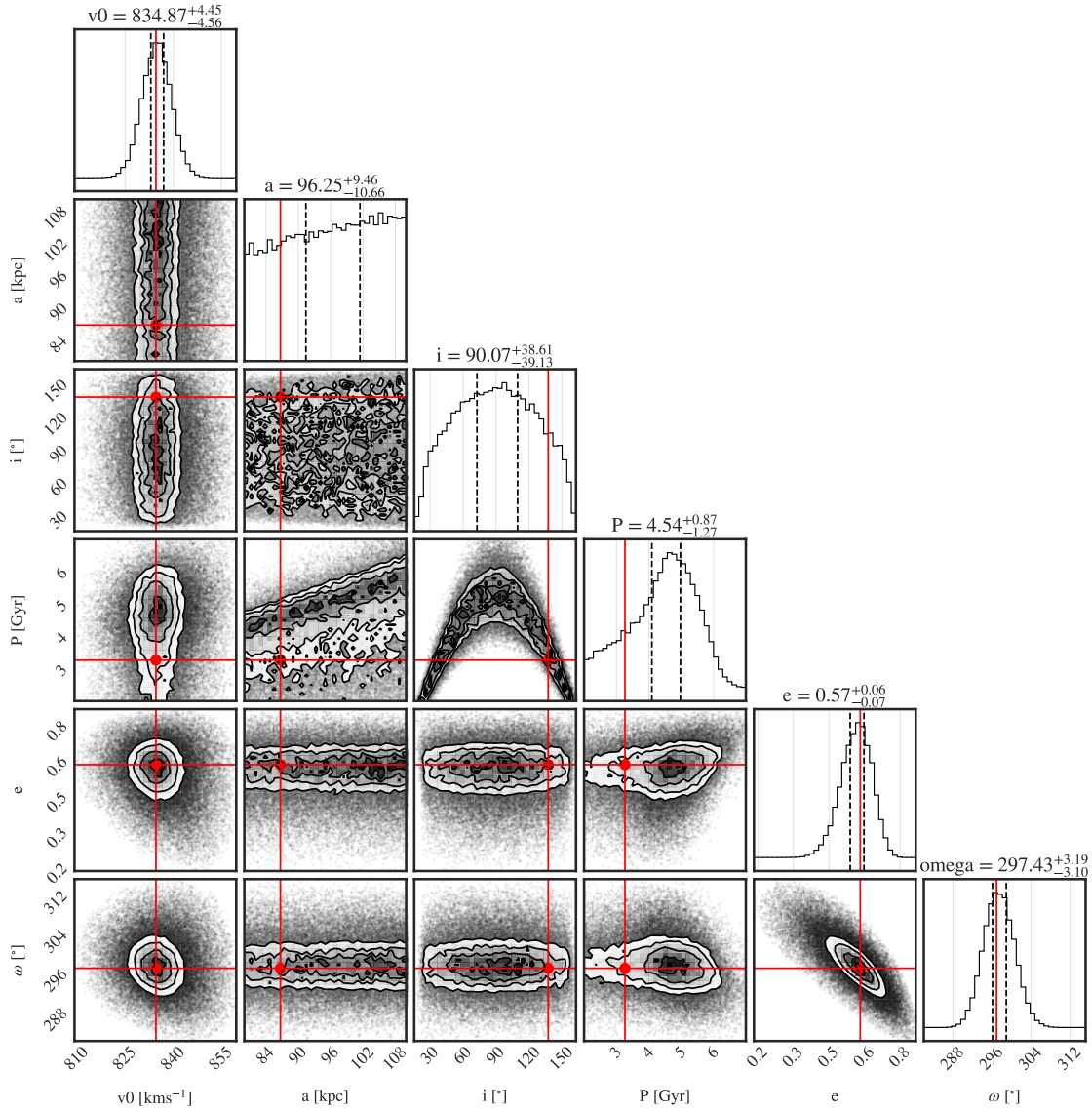

Figure 36: Corner plot of the parameter space explored via nested sampling. Titles of each histogram shows the median value of the distribution with estimated upper and lower uncertainty. Black dashed lines on the distributions show the 1σ interval from the median. Red lines/dots indicate the maximum likelihood best fit parameters from Table 3. 35 bins is used for each histogram. The contours show the 2D sigma level. Within the 1-sigma level of 1D distributions, the Gaussian contains 39.3% of the volume.

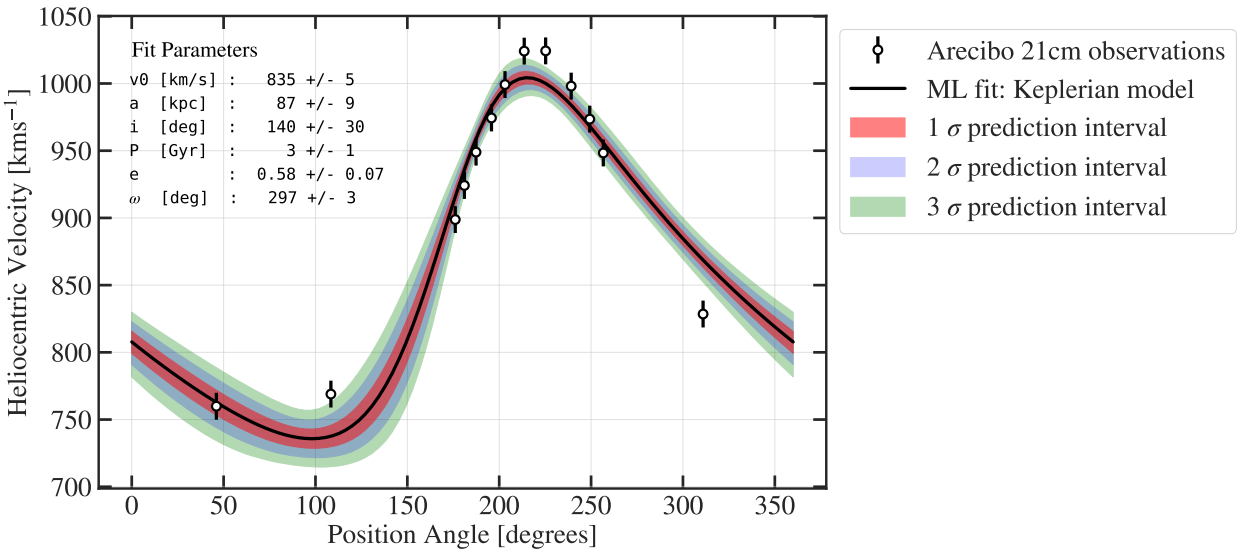

Figure 37: Keplerian model of the line-of-sight velocities for the intergalactic gas ring. The heliocentric velocity of clouds II-VII in km/s is plotted versus the position angle (eccentric anomaly) relative to the center of the proposed ellipse. The solid black line shows the fit with the maximum likelihood best fit parameters. These are noted in the figure. The red, blue and green coloured regions show the 1, 2 and 3σ region from the maximum likelihood. Note that the position angle (eccentric anomaly) is shifted 180° relative to the periapse.

Option B: Alternative prior

We have run the same procedure as described in Section 2.4 with $n = 10000$ live points. However, we use a prior with looser bounds as shown in Table 14, where the bounds on M is unaccounted for.

Table 14: Flat prior used in nested sampling

Parameter	Lower Bound	Upper Bound
v_0 [km/s]	200	2000
a [kpc]	50	180
i [degrees]	0	180
P [Gyr]	0.8	10
e	0	<1
ω [degrees]	0	360

The results from nested sampling using the prior in Table 14 is shown in Figure 38 and 39.

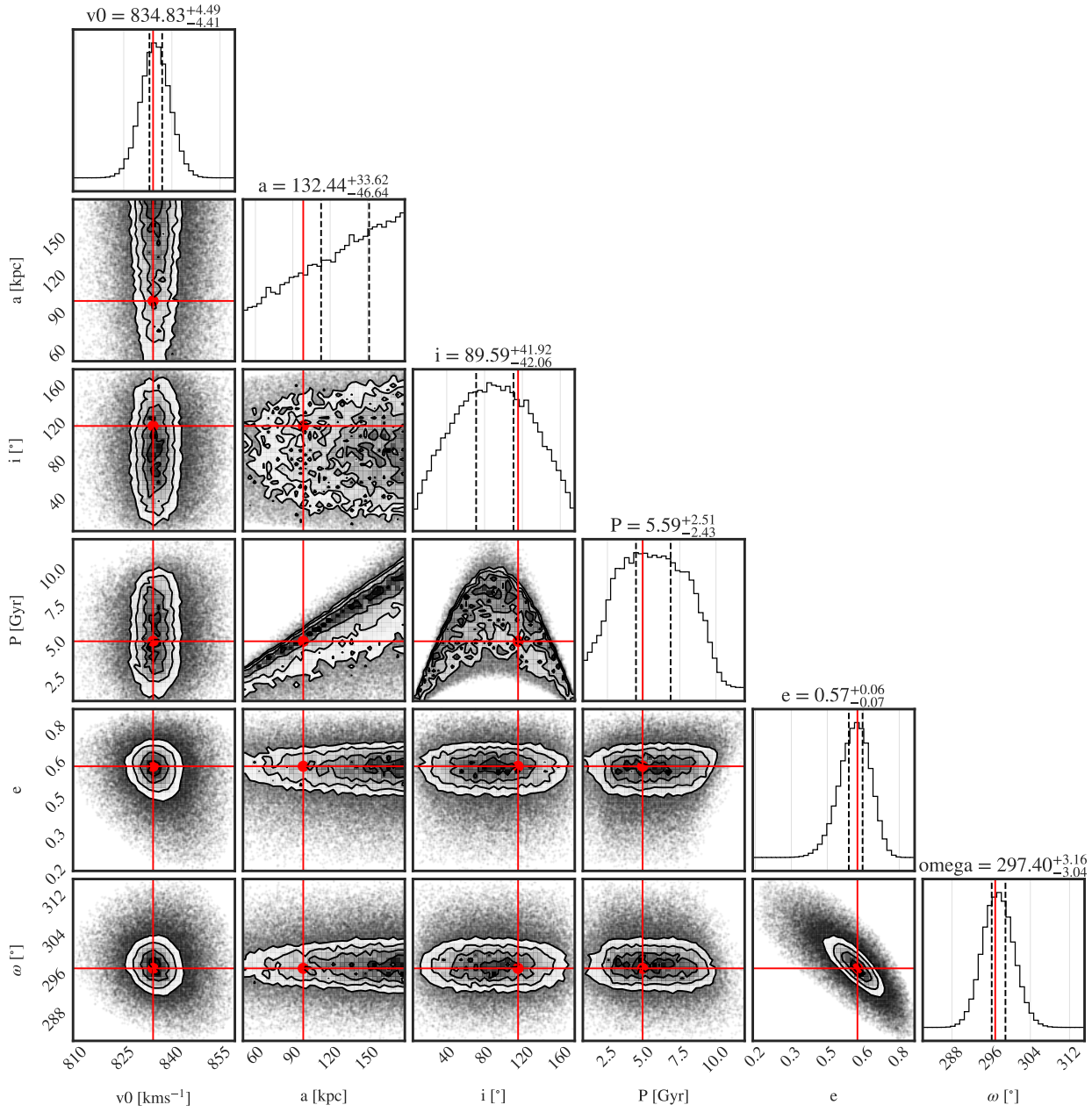

Figure 38: Corner plot of the parameter space explored via nested sampling. Titles of each histogram shows the median value of the distribution with estimated upper and lower uncertainty. Black dashed lines on the distributions show the 1σ interval from the median. Red lines/dots indicate the maximum likelihood best fit parameters from Table 3. 35 bins is used for each histogram. The contours show the 2D sigma level. Within the 1-sigma level of 1D distributions, the Gaussian contains 39.3% of the volume.

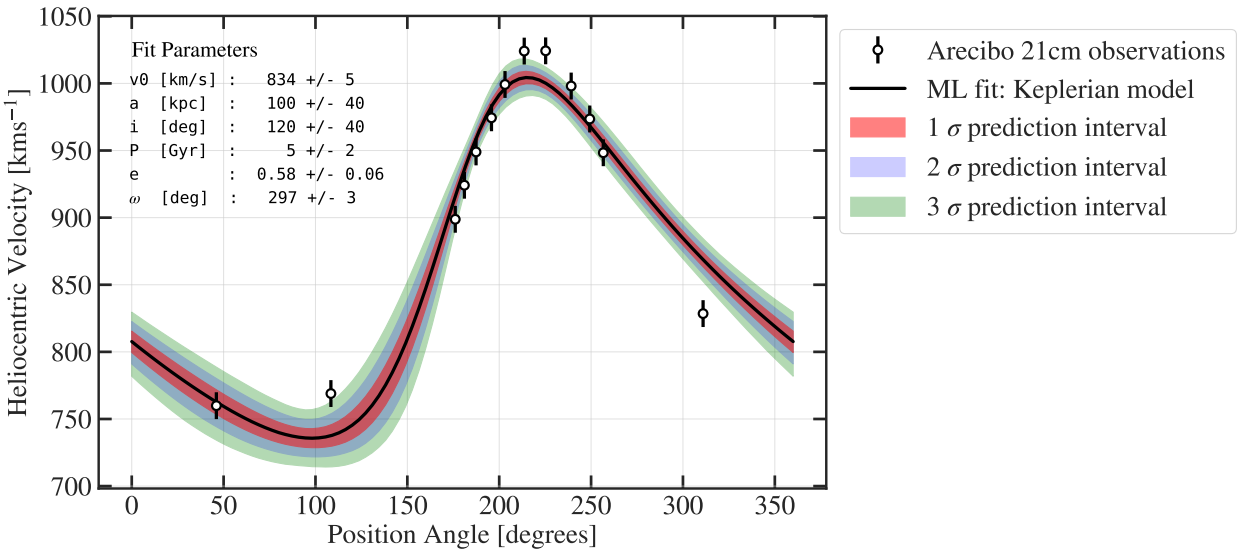

Figure 39: Keplerian model of the line-of-sight velocities for the intergalactic gas ring. The heliocentric velocity of clouds II-VII in km/s is plotted versus the position angle (eccentric anomaly) relative to the center of the proposed ellipse. The solid black line shows the fit with the maximum likelihood best fit parameters. These are noted in the figure. The red, blue and green coloured regions show the 1, 2 and 3σ region from the maximum likelihood. Note that the position angle (eccentric anomaly) is shifted 180° relative to the periapse.

D Notes on Cepheids

Classes of pulsating stars

As briefly mentioned, there exist several types of Cepheids. Although, we are concerned with the Classical Cepheids as we make use of its period-luminosity relation, it is meaningful to position it on the H-R diagram and compare with other classes. In the Milky Way alone, we estimate up to millions of pulsating stars, whereas there are hundred billions of stars in the galaxy. This by it self tells us, that pulsating stars are a transient phenomenon. It is best represented by positioning it on the H-R diagram as in Figure 40.

It turns out, that the majority of pulsating stars lie along an almost vertical narrow band (600-1000 K wide), which is called the *instability strip* (Carroll & Ostlie, 2007). This is indicated by the shaded areas on the Figure. Figure 40 shows different evolutionary tracks for stars of different masses. As they enter the strip the begin to pulsate and shortly after, when leaving this phase, the oscillations stop.

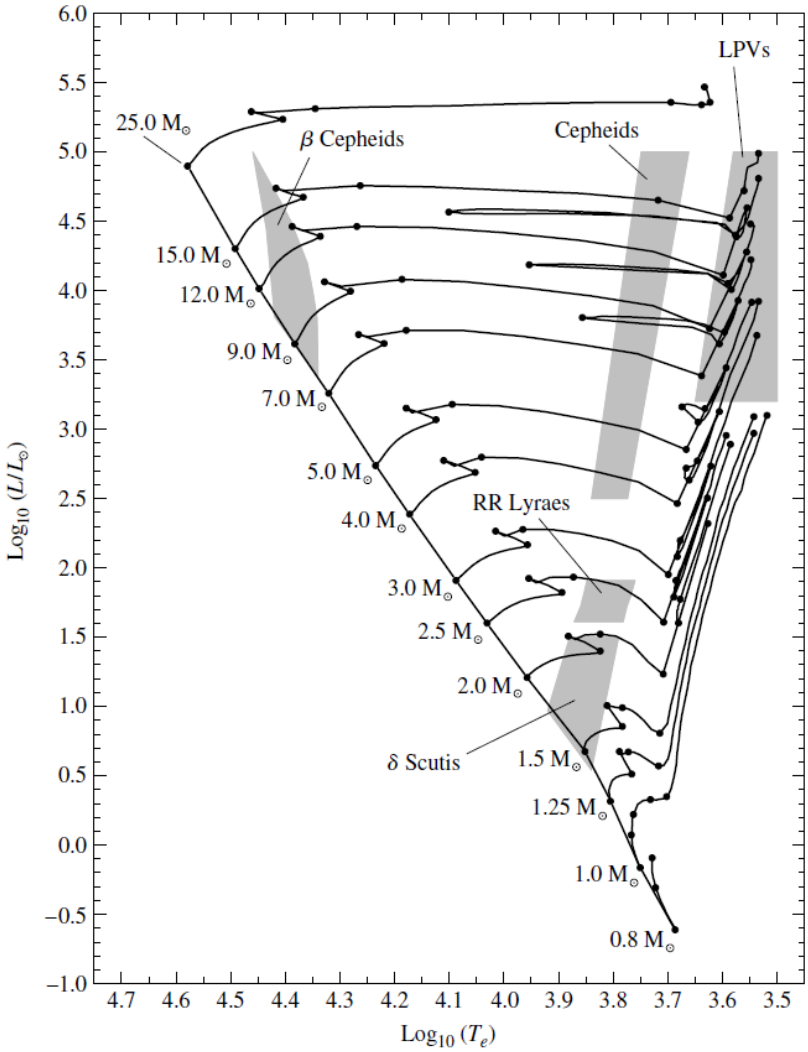

Figure 40: Figure 14.8 from (Carroll & Ostlie, 2007). Pulsating stars on the H-R diagram. The shaded areas mark the instability strip.

On the diagram, we find the *Long-Period Variables* (LPVs), *Classical Cepheids*, *RR Lyrae stars*, *δ Scutis* and *β Cepheids*. These types of Cepheids all have different ranges of pulsation periods, masses and population types. Some, like the β cephei stars can even exhibit both radial or non-radial oscillations. Additionally, all the Cepheids within the instability strip have common mechanisms which drives the oscillations, whereas the LPVs or β Cepheids differ as the element driving the mechanisms are iron.

The physics of stellar pulsation

The radial oscillations of a pulsating star is the result of sound waves resonating within the star. The pulsation period denoted, Π, is easily obtained by computing the time

needed for the sound wave to cross the diameter of the star with constant density ρ. The adiabatic sound speed is given by:

$$v_s = \sqrt{\frac{\gamma P}{\gamma}}, \tag{115}$$

where P is the pressure and γ the adiabatic index. One caveat with this method is of course the assumption of constant density, since this is quite unrealistic (Carroll & Ostlie, 2007). However, from hydrostatic equilibrium we find the pressure:

$$\frac{\mathrm{d}P}{\mathrm{d}r} = -\frac{GM_r\rho}{r^2} = \frac{G(\frac{4}{3}\pi r^3\rho)\rho}{r^2} = \frac{4}{3}\pi G\rho^2 r. \tag{116}$$

This is then integrated to find the pressure as a function of r, using the boundary condition $P = 0$ at the surface:

$$P(r) = \frac{2}{3}\pi G\rho^2(R^2 - r^2), \tag{117}$$

where R is the radius of the star. The time is equal to the diameter divided by the adiabatic sound speed, but as the latter depends on the pressure, we must integrate over the full length:

$$\Pi \approx 2\int_0^R \frac{\mathrm{d}r}{v_s} \approx 2\int_0^R \frac{\mathrm{d}r}{\sqrt{\frac{2}{3}\gamma\pi G\rho(R^2 - r^2)}}, \tag{118}$$

This may be simplified to:

$$\Pi \approx \sqrt{\frac{3\pi}{2\gamma G\rho}}. \tag{119}$$

While this expression is a rough estimation of the pulsation period, it shows how the pulsation period is inversely proportional to the square root of the mean density. This helps explaining the period-luminosity relation, since we see the pulsation period decreases as we move down the instability strip on Figure 40.

To understand the mechanism that drives the oscillation, we must consider Kramer's law:

$$\kappa \propto \frac{\rho}{T^{3.5}}. \tag{120}$$

where κ is the opacity and T the temperature. As explained from Eddington's valve

mechanism, the opacity must increase during compression. However, given the stronger dependency on temperature in Kramer's law, the opposite is the case. However, in partially ionization zones this is actually the case. In these zones, the gas produces further ionization which results in a rise in temperature, which is smaller than the increase in density, thus increasing the opacity. Similarly, during expansion, the temperature drops, but not as significantly as expected, since energy is now released from recombination. The density term therefore dominates again and the opacity drops. This leads to energy pushing the surface layers upward during expansion, at which point the star becomes more transparent and is able to radiate energy away before contracting, which increases the opacity. The cycle then starts over.

E Distance measurements

We tabulate and plot the reduced sample for the Cepheid, TRGB and SBF method as discussed in Section 3.3.1.

Table 15: **Cepheids sample**: $m - M$ shows the distance modulus for each measurement in the final sample. σ_{m-M} is the random uncertainty in the distance modulus. The systematic uncertainty is 0.16 mag for all measurements. **Column 3** shows the distance in Mpc with associated random uncertainty in **Column 4**. **Column 5** and **6** shows the galaxy and publication year, respectively, for each measurement. The source for each measurements are stated in **Column 7**.

$m - M$	σ_{m-M}	D [Mpc]	σ_D [Mpc]	Galaxy	Year	Source
29.902	0.900	10	4	NGC3351	2003	Kanbur et al. (2003)
29.85	0.16	9.3	0.69	NGC3351	2002	Paturel et al. (2002b)
29.88	0.08	9.5	0.35	NGC3351	2002	Paturel et al. (2002a)
30.01	0.08	10.0	0.37	NGC3351	2000	Ferrarese et al. (2000)
30.01	0.19	10.0	0.88	NGC3351	1997	Graham et al. (1997)
30.10	0.07	10.5	0.34	NGC3351	2006	Saha et al. (2006)
30.08	0.17	10.4	0.81	NGC3368	2002	Paturel et al. (2002b)
30.17	0.10	10.8	0.50	NGC3368	2002	Paturel et al. (2002a)
30.25	0.18	11.2	0.93	NGC3368	1999	Tanvir et al. (1999)
30.20	0.10	11.0	0.50	NGC3368	2000	Ferrarese et al. (2000)
30.20	0.10	11.0	0.50	NGC3368	2000	Gibson et al. (2000)
30.34	0.11	11.7	0.59	NGC3368	2006	Saha et al. (2006)

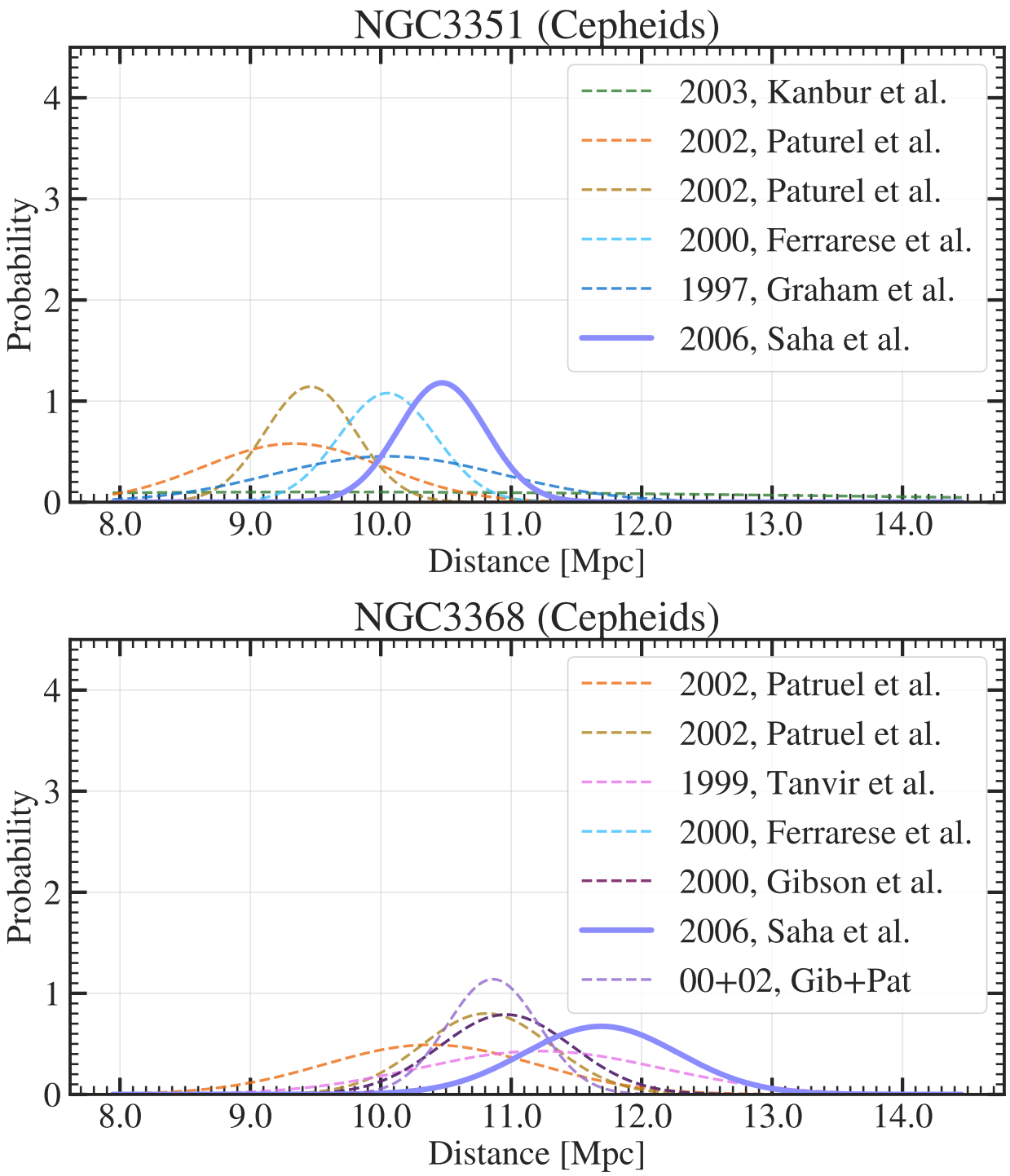

Figure 41: **Cepheids sample**: Measurements from Table 15 for NGC 3351 and NGC 3368. The source is stated shown in the legend. The highlighted solid curve indicates the measurement used for the structural analysis.

Table 16: **Tip of the Red Giant Branch sample**: $m - M$ shows the distance modulus for each measurement in the final sample. σ_{m-M} is the random uncertainty in the distance modulus. The systematic uncertainty is 0.12 mag for all measurements. **Column 3** shows the distance in Mpc with associated random uncertainty in **Column 4**. **Column 5** and **6** shows the galaxy and publication year3 respectively, for each measurement. The source for each measurements are stated in **Column 7**.

$m - M$	σ_{m-M}	D [Mpc]	σ_D [Mpc]	Galaxy	Year	Source
29.840	0.400	9.3	1.7	NGC3351	2018	Sabbi et al. (2018)
29.920	0.050	9.6	0.22	NGC3351	2007	Rizzi et al. (2007)
30.390	0.130	12.00	0.72	NGC3351	2004	Sakai et al. (2004)
29.960	0.560	9.8	2.5	NGC3368	2018	Sabbi et al. (2018)
30.223	0.054	11.1	0.3	NGC3368	2017	Jang & Lee (2017)
30.150	0.030	10.70	0.15	NGC3368	2013	Lee & Jang (2013)
29.650	0.200	8.5	0.78	NGC3368	2009	Mould & Sakai (2009)
30.180	0.020	10.9	0.1	NGC3377	2016	Lee & Jang (2016)
30.590	0.060	13.1	0.36	NGC3377	2009	Mould & Sakai (2009)
30.180	0.160	10.9	0.8	NGC3377	2007	Harris et al. (2007a)
30.050	0.020	10.200	0.094	NGC3379	2016	Lee & Jang (2016)
30.100	0.160	10.50	0.77	NGC3379	2007	Harris et al. (2007b)
30.140	0.140	10.7	0.69	NGC3379	2004	Gregg et al. (2004)
30.300	0.140	11.5	0.74	NGC3379	1997	Sakai et al. (1997)
30.420	0.100	12.10	0.56	NGC3384	2009	Mould & Sakai (2009)

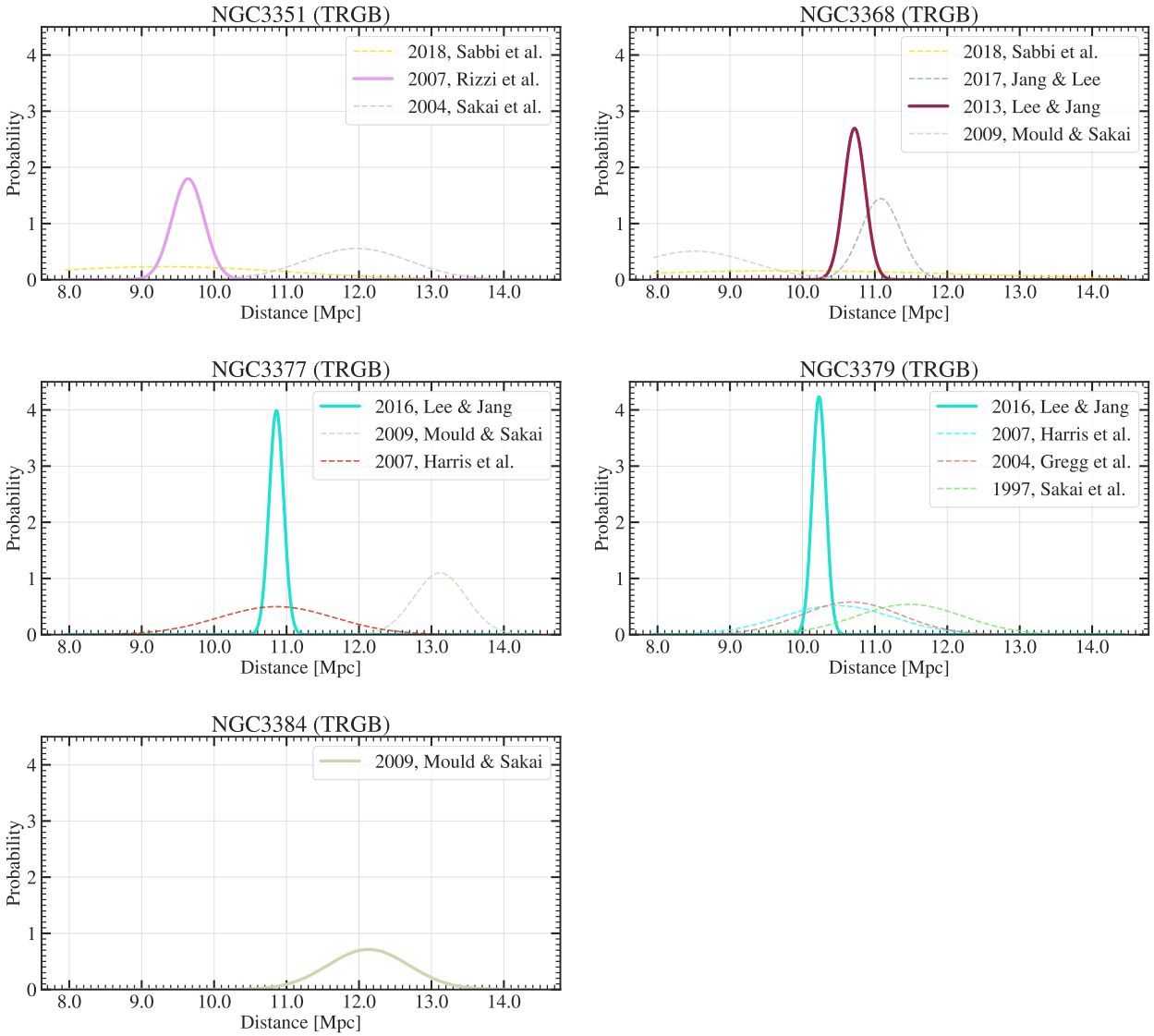

Figure 42: **Tip of the Red Giant Branch sample**: Measurements from Table 16 for each galaxy in the TRGB sample. The source is stated shown in the legend. The highlighted solid curve indicates the measurement used for the structural analysis.

Table 17: **Surface Brightness Fluctuations sample**: $m - M$ shows the distance modulus for each measurement in the final sample. σ_{m-M} is the random uncertainty in the distance modulus. The systematic uncertainty is 0.16 mag for all measurements. **Column 3** shows the distance in Mpc with associated random uncertainty in **Column 4**. **Column 5** and **6** shows the galaxy and publication year, respectively, for each measurement. The source for each measurements are stated in **Column 7**.

$m - M$	σ_{m-M}	D [Mpc]	σ_D [Mpc]	Galaxy	Year	Source
30.02	0.22	10.09	1.02	NGC3368	2003	Jensen et al. (2003)
30.13	0.22	10.61	1.08	NGC3368	2001	Tonry et al. (2001)
30.21	0.09	11.00	0.46	NGC3377	2001	Tonry et al. (2001)
30.12	0.12	10.57	0.58	NGC3377	2000	Ferrarese et al. (2000)
30.06	0.11	10.28	0.52	NGC3379	2003	Jensen et al. (2003)
30.15	0.11	10.71	0.54	NGC3379	2001	Tonry et al. (2001)
30.18	0.14	10.86	0.70	NGC3379	2000	Ferrarese et al. (2000)
30.26	0.14	11.27	0.73	NGC3384	2003	Jensen et al. (2003)
30.30	0.14	11.50	0.74	NGC3384	2001	Tonry et al. (2001)
30.38	0.16	11.91	0.88	NGC3384	2000	Ferrarese et al. (2000)
30.28	0.14	11.38	0.73	NGC3412	2001	Tonry et al. (2001)
30.39	0.15	11.98	0.83	NGC3489	2001	Tonry et al. (2001)

The SBF measurements presented in (Tonry et al., 2001) and (Jensen et al., 2003) have been corrected for bias in (Blakeslee et al., 2010). For (Jensen et al., 2003), distance moduli are increased by $+0.1$ mag uniformly to make them consistent with the correction of (Tonry et al., 2001) and the work of (Blakeslee et al., 2010). The correction of (Tonry et al., 2001) measurements is

$$(m - M)_{\mathrm{T01,cor}} = (m - M)_{\mathrm{T01,raw}} + 0.1 - 0.03 Q_{\mathrm{T01}} \tag{121}$$

where Q_{T01} is the observation quality described in (Tonry et al., 2001); higher numbers indicate a better observation (see Table 18). The measurements in Table 17 and 4 are adopts this bias correction.

Table 18: Quality factor, Q, for each member

Galaxy	NGC3368	NGC3379	NGC3377	NGC3384	NGC3412	NGC3489
Q	1.7	2.4	4.8	3.9	3.0	3.9

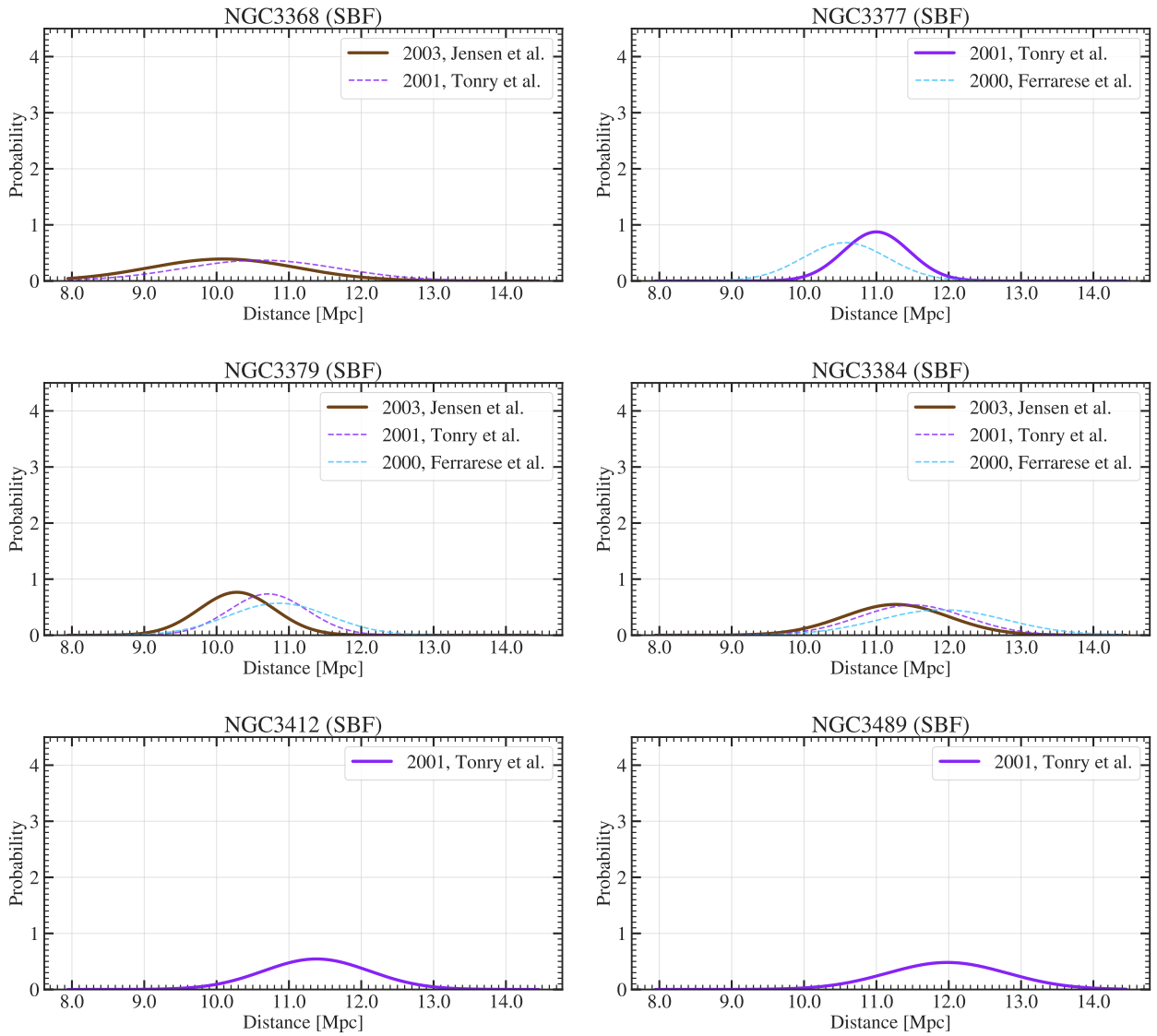

Figure 43: **Surface Brightness Fluctuations sample**: Measurements from Table 17 for each galaxy in the SBF sample. The source is stated shown in the legend. The highlighted solid curve indicates the measurement used for the structural analysis.

F SBF measurements without bias correction

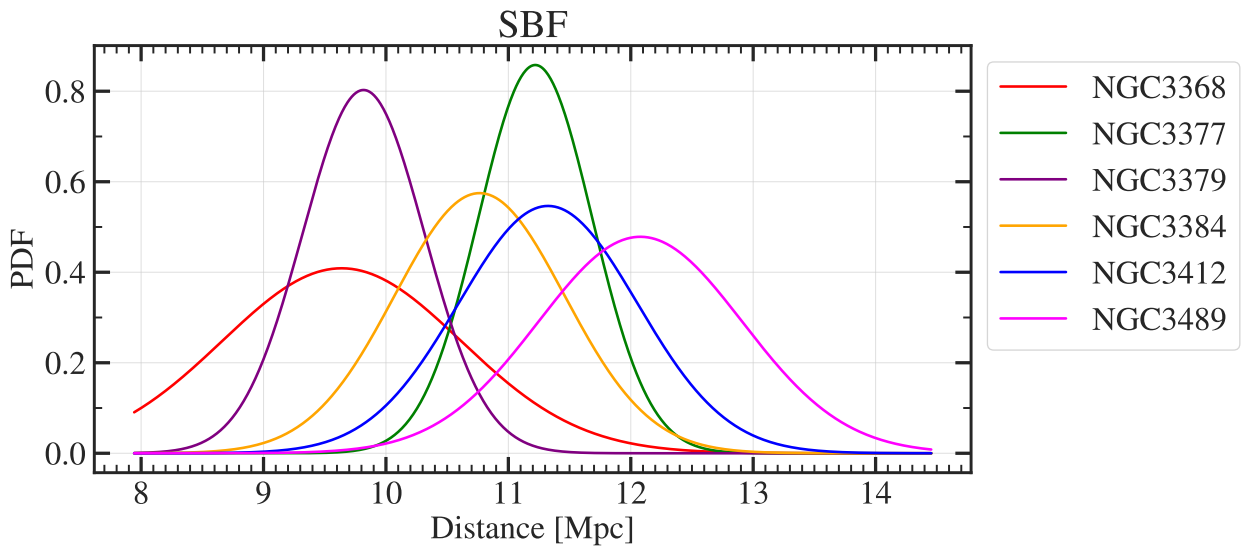

Figure 44: Relative distance comparison. The SBF sample without the bias correction from (Blakeslee et al., 2010) are plotted as Gaussian distributions. The distance is in Mpc. Colors coding indicates the galaxy as shown in the legend.

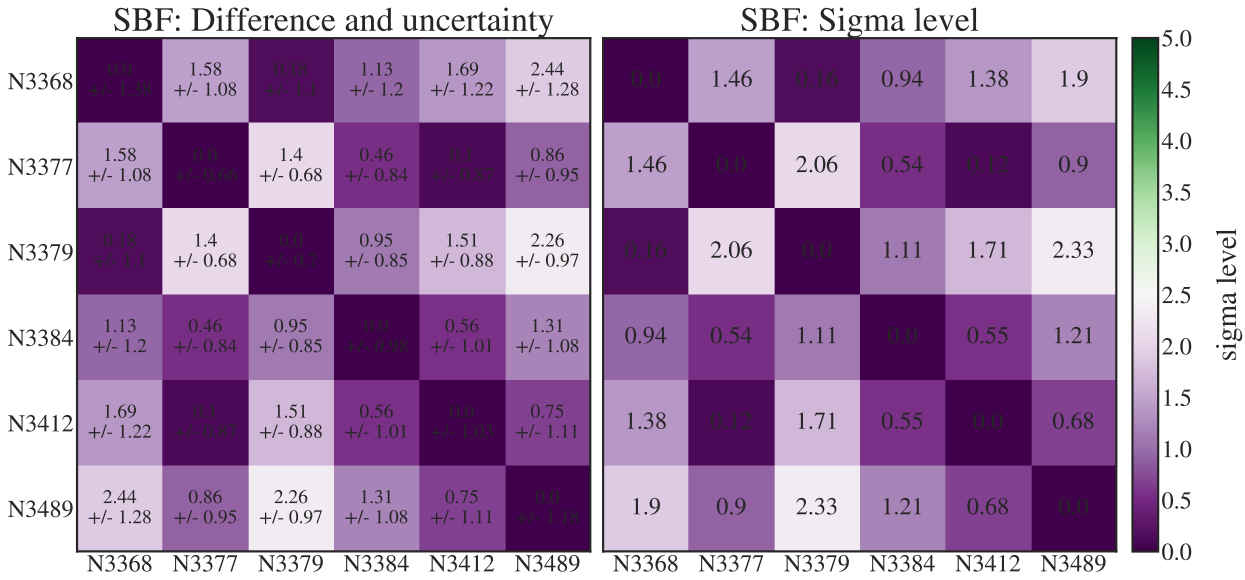

Figure 45: SBF. **Left panel**: Difference and uncertainty between the SBF measurements in Mpc without the bias correction from (Blakeslee et al., 2010). **Right panel**: The sigma level of the difference relative to the uncertainty. The colourbar indicates the sigma level. Galaxy acronyms (NGC) are abbreviated as N.

G Cumulative Mass Function: Total scatter

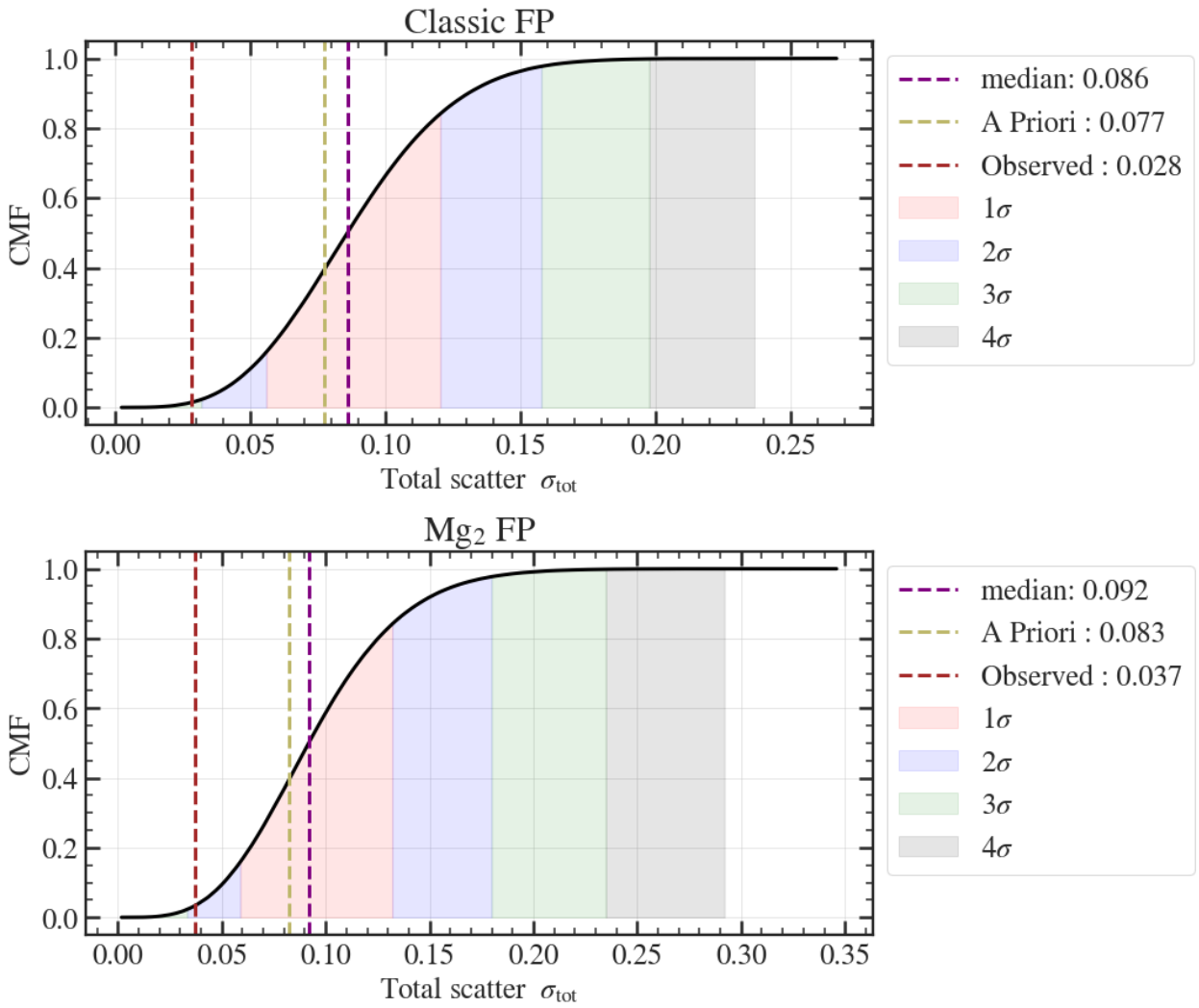

Figure 46: Cumulative Mass Function of the sampled total scatter (σ_{tot}) in dex from the from the classic (top panel) and Mg_2 (bottom panel) FP values as shown in Figure 27. The sample consist of $n = 10^6$ trials. Vertical dashed lines indicate the median, a priori and observed formal rms scatter as indicated in the legend. Shaded areas indicate the 1, 2, 3 and 4σ deviation from the median.

H Fundamental Plane: Obtaining an alternative relation between NGC 3379 and NGC 3377

Using eq. (113), we position NGC 3379 at a distance of 10.86 Mpc corresponding to the position of NGC 3377. We then fit the classic and Mg_2 FP to the galaxies from which we obtain the total scatter for the alternative relation. The shift of NGC 3379 along with the fitted relations are shown in Figure 47.

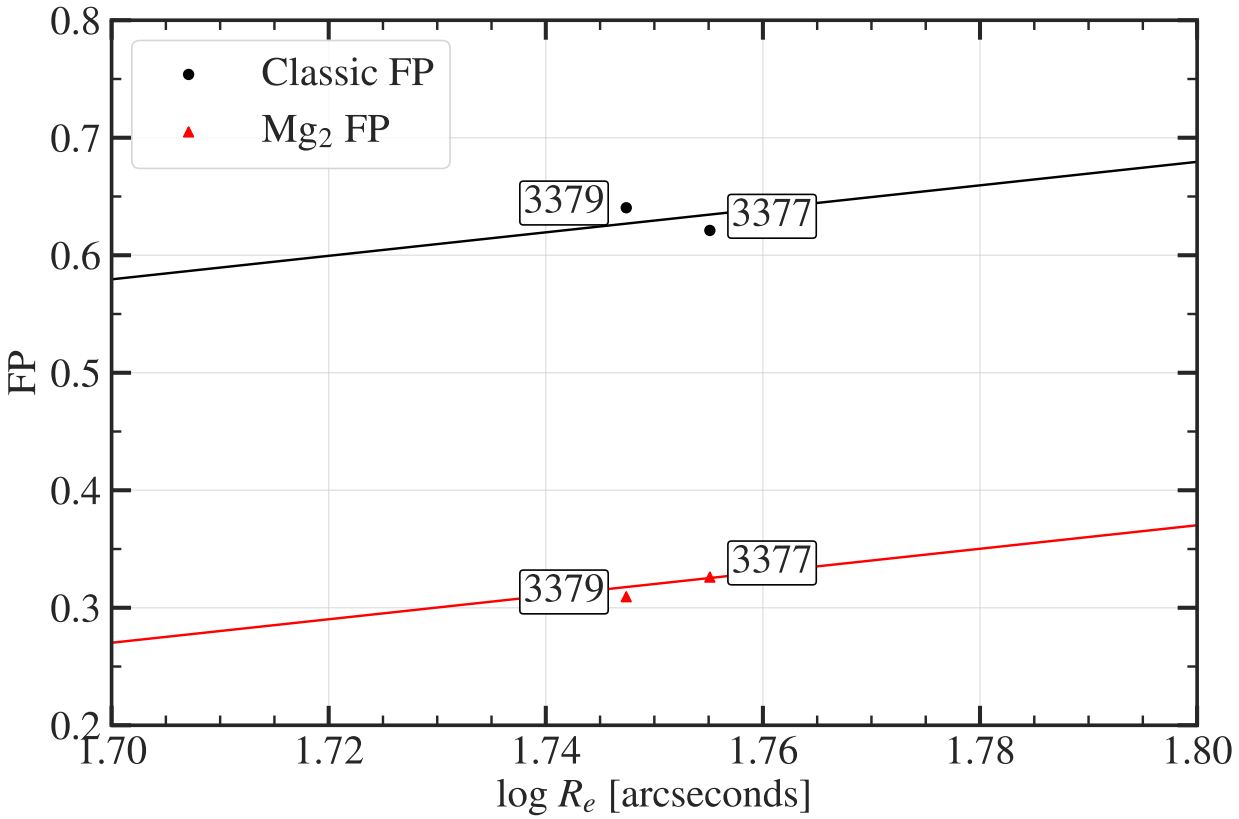

Figure 47: Alternative Fundamental plane in Leo I. The black circles are the classic FP ($FP_{\rm cl} = 1.24\log\sigma - 0.82\log\langle I\rangle_{\rm e}$) values for NGC 3379 and NGC 3377. The red circles are the Mg_2 FP ($FP_{\rm Mg_2} = 1.05\log\sigma - 0.78\log\langle I\rangle_{\rm e} - 0.40\Delta{\rm Mg_2}$) values for NGC 3379 and NGC 3377. The solid lines are fitted FP relations from eq. (104) and (105). NGC 3379 has been shifted upwards on the diagram compared to Figure 27 by adopting a distance of 10.86 Mpc to NGC 3377, the associated zero point of $\gamma_{NGC3377} = 1.134$ and eq. (113).

I Fundamental Plane: zero points and distance ratios

Table 19: **Distance ratios:** Column 1 shows the galaxy used for determining γ. The FP relation rows are based on the fit of NGC 3379, NGC 3377, NGC 3384 and NGC 3412. The NGC 3377 + NGC 3379 rows is from the alternative approach including only these galaxies. The assumption for determining the uncertainty is shown in Column 2, where $\sigma_{\rm int+obs}$ includes both the measurement error and an additional 14% intrinsic error. $\sigma_{\rm obs}$ includes only the measurement error. For $\sigma_{\rm alt}$, both the measurement and intrinsic error is discarded and instead only the scatter between NGC 3379 and NGC 3377 is used. We adopt a Leo I redshift of 757 ± 68 km/s from (Hjorth & Tanvir, 1997). Column 4 and 5 show the angular diameter distance ratio in log and linear scale respectively. Column 6 and 7 show the luminosity distance ratio in log and linear scale respectively.

Classic FP

Galaxy	Assumption	γ	$D_{\rm A}$ ratio (log)	$D_{\rm A}$ ratio	$D_{\rm L}$ ratio (log)	$D_{\rm L}$ ratio
NGC 3377	$\sigma_{\rm int+obs}$	1.134 ± 0.082	0.952 ± 0.082	9.0 ± 1.7	0.97 ± 0.083	9.3 ± 1.8
	$\sigma_{\rm obs}$	1.134 ± 0.055	0.952 ± 0.056	9.0 ± 1.1	0.97 ± 0.056	9.3 ± 1.2
	$\sigma_{\rm alt}$	1.134 ± 0.0135	0.952 ± 0.016	8.95 ± 0.33	0.97 ± 0.016	9.33 ± 0.34
NGC 3379	$\sigma_{\rm int+obs}$	1.133 ± 0.072	0.951 ± 0.073	8.9 ± 1.5	0.969 ± 0.073	9.3 ± 1.6
	$\sigma_{\rm obs}$	1.133 ± 0.038	0.951 ± 0.039	8.93 ± 0.8	0.969 ± 0.039	9.31 ± 0.84
	$\sigma_{\rm alt}$	1.133 ± 0.0135	0.951 ± 0.016	8.93 ± 0.33	0.97 ± 0.016	9.31 ± 0.34
FP relation:	$\sigma_{\rm int+obs}$	1.158 ± 0.022	0.976 ± 0.039	9.46 ± 0.84	0.994 ± 0.039	9.86 ± 0.89
Classic	$\sigma_{\rm obs}$	1.158 ± 0.022	0.976 ± 0.024	9.46 ± 0.52	0.994 ± 0.024	9.86 ± 0.55
NGC 3377 + NGC 3379	$\sigma_{\rm alt}$	1.1205 ± 0.0002	0.94 ± 0.011	8.68 ± 0.23	0.957 ± 0.012	9.06 ± 0.25

Mg_2 FP

Galaxy	Assumption	γ	D_A ratio (log)	D_A ratio	D_L ratio (log)	D_L ratio
NGC 3377	$\sigma_{\rm int+obs}$	1.429 ± 0.077	0.932 ± 0.078	8.5 ± 1.5	0.95 ± 0.078	8.9 ± 1.6
	$\sigma_{\rm obs}$	1.429 ± 0.047	0.932 ± 0.074	8.55 ± 0.94	0.95 ± 0.048	8.91 ± 0.99
	$\sigma_{\rm alt}$	1.429 ± 0.0045	0.932 ± 0.010	8.55 ± 0.2	0.95 ± 0.01	8.91 ± 0.21
NGC 3379	$\sigma_{\rm +obs}$	1.464 ± 0.069	0.967 ± 0.070	9.3 ± 1.5	0.985 ± 0.07	9.7 ± 1.6
	$\sigma_{\rm obs}$	1.464 ± 0.033	0.967 ± 0.034	9.26 ± 0.73	0.985 ± 0.034	9.66 ± 0.76
	$\sigma_{\rm alt}$	1.464 ± 0.0045	0.967 ± 0.010	9.26 ± 0.21	0.985 ± 0.01	9.66 ± 0.22
FP relation:	$\sigma_{\rm int+obs}$	1.459 ± 0.02	0.962 ± 0.037	9.16 ± 0.84	0.98 ± 0.038	9.55 ± 0.84
Mg_2	$\sigma_{\rm obs}$	1.459 ± 0.02	0.962 ± 0.022	9.16 ± 0.46	0.98 ± 0.022	9.55 ± 0.48
NGC 3377 + NGC 3379	$\sigma_{\rm alt}$	1.42979 ± 0.00002	0.933 ± 0.007	8.57 ± 0.14	0.9512 ± 0.0072	8.94 ± 0.15

Table 20: **Distance to Coma:** Column 1 shows the object used for determining the distance. The assumption for determining the uncertainty is shown in Column 2, where $\sigma_{\mathrm{int+obs}}$ includes both the measurement error and an additional 14% intrinsic error. σ_{obs} includes only the measurement error. For σ_{alt}, both the measurement and intrinsic error is discarded and instead only the scatter between NGC 3379 and NGC 3377 is used. The FP classic rows in Column 2 are based on the fit of NGC 3379, NGC 3377, NGC 3384 and NGC 3412. The NGC 3377 + NGC 3379 rows are from the alternative approach including only these galaxies. Column 3,4 and 5 show the distance, random and systematic uncertainty respectively. All distances are in Mpc.

Object	Assumption	D_{Coma} [Mpc]	$\sigma_{D_{\mathrm{Coma}}}$ (random) [Mpc]	$\sigma_{D_{\mathrm{Coma}}}$ (systematic) [Mpc]
NGC 3368	$\sigma_{\mathrm{int+obs}}$	100	20	20
	σ_{obs}	100	10	10
	σ_{alt}	103	5	5
	$\sigma_{\mathrm{int+obs}}$: FP classic	110	10	10
	σ_{obs}: FP classic	109	7	7
	σ_{alt}: NGC 3377 + NGC3379	100	4	4
68-77-grp	$\sigma_{\mathrm{int+obs}}$	100	20	20
	σ_{obs}	100	10	10
	σ_{alt}	101	4	7
	$\sigma_{\mathrm{int+obs}}$: FP classic	107	10	10
	σ_{obs}: FP classic	107	6	8
	σ_{alt}: NGC 3377 + NGC3379	98	3	6
NGC 3379	$\sigma_{\mathrm{int+obs}}$	100	20	20
	σ_{obs}	95	9	10
	σ_{alt}	95	4	6
	$\sigma_{\mathrm{int+obs}}$: FP classic	101	9	10
	σ_{obs}: FP classic	101	6	8
	σ_{alt}: NGC 3377 + NGC3379	93	3	6
SN1998bu	$\sigma_{\mathrm{int+obs}}$	90	20	20
	σ_{obs}	90	10	10
	σ_{alt}	91	3	5
	$\sigma_{\mathrm{int+obs}}$: FP classic	96	9	10
	σ_{obs}: FP classic	96	5	7
	σ_{alt}: NGC 3377 + NGC3379	89	3	5

J Results from CARRICKS model

The density profile of the Coma cluster from the CARRICKS model is shown in Figure 48.

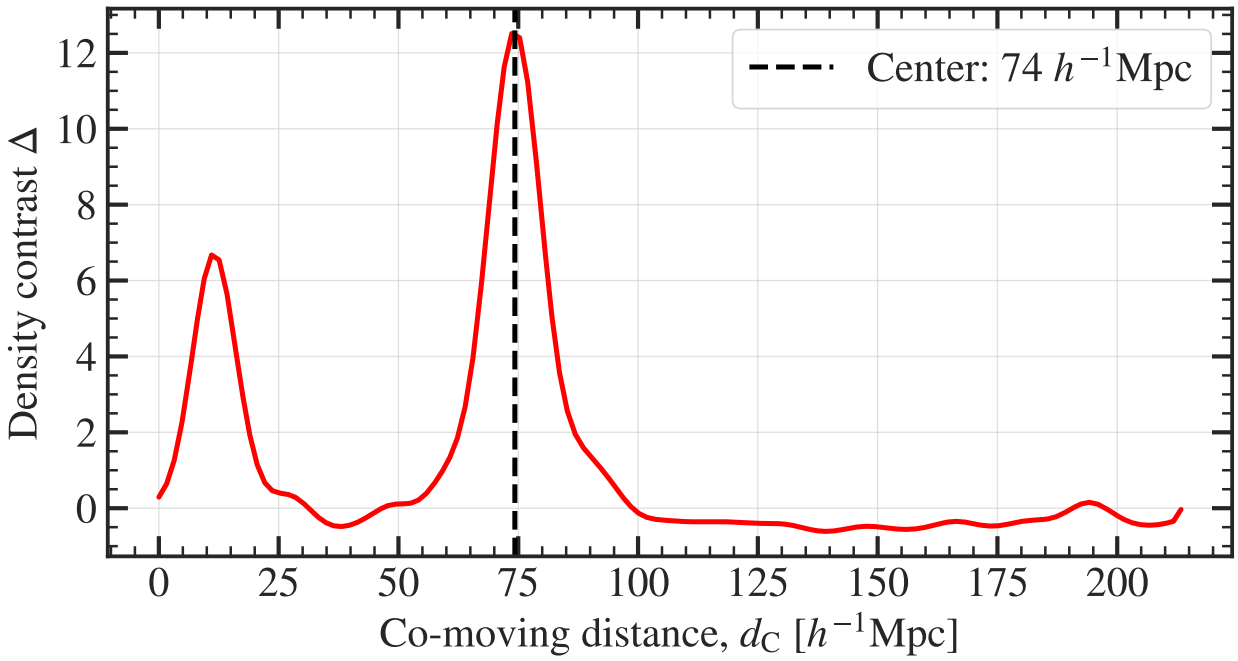

Figure 48: Density profile of the Coma cluster from the CARRICKS model.

As mentioned in Section 4.4.2, this profile is different compared to the equivalent profile obtained from the BORG model. Most noteworthy is the width of the density region surrounding the cluster, which is much wider in the CARRICKS model. In addition, we find a structure between 0 and 25 h^{-1}Mpc, which is not observed in the BORG model.

K Abbreviations

Table 21: Abbreviations used in this work

Abbreviation	Description
D-Sigma	The radio surface brightness to diameter relation
E1	Classical and almost round elliptical
E5-6	Elliptical galaxy with high eccentricity
GCLF	Globular Cluster Luminosity Function
PNLF	Planetary nebula luminosity function
TRGB	Tip of the Red Giant Branch
SAB(rs)0	Intermediate bar spiral with partial inner ring
SAB(rs)ab	Open bar spiral with partial inner ring with
SB(s)0	Intermediate bar spiral with winding open arms
SB(r)b	Bar spiral with closed inner ring
SBF	Surface Brightness Fluctuations
SNIa	Type Ia supernova
SNII optical	Type II supernova in the optical band